Title
Flexural Behavior of 3D Printed High-Strength Ductile Concrete Beams with Optimized Topology

Author
Malats Domenech, Amadeu

Publication Date
2021

Peer reviewed|Thesis/dissertation

UNIVERSITY OF CALIFORNIA,
IRVINE

Flexural Behavior of 3D Printed High-Strength Ductile Concrete Beams with Optimized Topology

THESIS

submitted in partial satisfaction of the requirements
for the degree of

MASTER OF SCIENCE

in Civil and Environmental Engineering

by

Amadeu Malats Domenech

Thesis Committee:
Associate Professor Mo Li, Chair
Associate Professor Anne Lemnitzer
Assistant Professor Joel Lanning

2021

TABLE OF CONTENTS

LIST OF FIGURES

LIST OF TABLES

LIST OF ABBREVIATIONS

3DCP	Three-dimensional concrete printing
HS-DC	High-Strength Ductile Concrete
FEM	Finite element model
MOR	Modulus of rupture
FDM	fused deposition modeling
PE	Polyethylene
CC	Contour Crafting
UHPC	Ultra-high performance concrete
VMA	Viscosity modifying admixtures

ACKNOWLEDGEMENTS

I would like to thank the guidance and the opportunity given to me by my Master Thesis advisor Professor Mo Li.

Also from the Balsells Foundation and specially Professor Roger Rangel for trusting me and awarding the Balsells Fellowship for conducting the MS Degree in Civil Engineering at the University of California, Irvine.

I appreciate the committee members Professor Anne Lemnitzer and Professor Joel Lanning for reviewing and evaluating this Thesis.

This thesis would not have been possible without the help of fellow laboratory researchers that taught me to use all the lab tools and equipment.

Finally, a big thanks for my family and friends that have always supported me whether in Spain, the USA or in any place I have been.

ABSTRACT OF THE THESIS

Flexural behavior of 3D Printed High-Strength Ductile Concrete beams with optimized topology

by

Amadeu Malats Domenech

Master of Science in Civil and Environmental Engineering

University of California, Irvine, 2021

Professor Mo Li, Chair

The technology of 3D concrete printing (3DCP) has the potential of revolutionizing the construction industry through an automated, rapid and economical method to build structures or infrastructure with minimal needs for formworks and labor. In order to realize the rational and wide adoption of 3DCP a series of fundamental challenges need to be addressed, ranging from new concrete materials science and engineering to enable the 3D printing process, to understanding the mechanical behavior of 3D printed concrete structural elements.

Conventional cast concrete is known to have a quasi-brittle nature and possess significantly lower strength under tension than under compression. Therefore, steel reinforcement is commonly used in flexural members made of concrete such as beams. While steel reinforcements can be well pre-aligned or installed in formworks before casting concrete, they are difficult to be integrated into the concrete 3D printing process when

formworks are absent. Therefore, this thesis proposes and investigates a new approach to 3D printing concrete beam members with novel concrete featuring a ductile (rather than quasi-brittle) behavior and an optimized topology. It is hypothesized that if a ductile strain-hardening tensile behavior of the 3D printed concrete can be achieved, it would lead to substantially improved flexural behavior of 3D printed beam members, in terms of flexural strength and ductility, thus reducing the need for steel reinforcement. It is further hypothesized that the 3D printed concrete beam with optimized topology and ductility would result in higher mechanical capacity but with less use of concrete materials.

To test these hypotheses, this thesis has two objectives: first, it aims to generate the understanding on the flexural behavior of beam members made of the high-strength ductile concrete; second, it aims to reveal how the optimized topology enabled by 3D printing will affect the flexural behavior of beam members made of high-strength ductile concrete. To achieve these, this thesis performs both experimental and numerical studies on the flexural behavior of small-scale beam specimens either casted or 3D printed with newly developed high-strength ductile concrete materials, either with or without optimized topology. It first performs topology optimization of a concrete beam geometry using finite element method (ABAQUS). Then, four types of concrete beam specimens are manufactured with novel high-strength ductile concrete: (a) 3D printed beams with optimized topology, (b) casted beams with optimized topology, (c) casted prismatic beams without topology optimization, which has the same total volume as the beams in (a) and (b), and (d) casted prismatic beams without topology optimization, which has the same effective volume between supports as the beams in (a) and (b). These beams are subjected to 4-point bending test. In addition, two types of boundary conditions are considered: (1) pin–roller support condition without horizontal constraint, and (2) with horizontal constraints at both supports. The force-displacement relation, strain field and damage pattern are experimentally measured.

In addition to the experimental study, finite element based modeling is performed using Abaqus to numerically analyze the behavior of the different beam specimens. The model considers the constitutive relation of 3D printed high-strength ductile concrete that is fundamentally different from that of conventional concrete, it also considers the given beam geometries and different boundary conditions same as the experimental setup.

This study elucidates how concrete material ductility, 3D printing method, topology optimization, and beam boundary conditions affect the flexural behavior of concrete beams. The novel ultra-high-strength ductile concrete transforms the concrete beam behavior from brittle and localized fracture to a displacement-hardening behavior with spatial microcracking damage and a highly ductile failure mode. In addition, the study shows ultra-high-strength ductile concrete can be successfully 3D printed, into the optimized topology of the beam element. The 3D printing process tends to align the fibers into the direction along the printing filament, leading to increased resistance to stress and strain long the beam direction under bending, but less resistance in the direction perpendicular to the printing filaments. Furthermore, the study shows topology optimization can improve beam flexural behavior, depending on the boundary conditions. Without additional horizontal constraint in the four-point bending test setup, the beams with optimized topology exhibit larger displacement capacity before failure and higher load-carrying capacity, than the prismatic beams without topology optimization. The failure mode is flexure governed. However, with additional horizontal constraint, the beams with optimized topology still exhibits larger displacement capacity before failure and higher load-carrying capacity than the prismatic beams without topology optimization; but the displacement capacity is significantly lower and the load-carrying capacity is significantly higher their topology-optimized counterparts without horizontal constraint at the supports. This is because the failure mode becomes more dominated by shear and compression in the topology-optimized beams.

Chapter 1. Introduction

1.1. Research motivation

The technology of 3D concrete printing (3DCP) has the potential of revolutionizing the construction industry through an automated, rapid and economical method to build structures or infrastructure. Different from the conventional construction method that concrete is cast into prefabricated formworks, 3DCP is a layer-by-layer deposition process, also known as additive manufacturing, through an automated robotic arm or a gantry printer. 3DCP opens opportunities of automated onsite construction with reduced need for labor and formwork, and of building complex structural geometries for higher mechanical performance that cannot be achieved through the conventional cast method. In order to realize rational and wide adoption of 3DCP, a series of fundamental challenges need to be addressed, ranging from new concrete materials science and engineering to enable the 3D printing process, to understanding the mechanical behavior of 3D printed concrete structural elements.

Normal cast concrete is known to have a quasi-brittle behavior and significantly lower strength under tension than under compression. Therefore, steel reinforcement is commonly used in flexural members made of concrete, such as beams, to resist tensile force and provide ductility. While steel reinforcements can be well pre-aligned or installed in formworks before casting concrete, they are highly difficult to be integrated into the concrete 3D printing process when formworks are absent. Therefore, this thesis proposes and investigates a new approach to 3D printing concrete beam members with novel concrete featuring a ductile (rather than quasi-brittle) behavior and an optimized topology. It is hypothesized that if a ductile tensile strain-hardening behavior of 3D printed concrete can be achieved, rather than the normal quasi-brittle behavior, it would lead to greatly improved flexural behavior of 3D printed concrete beam members in terms of flexural strength and ductility, thus reducing the need for steel reinforcement. It is further hypothesized that the 3D printed concrete beam with an optimized topology and ductility would possess higher mechanical capacity but with less usage of concrete materials.

The novel ductile concrete material investigated in this study features a tensile strain-hardening behavior as well as an ultra-high compressive strength. It is a fiber-reinforced cementitious composite material possessing a compressive strength of 100MPa and a large tensile strain capacity (also known as elongation capacity) up to 8%. This tensile strain capacity is extraordinarily high, 800 times that of normal concrete or 3D printed concrete (tensile strain capacity = 0.01%), thus providing remarkable fracture toughness and damage tolerance under both service loading and extreme loading conditions. The combination of ultra-high compressive strength and ultra-high tensile ductility, achieved through a sequentially formed spatial microcracking damage behavior (rather than a localized fracture behavior), provide great potential for 3D printing of concrete structural members with reduced steel reinforcement needs. Furthermore, optimizing the topology of structural members enabled by 3D printing can further reduce material usage but increase structural capacity and efficiency.

To test these hypotheses, this thesis has two objectives: first, it aims to generate understanding on the flexural behavior of beam members made of the high-strength ductile concrete; second, it aims to reveal how the optimized topology enabled by 3D printing will affect the flexural behavior of beam members made of high-strength ductile concrete. To achieve these objectives, this thesis study will be first perform topology optimization of a concrete beam geometry using finite element method (ABACUS). Then, four types of concrete beam specimens will be manufactured with the novel high-strength ductile concrete: (a) 3D printed beams with optimized topology, (b) casted beams with optimized topology, (c) casted prismatic beams without topology optimization, which has the same total volume as the beams in (a) and (b), and (d) casted prismatic beams without topology optimization, which has the same effective volume between supports as the beams in (a) and (b). These beams will be subjected to 4-point bending test under displacement control. In addition, two types of boundary conditions will be studied: (1) pin–roller support condition without additional horizontal constraint, and (2) with horizontal constraints at both supports. The force-displacement relation, strain field and damage pattern will be experimentally measured.

Furthermore, it is important to develop finite element-based numerical models to predict the mechanical behavior of 3DCP elements, for which the material constitutive relation is different from the conventional concrete and the structural member can have various geometries enabled by 3DCP. Therefore, in addition to the experimental study, finite element based modeling will be performed using Abaqus to numerically analyze the behavior of the beam specimens, and to compare the numerical predictions with the experimental data. The model will consider the constitutive relation of 3D printed high-strength ductile concrete that is fundamentally different from conventional concrete. It will also consider the given beam geometries and the boundary conditions same as the experimental setup.

The experimental and numerical results will be analyzed to elucidate how concrete material ductility, 3D printing method, topology optimization, and beam boundary conditions affect the flexural behavior of concrete beams. Finally, the thesis will discuss the major conclusions drawn from the experimental and numerical studies, and the future work to be performed to further advance this field.

1.2. Literature review

1.2.1. State of the Arts and Practice of Concrete 3D Printing

3D printing is a group of additive manufacturing (AM) technologies, that through a process of additive deposition of material by layers is able to create tridimensional solid objects from a digital model. [1]

The first AM method called stereolithography was invented in 1976 by Hideo Kodama using a liquid polymer that was hardened layer by layer using ultraviolet lights (Figure 1: 3D printing with the stereolithography process (Figure 1). [2]

In the following decades, other types of 3D printing methods were developed such as the fused deposition modeling (FDM). This method uses a thermoplastic material which is heated and extruded through a moving nozzle that deposits the material in the appropriate location layer by layer. Then the extruded thermoplastic filament gets cooled and hardened by the surrounding air and bonds to the adjacent layers producing a tridimensional object (Figure 2).[3]

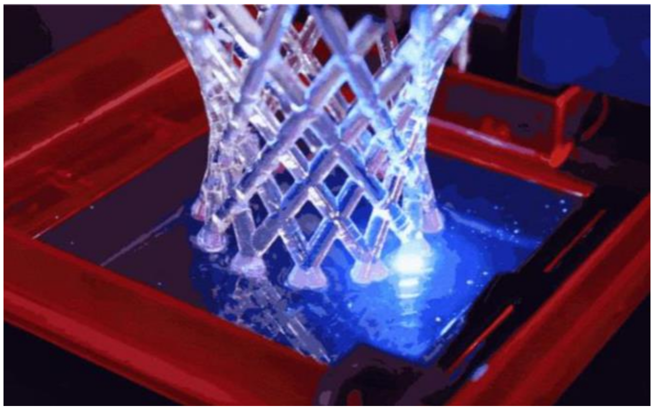

Figure 1: 3D printing with the stereolithography process [2]

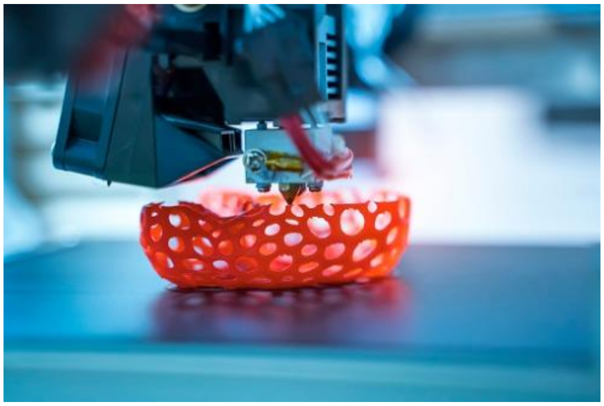

Figure 2: 3D printing using the Fused deposition modeling [3]

1.2.1.1. Extrusion Based Method

Contour crafting

Until the mid-1990s the 3D printing technologies were focused in producing small scale objects made by polymers or metals. However, Professor Khoshnevis changed this paradigm in 1998 introducing the technique of Contour Crafting (CC)[4]. This method also consists in extruding material through a moving nozzle like in the FDM method, but in this case instead of melted polymers the extruded material is a fresh cement-based paste. The use of concrete as the extruded material and using a large robot arm or gantry to move the nozzle enables this technology to 3D print large scale structures in a cost effective way. [5]

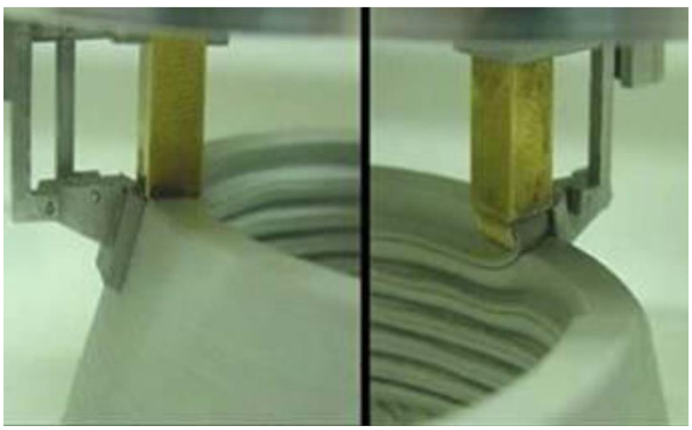

Figure 3: Contour Crafting extrusion nozzle while it is 3D printing a concrete wall [4]

Figure 4: Contour Crafting plan to 3DCP a house [5]

Since Contour Crafting was invented, other companies and research teams have developed their own technology of 3D concrete printing. While most of them work with the same fundamental technology of extruding a cement based paste, some differ in using a moving robot arm or gantry system and the mix design of the cementitious paste and its reinforcement.[6]

One of the major challenges the 3D concrete printing technology faces is the incorporation of reinforcement in the structure, as plain concrete has a low tensile strength and is brittle. [7]

Apis Cor

Some companies such as Apis Cor reinforces the 3D concrete printed structure introducing some steel bars between the printed walls which are then filled with casted concrete (Figure 5) [8]. This company holds the current record for the largest 3D concrete printed building in the world built in Dubai using this reinforcement method, and a moving printer crane that can rotate 360 degrees and extend itself in both horizontal and vertical directions (Figure 6). [9]

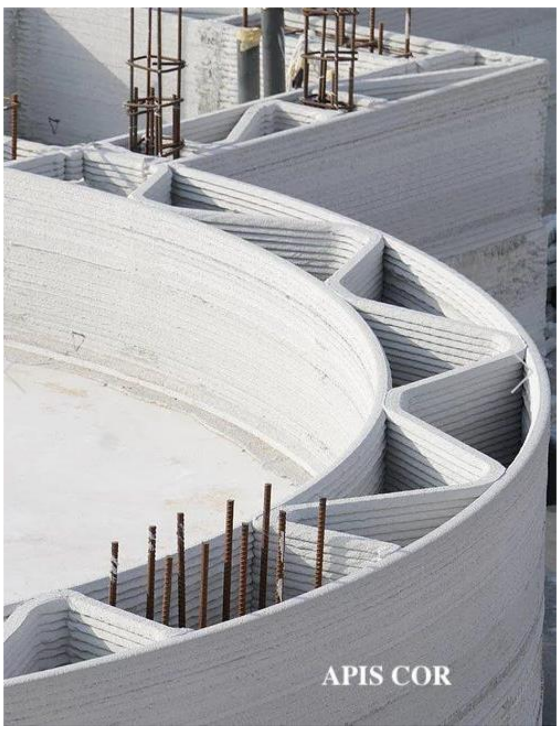

Figure 5: Steel bar reinforced 3D printed wall by Apis Cor [8]

Figure 6: Apis Cor 3D concrete printing crane [8]

Figure 7: World's biggest 3DCP building by Apis Cor [9]

Although the Apis Cor method of reinforcing the 3DCP building is structurally sound, the placement of the steel bars requires a lot of manual labor, which makes the process slower, more expensive, and dangerous for the health of the workers and limits the geometry of the structure. Apis Cor also has plans to 3D concrete print affordable housing in California which could greatly reduce its cost thanks to this revolutionizing technology.[10]

Winsun

The company Winsun in 2019 achieved to 3D print 10 houses (Figure 8) with 195 squared meters of area each in less than a day with a cost of 4800$ each. In this case, the company used a extrusion based 3D printer to manufacture parts of the house off-site and then transported and assembled the parts to the construction site, the 3D concrete printed parts where then put together and reinforced with conventional steel rebar. Using a similar method a 5-story apartment (Figure 9) was built with a total area of 1100 m^2, and also a concrete villa (Figure 10) with interior fittings for a cost of 160,000$.[11]

Figure 8: Winsun 3D printed 10 houses completed in 1 day [11]

Figure 9: 3D concrete printed 5-story building by Winsun [11]

Figure 10: Winsun 3D printed Villa for 160000$ [11]

XtreeE

The company XtreeE developed an AMOC method that consists in 3D concrete printing the formwork and then casting another material inside it such as ultra-high performance concrete to strengthen the structure or as insulation material like foamed concrete. The 3DCP formwork is left in the structure which is called lost-formwork. [12]

The balance between 3D printed material formwork and casted material is very important to achieve an economical viability, for some structures formwork 3D printing can be more optimal than all -3D printed or traditional construction.[13]

This company formwork 3D concrete printed a 4-meter tall pillar using UHPC with a topology optimized shape. The pillar was produced in 3 parts to reduce hydrostatic pressure when casting UHCP inside and for ease of transportation (Figure 11) and assembly in the final location (Figure 12). To improve the continuity of the joints between the three segments, metallic connectors where installed during the casting and chemical glue was used to seal the connection.[14]

Figure 11: XtreeE pillar being transported by parts [14]

Figure 12: XtreeE pillar assembled in its final setup [14]

Huashang Tengda

The Chinese company Huashang Tengda achieved to 3D concrete print a two-story villa manufactured on-site and in one-go, compared to the Winsun that has to transport and assemble the 3D printed segments of the structure. The structure of the Huashang Tengda houses (Figure 13) includes conventional steel reinforcement and plumbing pipes.[10] The construction process consists in first manually placing the steel rebar frame and the plumbing pipes, and then the concrete is 3D printed over it with a large scale printer that has a unique extruding nozzle of forked shape (Figure 14) that surrounds the steel rebar frame extruding concrete on both sides.[15]

Figure 13: 3DCP ville by HuaShang Tengda [10]

Figure 14: HuaShang Tengda 3D printing process with a forked nozzle [15]

The concrete mix used is an ordinary class C30 concrete, which is durable and tough, yet inexpensive. The wall thickness of the 3D printed villa is 250 cm and it has been tested that the structure could withstand a strong earthquake with a magnitude of 8 in the Richter scale.[16] The main disadvantage of this 3DCP method is that the process of installing the steel reinforcement frame requires a lot of labor and takes a long time, compared to only 3D printing.

University Federico II of Naples

Another technology to reinforce 3D printed concrete was developed by the University Federico II of Naples, Italy, that made use of modular 3D printed concrete segment with a topological optimized shape united using external steel bars, which combined together can create beams (Figure 15) or pillars.[17]

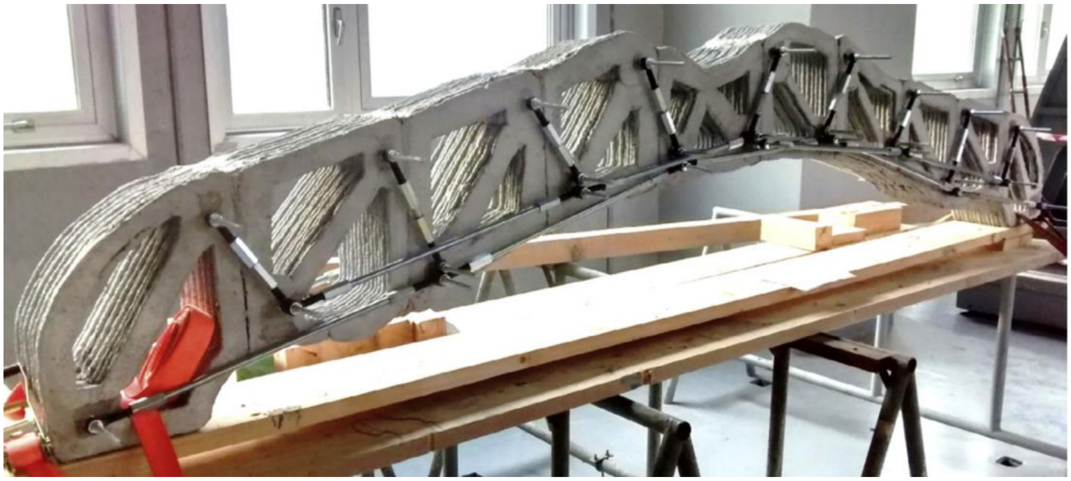

Figure 15: 3DCP modular beam reinforced with external steel rebar [17]

PERI

The PERI company built one of the most complex 3D concrete printed residential buildings in Germany. Using the 3D construction printer named 'BOD2' (Figure 16) supplied from COBOD which is reported to be the fastest on the market achieving a speed of 2.2 mph and completing a 1 square meter of wall in under five minutes. It uses a gantry system that moves along three axes on a metallic frame, only needing to be calibrated once. During the 3D printing process the machine analyzes the utilities such as pipes, cables , enabling the manual workers to install these utilities while the structure is being 3D printed (Figure 17).

The structure is composed of triple skin hollow walls, that are filled with insulating material requiring two operators to monitor the process. [18]

This 3D concrete printed house (Figure 18) have passed all the regulatory requirements in Germany so it can be inhabited.


Figure 16: PERI 3D concrete printer 'OBD2' from COBOD [18]

Figure 17: PERI 3D printing a house in Germany while workers install utilities [18]


Figure 18: First inhabitable 3D printed home in Germany by PERI [18]

PERI associated with Habitat for Humanity is also building some residential homes in Tempe, Arizona as a possible solution for a lack of affordable housing in the region. The single family homes will have a livable area of 1738 square feet and 80% of them will be 3D concrete printed while the rest of the construction is traditionally built.

Mighty Buildings

The company Mighty buildings is planning to create a zero net energy single-family homes community (Figure 19) in the area of Palm Springs, California. These homes will be fully sustainable using a light stone 3D printing material prefabricated in a factory setting, allowing for a good quality control, and then installed on-site. Solar panels would be installed on the roof to boost the sustainability of the complex and insulating the walls. [19]

Figure 19: 3D concrete printed home complex in Palm Springs [19]

WASP

The Italian company WASP built an environmentally friendly house (Figure 20) 3D printed using local soil in a zero-waste construction process, which did not require any material to be transported. It is obtained by excavating the soil, removing the stones and gravel with a sieve, and mixing the sieved soil with water and rice husks in a concrete mixer. Then the material is extruded using a layer deposition method (Figure 21).[20]

Figure 20: 3D printed dirt house by WASP [20]

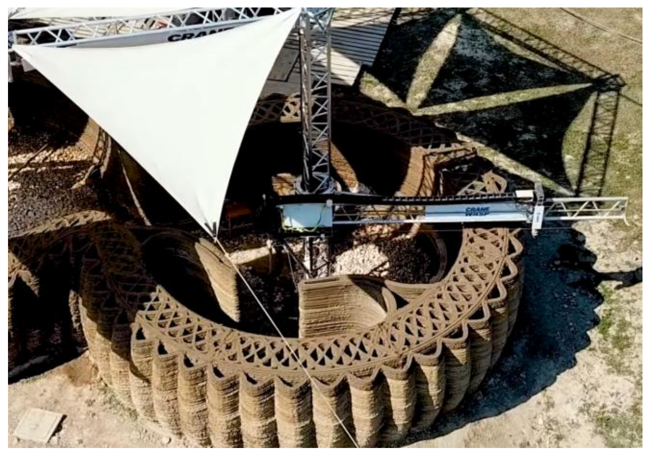

Figure 21: Process of 3D printing a house using dirt, water and rice husks by WASP [20]

ETH Zurich

A group of architects and engineers from Eidgenössische Technische Hochschule Zürich in collaboration with Zaha Hadid Architects and Incremental 3D have 3D printed a bridge made of unreinforced concrete (Figure 22). The 12m by 16m bridge is composed by several 3D printed blocks that are assembled in the arch shaped bridge (Figure 23). The 3D printed layers are made orthogonal to the flow of the compression forces so that each layer is well pressed against each other, and just by the compressive strength of the concrete material the structure does not need any other reinforcement.[21]

Figure 22: 3D concrete printed modular bridge being assembled [21]

Figure 23: Completed modular 3D printed bridge by ETH Zurich [21]

Ghent University

Researchers at Ghent University in collaboration with the company Vertico and the Technion Israel Institute of Technology have developed a 3D printed bridge (Figure 24) using the least amount of concrete.[22] Its shape is topologically optimized, for a post tension cable that runs at the bottom of the bridge that minimizes stress peaks. Reducing the amount of concrete have both an economic and time benefits and the capability of 3D printing in any topology optimized shape enables to produce cost effective and safe structures.[23]

Figure 24: Topology optimized post tensioned 3D printed bridge at Ghent University [22]

Institute for Advanced Architecture of Catalonia

The Institute for Advanced Architecture of Catalonia has developed a new approach to 3D printing large structures with concrete. Instead of using large robotic arms or gantry systems, the IAAC have developed a team of minibuilders (Figure 25) which consists of three types of small robots that can climb the structure and continuously 3D print over it. [24]

The foundation robots make the footprints of the initial 10 layers of the structure. The robots have a pipe connected to a concrete supplier that provides the printing material.

The Grip robots (Figure 26) have four rollers that clamps to the edge of the structure allowing it to move along the edge and printing additional layers of material, with a nozzle that can shift from side to side increasing the printing accuracy. These robots can even print horizontal ceilings and windows openings.

Vacuum robots (Figure 27) attaches to the surface of the previously 3D printed surface using a vacuum generator, and then can reinforce the structure 3D printing additional material around the object in any direction as it can move freely around the surface.[25]

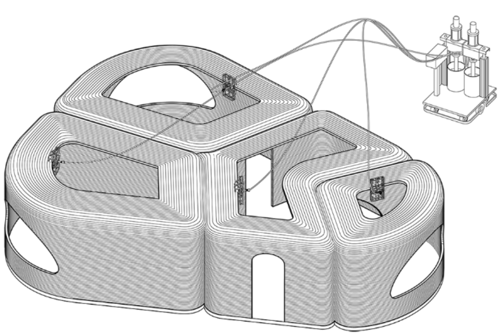

Figure 25: Representation of how the minirobots work at the same time 3D concrete printing a large structure by IAAC [24]

Figure 26: Grip robot 3D concrete printing a structure by IACC [24]

Figure 27: Vacuum minirobot reinforcing a 3D concrete printed structure by IAAC [25]

Tsinghua University

The Tsinghua University 3D concrete printed a 26.3 meter long by 3.6 meter wide bridge (Figure 28) in Shanghai, completed in 19 days.

The bridge has a modular composition (Figure 29) of 176 concrete segments 3D printed in 450 hours using a composite polyethylene fiber reinforced concrete and admixtures. The structure does not require any additional reinforcement or templates, and can then reduce the total cost by a third. [26]

The 3D printing robot has two arms with separate functions (Figure 30), one stirs and extrudes the concrete while the other controls the printing path and the operating system.

The bridge also integrates strain and stress sensors to obtain data in real time of the performance of the bridge. [27]

Figure 28: 3DCP bridge in Shanghai by Tsinghua University [26]

Figure 30: 3D concrete printing a modular bridge by Tsinghua University [26]

Figure 29: Modular installation of a 3DCP bridge by Tsinghua University [26]

1.2.1.2. Powder-based Technique

Powder-based deposition or binder-jetting is another large-scale additive manufacturing method that can create very accurate and complex shapes. This technique works by laying a granular layer, usually sand, and depositing a binder selectively where the object is to be constructed. This binder creates a bond between the particles that is in contact with. Then another powder granular layer is placed over with another round of binder layer by layer until the final object is completed. The remaining powder can be easily removed.[28] This technique enables the production of objects with a very complex shapes with inclined walls and ceilings, because the unbounded powder acts as a bed that holds the upper layers.

D-Shape

D-Shape is a company specialized in the binder-jetting technology (Figure 31) which uses sand as a powder and a magnesium-based binder with inorganic seawater that creates stone-like objects. The magnesium oxide reacts with the sand creating a strong chemical bond with a final product that is like a mineral with a crystalline structure and a high tensile strength, so D-shape structures do not require reinforcement.[29]

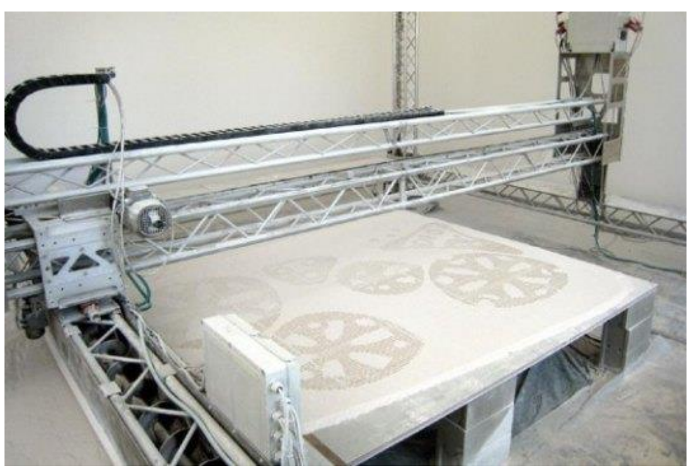

Figure 31: D-shape binder-jetting 3D printing process [29]

D-Shape in collaboration with the IAAC and the construction company Acciona made the first pedestrian 3D printed bridge (Figure 32) in the world located in Madrid. It has a span of 12 meters and a width of 1.75 m and was 3D printed using the D-shape technology of binder-jetting. The shape of the bridge was topology optimized to minimize the amount of material and waste by recycling the raw material during the printing.[30]

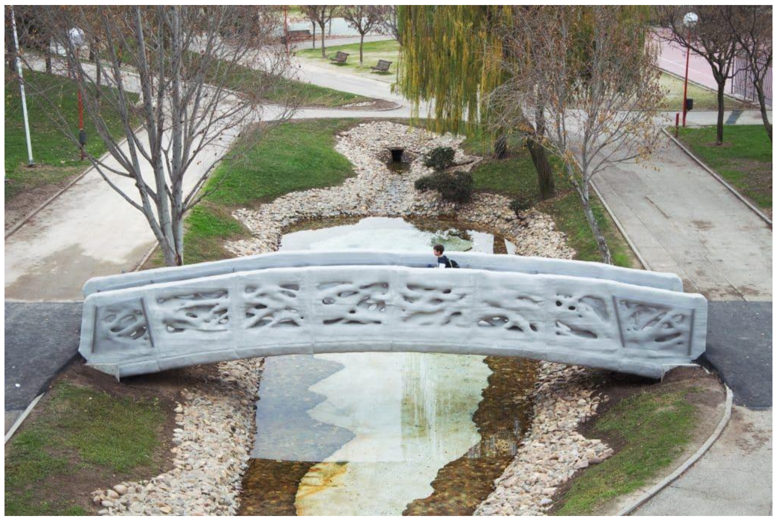

Figure 32: 3D printed pedestrian bridge using binder-jetting technique by D-shape [30]

1.2.2 Advantages of 3DCP

Compared to conventional construction methods, the major advantages of 3D concrete printing are the capacity to autonomously produce complex designs of structures that are cost effective because its shape can be optimized to require less material, produce less waste and being built much faster as it can print at a rapid pace 24 hours a day. As a result 3DCP requires less manual labor and in some cases it might not require any at all so it is a much safer method of construction, which would prevent many accidents and casualties that are currently happening in the construction industry. Because of conventional construction methods, construction is one of the most dangerous industries, with 150,000 injuries and 1000 deaths annually in the US [31], the majority of whom are aged between 25 and 34 years old. Also has one of the highest suicide rates for its workers which reflects the demanding and dangerous aspect of the manual work.[32]

In terms of economic and environmental impact, construction represents 9% of the global GDP and it usually operates with low benefit margins of around 5% so the increase in efficiency from 3DCP can make for a big difference. Due to its significant size, the construction industry is responsible of 8% the man-made CO2 gas emissions that pollutes the environment and contributes to climate change, and that could be reduced using greener concrete mix designs and taking advantage of the reduced material consumption and waste generated that 3DCP technology offers.[33]

The productivity of the construction industry has remained stagnant for decades with minimal improvements in its practice which is still very labor intensive, the 3DCP technology presents itself as a great opportunity to revolutionize this field if it can overcome some major challenges such as the reinforcement of concrete in order to resist the tensile stresses and provide a good interlayer bond. Some research groups are working in alternatives such as reinforcing the material using small fibers mixed in the concrete paste to increase its performance, although currently no real project has used this kind of material. The possibility of using ultra high performance fiber reinforced concrete might be the best option to launch this technology[34]. For this reason this thesis studies the 3D printing of High Strength Ductile Concrete structures, which makes use of short PE fibers that provides a strain-hardening behavior and ductility to the material. Due to these properties no additional reinforcement could be required.[35]

CHAPTER 2: Experimental Program

2.1. Introduction

The experimental program chapter covers the process of the design, fabrication and testing of the specimens. The objective is to obtain the force-displacement relationship and strain field for the 4-point flexural bending test results for every type of beam. The geometry design of the beam was carried out using a topology optimization tool provided by the Abaqus software that maximizes the stiffness for a given amount of material and boundary conditions. The next part is the production of the 3D printed beams that have the topology optimized shape and the conventional prismatic shaped beams. And the last part of the chapter explains how the 4-point bending test was carried out.

2.2. Topology optimization

The Additive manufacturing technology enables the manufacturing of complex structures in an easy, efficient and cost effective way .The 3D concrete printing can produce an object in any shape if the vertical stability of it is maintained, which means that the inclination and overhang of the printed element is the only design limitation.[36] This topological optimization have an important impact on the manufacturing efficiency, decreasing the material, waste, time, energy and environmental impact and as a result its cost. So not taking advantage of this quality of 3D printing into a more optimized shape would be unjustified.[37]

However, the process of topological optimization is not trivial, depending on the objective different criteria can be applied, for instance different parameters or a combination of them can be optimized such as strength, stiffness and volume.

The topology optimization also depends on the material properties, loading states and boundary conditions. Mathematically the topology optimization consists of finding the minimum or maximum of an objective function that depends on all the parameters like material properties, loads and boundary conditions.

The 3D printing technology has a limited resolution and precision that depends on the nozzle size and the extrusion width. Because of this, the result from the theoretical topology optimization given by the software Abaqus, which is very fine detailed, has to be adapted and simplified in order to be 3D printable.[38]

The first step to calculate a topology optimized shaped in Abaqus is to define a volume of material that will contain the optimized design. In this thesis a prismatic beam of dimension 12”x4”x1” clamped on the sides with a vertical distributed load (Figure 33) is topologically optimized using the tools for this purpose that are provided within the FEM software Abaqus.

The output parameter to minimize for the initial iteration of the design response is the strain energy. As a consequence, the topologically optimized beam will have the lowest strain for a given amount of material, or in other words the beam will be have the highest stiffness for a given material amount contained inside the initial reference volume. The resulting optimized beam from the previous routine is shown in the following (Figure 33):

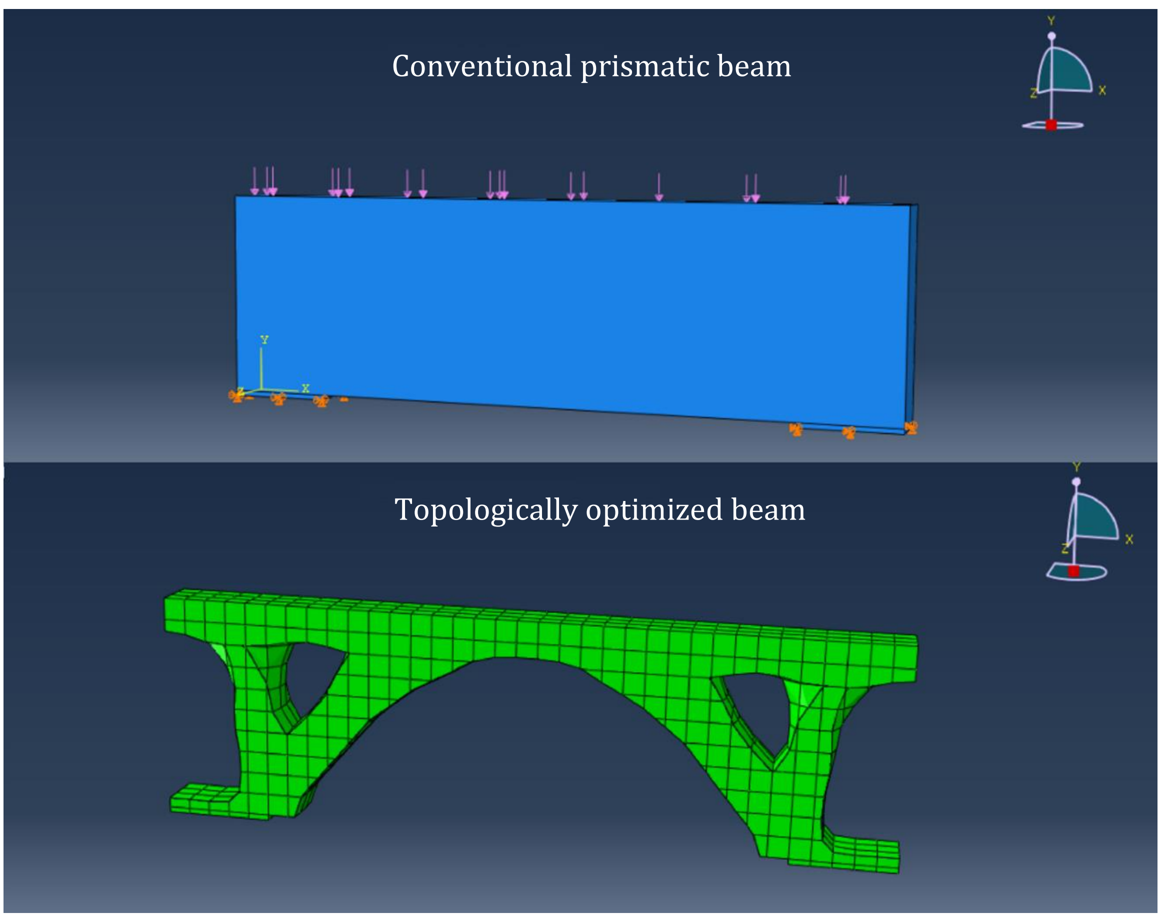

Figure 33: Beam topology optimization using finite element method

From the Abaqus software optimized beam it can be seen that it takes the shape of an inverted catenary arch, which makes sense as the catenary is the shape that distributes the loads uniformly along its path, and the tensile stresses are reduced in the middle of the arch as it have more compressive stresses due to the clamped boundary conditions of the beam. Moreover, it appears that two holes are created within the structure to save volume in an area that is not subjected to as much stresses as the interior of the beam.

The topology optimized beam from Abaqus has to be adapted to the 3D printing process limitations, specially for a small scale beam in which the printer does not have much resolution and the width of the printer nozzle is as wide as one layer of the topology optimized sections of the beam. The postprocessed topology optimized beam adapted to the small scale 3D printing process is shown in the following (Figure 34) and also showing all the layers and printing paths in the software Simplify3D that translates the CAD file (**Error! Reference source not found.**) to a .stl file that the 3D printer can read.

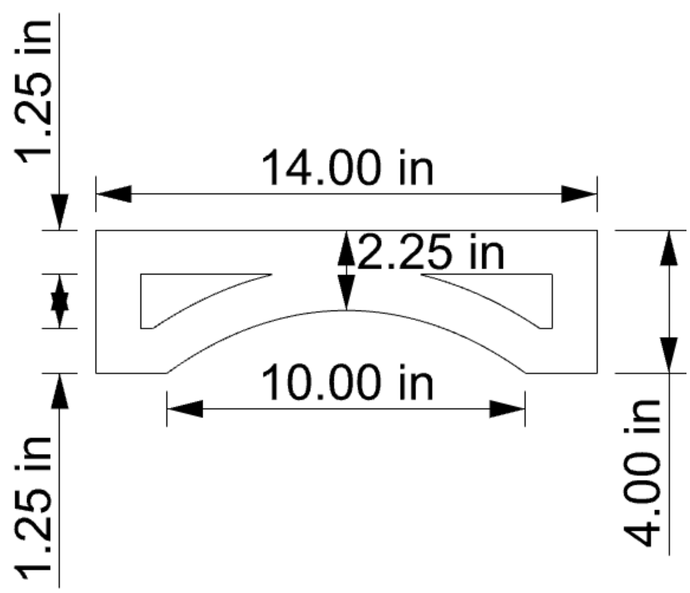

Figure 34: Dimensions of beam specimen with postprocessed topology optimization

Figure 35: CAD model of the specimen with postprocessed topology

2.3. High Strength Ductile Concrete for 3DCP

The development of ultra-high-strength ductile concrete for 3D printing was achieved based on a systematic approach that synergically (a) designs the properties of the raw solid ingredients, water and chemical admixtures to achieve an optimized particle size distribution and packing density, hydration and pozzolanic reaction kinetics and the resulting microstructure for reaching an ultra-high compressive strength; (b) tailors rheological parameters such as the yield stress, plastic viscosity and thixotropy to enable the 3D printing process including the extrusion and precise deposition capacities as well as the shape deformation resistance and early-age strength gain; and (c) design the micromechanical parameters including the cementitious matrix toughness and the interfacial constitutive behavior between the cementitious matrix and the polymeric fibers to achieve a high tensile ductility, particularly at the given matrix ultra-high strength and the rheological parameters for 3D printing.

Achieving a tensile strain-hardening behavior in fiber reinforced cementitious composite materials is based on fundamental theory of micromechanics and fracture mechanics.[39][40]. Steady-state cracking must be prevalent in the cementitious composite material, instead of typical Griffith-type cracking. Steady state crack propagation can be achieved through tailoring the matrix toughness properties and fiber/matrix interfacial bonding constitutive relation to satisfy Equation 1.[34][41]

$$J_{tip} \leq \sigma_o \delta_o - \int_0^{\delta_o} \sigma\,(\delta) d\delta \;\equiv\; {J_b}' \qquad (1)$$

Where $\sigma(\delta)$ describes the averaged (or smeared) fiber bridging stress across a crack vs. crack opening relation, J_{tip} is the matrix toughness at the crack tip, determined by:

$$J_{tip} = \frac{K_m^2}{E_m} \tag{2}$$

Where K_m is the matrix fracture toughness and E_m the matrix elastic modulus. σ_o is the maximum fiber bridging stress across a crack, and δ_o is the critical crack opening corresponding to the maximum fiber bridging stress. σ_o.[42]

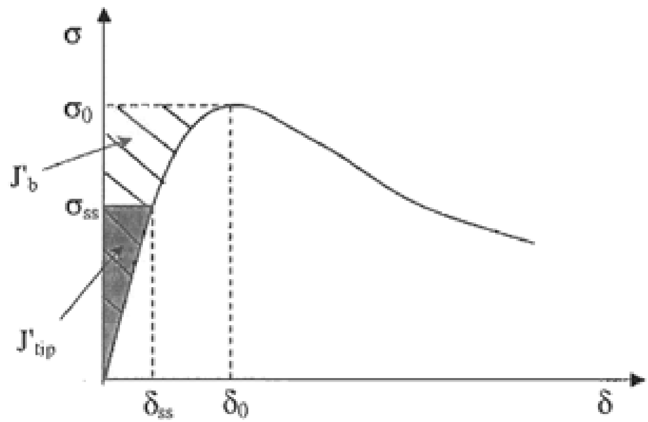

Figure 36: Constitutive relation between smeared fiber bridging stress across a crack and the opening of the crack. The darker shaded area represents the matrix toughness at the crack tip, which should be less than the complementary energy represented by the lighter shaded areas [34]

Furthermore, the initial matrix cracking stress σ_{fc} must be smaller than the maximum fiber bridging stress σ_o. .[41] The matrix should also contain sufficient natural flaws such as air pores and weak aggregate/binder interfaces, which behave as crack initiators by having the flaw size larger than the critical flaw size governed by the fiber bridging stress vs. crack opening relation.

Achieving the correct rheology for 3D printing considered the following requirements[43] [44]:

- Pumpability: it is the ability of the fresh material to being moved through the pump, tubes and extruding system.
- Printability: the reliability of the depositing material at maintaining its properties and filament continuity while being extruded (Figure 37).
- Buildability: the capacity of the deposited material to resist deformation and maintain its shape in a fresh condition (Figure 38).
- Open time: The period during which the material pumpability, printability and buildability and other properties are within an acceptable performance for the printing process to continue and complete[45].

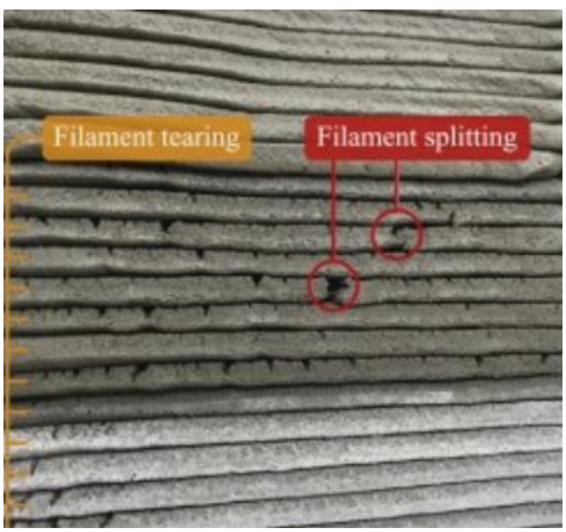

Figure 37: Example of poor printability [42]

Figure 38: Example of poor buildability in 3D printed concrete [42]

2.4. Specimen types and fabrication

In order to study the performance of 3D printed High Strength Ductile Concrete structures and its feasibility as a construction method, that could solve the challenges of reinforcing 3DCP structures to resist shear and tensile stresses, several beam specimens were produced at a small scale, to be loaded under a 4-point flexural bending test to obtain the force-displacement relationship and the strain field using DIC. These results will show the beam behavior in resisting shear, tensile and compressive stresses. Moreover, in order to understand the role of every aspect in the beam such as the 3D printing path, fiber alignment and geometry, different types of specimens are produced, all of them using the same High Strength Ductile Concrete mix.

The first kind and most representative specimens of this technology are the 3D printed beams with the topology optimized geometry, having a total length of 14 in, width of 4 in and 1 in thickness (Figure 39).

Another type of specimen has the same topology optimized geometry of the previous beam but is produced by casting the HS-DC material (Figure 40) into a mold instead of being 3D printed. This type of specimen will show the effect that causes the 3D printing process which tends to align the fibers in the extruded material direction along the printing path, which in turn increases the performance of the material in that same direction but is decreased in the perpendicular.

The next specimen type is another casted beam but with a conventional prismatic shape having the same total weight and volume (Figure 41) as the topology optimized beam type, with the dimension of 14 in length, 2.79 in width and 1 inch thickness. The change in performance in this prismatic shaped beam will show the impact of the topology optimization geometry.

The last specimen type is another prismatic beam (Figure 42) but that has the same volume as the topology optimized beam only in the region that spans 12 inches between the 4-point flexural bending test lower roller supports shown in red in (Figure 43), as it is the region of the beam that supports the majority of the stresses while the material situated outside the rollers does not interact much. Being the effective volume the same in the topology optimized beam makes a more fair and rigorous comparison between the two beam geometries.

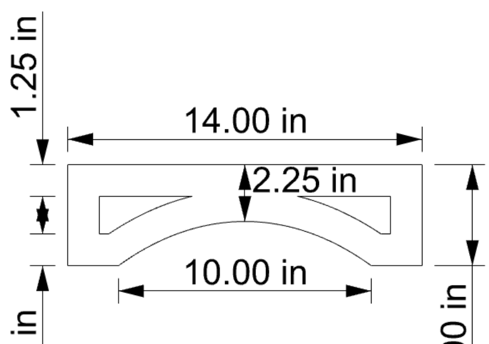

Figure 39: 3D printed beam with optimized topology

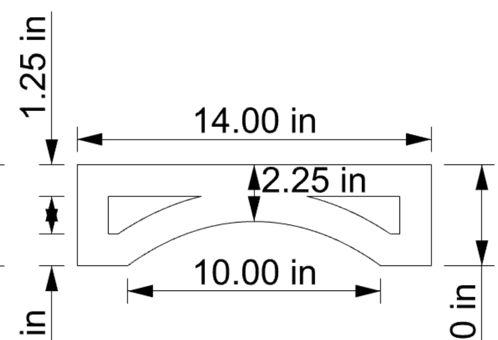

Figure 40: Casted beam with optimized topology

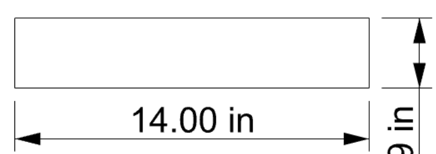

Figure 41: Casted prismatic beam with the same total volume as the topology-optimized beams

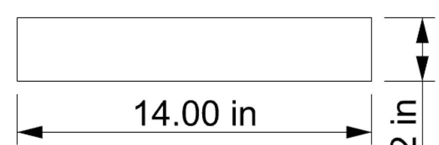

Figure 42: Casted prismatic beam with the same effective volume between supports as the topology-optimized beams

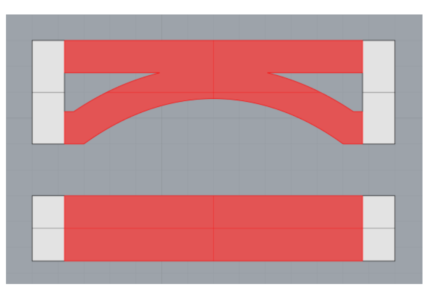

Figure 43: Effective volume highlighted in red for the prismatic and topology optimized beams

A total of 32 beams are produced, distributed in 8 specimens for each type of beam in order to have a fair amount of data for each beam type to avoid statistical variability and have a more coherent analysis of the results.

The manufacturing process of the beam specimens starts mixing and producing the High Strength Ductile Concrete material with the suitable rheological properties for being 3D printed. The casted beam HS-DC does not require any special rheological characteristics, but same mix design is used for all the casted and 3D printed specimens.

For producing the casted topology beam specimens several layers of cardboard were cut with the topology optimized shape and stuck together with glue to get a 1-inch thick cardboard formwork. Then the inside borders of the cardboard were covered by tape to smoothen and impermeabilize the surface of the cardboard that will be used as a mold for casting the beam. The inside mold wedge shaped pieces were situated using tape in order to fix them to the rest of the formwork and make sure its position is maintained when the HS-DC is casted.

Figure 44: Cardboard mold for the topology optimized beam with length measurement

Figure 45: Cardboard mold for the topology optimized beam with side measurement

With the fresh HS- DC in the optimum rheological condition and checking that the PE fibers are well dispersed in the mix, the material was casted into the cardboard formwork as a continuous filament in order to avoid patches of material whose PE fiber would not be well connected and impacting the behavior of the material as the fibers would not cross one side of the patch of material to the another creating a weak contact area. The material was then compacted to fill all the volume and corners of the mold. Finally, the surface of the casted specimen was smoothened (Figure 46).

Figure 46: Casted beam with optimized topology

In the first attempt of producing the 3D printed topology optimized beams using the 3D printer and laying the material on an open surface was proven to be difficult to achieve the precision and geometric tolerances required of the designed topologic optimized shape. So it was decided to 3D print inside the same cardboard formwork (Figure 47) used for the casted topology optimized beam. But in this case 3D printing inside the mold to achieve the precise geometry and guarantee that all specimens have the same shape, volume and weight. The 3D printing was performed in a continuous path around the mold with a total of 4 layers stuck together. After the 3D printing process was completed, the top surface was also smoothened (Figure 48) to get a perfectly flat surface with a constant thickness of 1 inch like in the casted specimens.

Figure 47: 3D printing of topology-optimized beam with a SCARA robot

Figure 48: 3D printed beam with optimized topology made of high-strength ductile concrete

The prismatic shaped beams were casted in a casting mold board using a 1 inch thickness rails and allowing them on one side to move to be adjusted to the precise location to get a 2.79 inches width for the Same total volume prismatic beam, and 2.52 inches width for the Effective volume prismatic beam. The material was also casted avoiding cold joins and maintaining the continuity of the material fibers.

Finally, the material was evenly distributed to fill all the mold and the surface was smoothened to get exactly 1-inch thickness like in the other specimens (Figure 49).

Figure 49: Casted prismatic beams made of high-strength ductile concrete

All the specimens were then covered with transparent plastic sheets for curing during the first four days, to minimize evaporation and retaining the water inside the fresh HS-DC to get the highest possible strength.

Figure 50: Fresh specimens covered with plastic sheets for curing for the initial four days

After four days, the HS- DC had hardened enough to be removed carefully from the mold and be stored in a curing room at a 100% humidity for the following 24 days.

In the 28th curing day the specimens were taken out from the curing station and using a saw and sandpaper the excess material was removed and the surfaces were further smoothened.

Followed by a cleaning to remove dust the specimens were prepared for being painted with a high contrast pattern for the Digital Image Correlation (DIC) system be able to capture the strain and displacement field during the tests. First a coat of plain white was applied (Figure 51) to the front area and then with a matte black spray a dotted pattern was applied (**Error! Reference source not found.**).

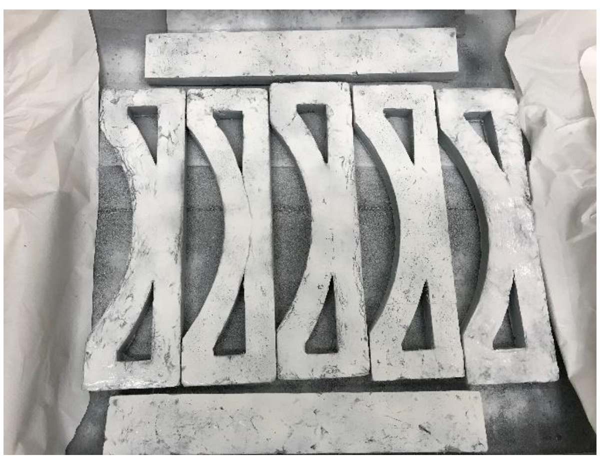

Figure 51: Specimens sprayed with a base white paint for subsequent DIC measurement of strain field

Figure 52: Specimen spray-painted with a black dotted pattern for subsequent DIC measurement of strain field

2.5. 4-Point bending test with digital image correlation system

The beam specimens are to be loaded under a 4-point flexural bending test, which consists in placing the beam supported over two rollers separated by 12 inch, and subjected to a load from the upper two rollers that are separated 4 inches centered in the middle of the beam (Figure 53). A command of displacement controlled at a constant speed is given and the MTS machine records the reacting force for every displacement value.

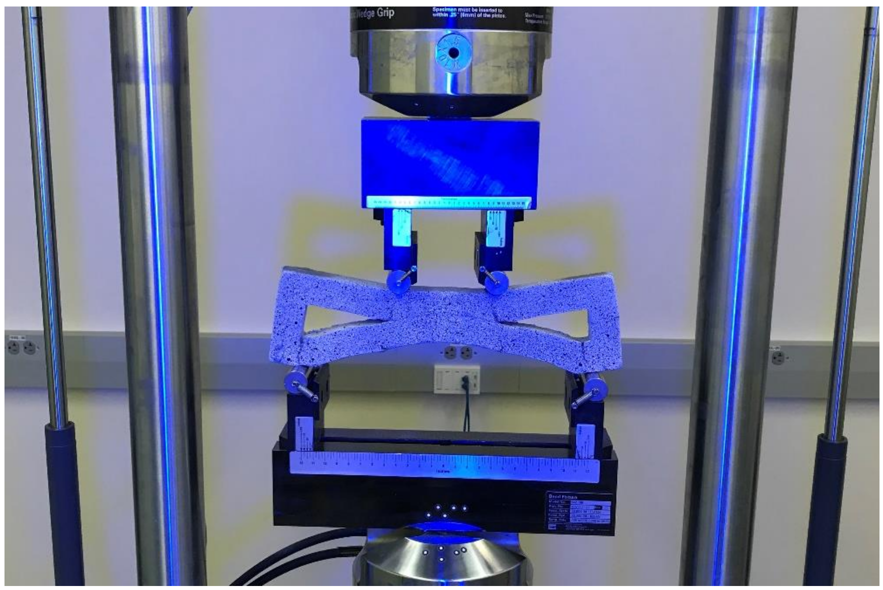

Figure 53: 4-point bending test setup

The test produces a flexural bending load that translates into the beam specimen as compressive stresses on the top of the beam, tensile stresses on the lower side and shear stresses on the outsides. This test is chosen because it produces more types of stresses compared to other tests such as the uniaxial tension or compression test which only produces one kind of stresses.

The topology optimized beam is designed considering the optimized geometry from the Abaqus software were the initial reference volume boundary condition is clamped on the lower sides, so the optimized shape beam would perform the best if its lower sides were to be clamped instead of allowing free movement like in a conventional 4-point bending test. For this reason a solid steel clamp was designed and manufactured using steel such that it restrains the lateral expansion of the sides of the beam (Figure 54) which better approximates the FEM topology optimization boundary condition that clamped the lower sides of the beam.

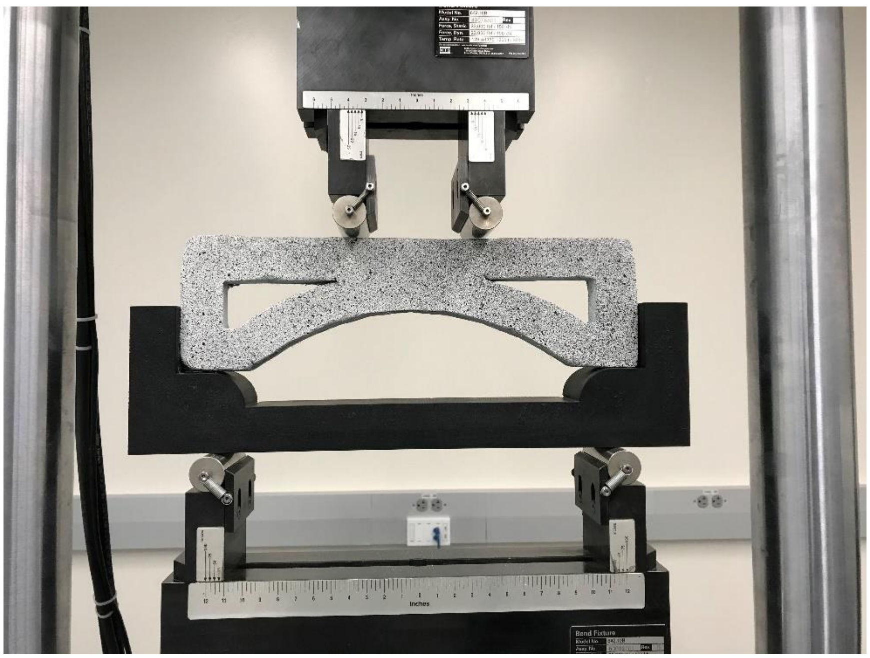

Figure 54: 4-point bending test setup with the modified fixture to provide additional horizontal constraints at both supports

This boundary condition would increase the performance of the topology optimized beam as the lateral confinement increases the compressive side of the stresses on the beam , reduces the tensile region, and the geometry of the catenary arch is able to resist better in compression than in tension. Because High strength Ductile Concrete and concrete in general have a much greater compressive strength, of around ten times the tensile, the global performance of the beam under these boundary conditions would be greatly improved compared to the normal 4-point bending test ,which will also be tested in this thesis, but in this case it is expected to show a lower performance for the 3D printed topology optimized beam.

There are a total number of 32 specimens distributed in 16 beams for the conventional 4-point flexural bending test with 4 beams for each type and the remaining 16 beams will be tested using the steel clamp fixture that restrain the lateral movement with 4 specimens tested for every kind of beam: 3D printed topology beam, casted topology beam, same total volume prismatic beam and effective volume prismatic beam.

The 4-point flexural bending test will be recorded by a Digital Image Correlation camera (Figure 55) that saves the whole test history with images and produces a strain and displacement field on the front surface of the specimen, giving a very valuable information of the areas that takes the most strain and damage.

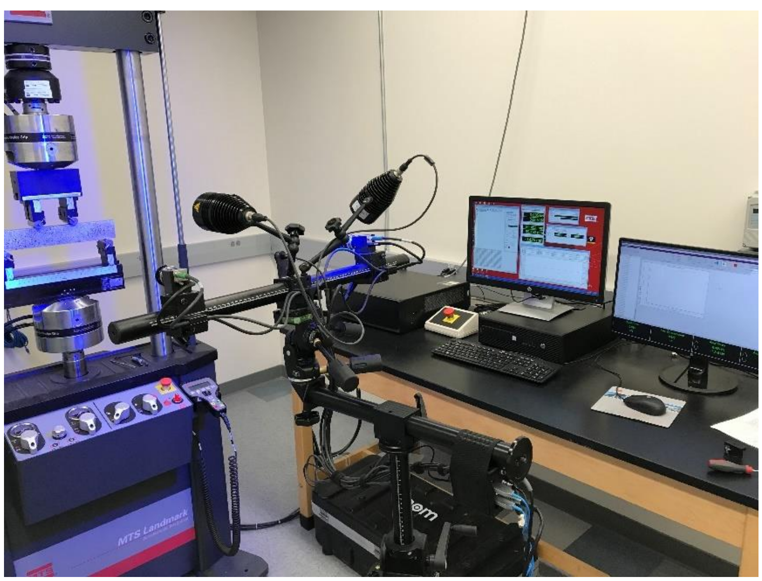

Figure 55: Digital Image Correlation system (DIC)

CHAPTER 3: Experimental Results and Discussion

3.1. Introduction

In this chapter, the results from the experimental program are presented and analyzed. These are obtained from the MTS universal testing machine that carries out the standard 4-point flexural bending test and delivers the force-displacement curve. From these data, the flexural stress-Displacement curve which are stresses in the middle section of the beam. The major strain field distribution over the beam front surface is also analyzed using the Digital Image Correlation camera. The camera provides a magnitude at every point and time of the front surface of the specimens. This magnitude can also be related to the vertical displacement. Moreover, the microcracking pattern of the HS-DC is also examined to obtain evidence relating this multicracking pattern with the overall behavior of the beam represented with the flexural stress -displacement curves and major strain field.

The first group of test results presented are from the standard 4-point flexural bending test which comprises the following: 4 beam specimens with a 3D printed topology optimization, 4 casted topology optimized beams, 4 prismatic beams with the same total volume and 4 prismatic effective volume beams. Altogether, there are 16 beams.

The same types and number of beams are also tested with the modified 4-point flexural bending test, using the customized steel clamp that restrain the lateral displacement of the beams. The results from each kind of beam are compared together in order to understand the difference in behavior arising from the 3D printing process and the topology optimization.

Some extra beam specimens are produced without the fibers that are contained inside the High-Strength Ductile Concrete while maintaining the same types of geometry as the Topology optimized and prismatic beams. This means only maintaining the cementitious matrix of the HS-DC material, and as a consequence, these specimens will not present a strain-hardening behavior, but it will show how brittle plain concrete is compared to the same material with the PE fibers, which is the material that has the fill potential of being 3D printable and structurally sound.

3.2. Flexural Behavior of 3D printed high-strength ductile concrete with optimized topology

Four 3D printed topology optimized beam specimens, numbered in order from 3D-1 to 3D-4, were tested in the standard 4-point bending test at a constant displacement rate of 0.05 mm/s. Figure 56 shows the relation between the flexural stress in megapascals versus the vertical displacement at the top rollers of the MTS bending test machine.

The Table 1 shows for every specimen the peak strength in megapascals which is the maximum value of flexural stress, and the displacement capacity at roller in millimeters which is the total vertical displacement of the beam before the flexural stress starts decreasing at a high rate. The displacement capacity at rollers is also related to the moment at which the critical crack in the HS-DC starts to propagate beyond the steady state. The moment widens the crack opening and causes the beam to collapse, losing the strength and the ability of the HS-DC to recover its original shape.

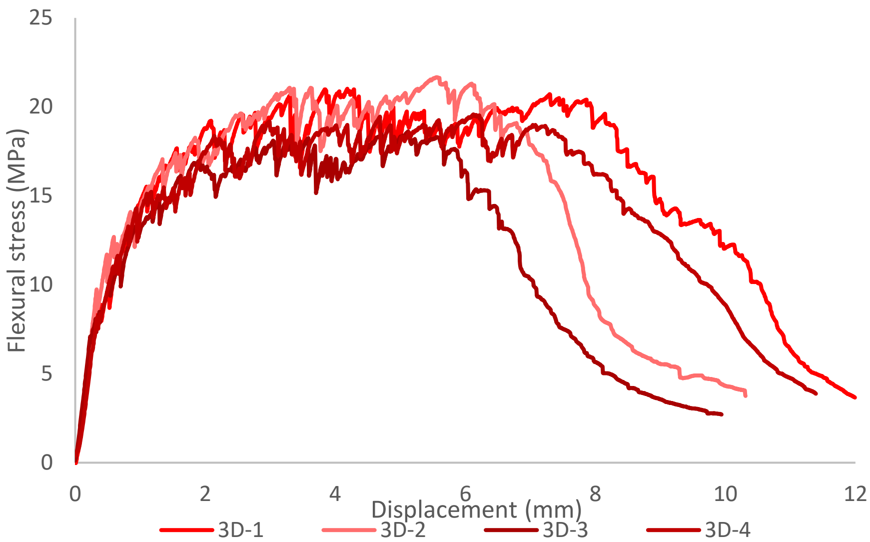

Figure 56: Flexural stress-displacement (at roller) curves of 3D printed topology-optimized beams under four-point bending

Table 1: Flexural strength and displacement capacity values for the 3D printed topology optimized beams

Repeat Specimen #	*Flexural Strength (MPa)*	*Displacement Capacity (mm)*
3D-1	20.8	8.3
3D-2	21.7	7.2
3D-3	18.3	6.5
3D-4	19.5	8
Average	20.1	7.5

From the flexural stress -displacement relation of the 3D printed topology beams, it can be seen an elasto-plastic behavior. There is an initial stage for a small displacement in which the material behaves as an elastic body with a linear relation between flexural stress and displacement with an average slope of 23.21 MPa/mm, until reaching a displacement of 0.28 mm from which there is a change in behavior at a flexural stress of 6.5 MPa which represents yielding point. After this point, the behavior becomes plastic with variable strain-hardening slope, meaning the material is still gaining strength as its being further displaced, but in this case with a lower slope than in the elastic stage and decreasing as its being strained.

In the strain-hardening stage from the Figure 56 it shows a sawtooth pattern curve in which there are several small drops that are rapidly recovered in excess until reaching the maximum flexural stress or flexural strength, with an average of 20.1 MPa for this kind of beam. After the peak strength is reached, the tendency of the curve is to decrease the flexural stress with larger displacements while still having the sawtooth shape but now the dips are larger than the recovery producing a downward trend of flexural stress. Physically each sudden dip of flexural stress in the HS-DC beam happens when a new microcrack is formed in the HS-DC matrix, but the flexural stress value before the dip is quickly recovered when the new propagated microcrack reaches the steady state. The accumulation of several of these steady state microcracks that creates small gaps bridged by fibers is what gives the High-strength Ductile Concrete its ability to deform and to behave as a ductile material although cementitious matrix is still a brittle material. In this case the 3D printed topology beam specimens can support large displacements and bend.

For this type of specimens the average maximum displacement supported before the beam flexural stress starts to decrease rapidly is 7.5 mm, the rapid decrease in flexural stress at the end of the test is due to the critical crack leaving the steady state regime and starting to further propagate causing a decrease in strength and the collapse of the beam at a larger displacements.

Figure 57: 3D printed topology-optimized beam (Specimen 3D-2) after testing

Figure 58: Close-up front view of final failure region in 3D printed topology-optimized beam (Specimen 3D-2)

Figure 57 shows the 3D printed topology beam 3D-2 specimen after the 4-point bending test, in which clearly shows the critical crack in the middle-right side that led to its collapse due to the bending of the beam, caused by the tensile stresses on the lower middle section. It can also be seen the overall curvature of the beam at the end of the test that supported 7.2 mm of displacement and a peak flexural strength of 21.7 MPa. The next Figure 58 shows a close-up image of the same critical crack with some fibers still bridging the gap, although many have been pulled out. The same picture also shows several steady state microcracks along the border perpendicular to the span of the beam and the curvature of the outer surface. Another view of the same cracks from the underside of the beam appears in the Figure 59 showing two major agglomerations of cracks, one around the critical crack and another agglomeration on the opposite side of the beam symmetrically with respect to the center. The concentration of microcracks in these areas indicates that in these regions produce the largest strains and stresses and as a result the most damage and microcracks are present there, which ultimately leads to the collapse of the beam.

Figure 59: Damage pattern in the bottom tensile region in 3D printed topology-optimized beam (Specimen 3D-2)

Figure 60: Microcracks formed around the corners (notches) due to stress concentration

Other areas of the beam also contain a microcracking pattern, such as around the triangular cavity on both sides of the beam shown in Figure 60 Due to these pointy vertices that produce stress concentration it leads to the propagation of microcracks in the region. Although in these areas the microcracks do not cause the collapse of the beam, they contribute to the overall displacement and bending capacity of the beam providing more ductility.

The following Figure 61 shows the major strain field obtained from the Digital Image Correlation sensor (DIC), in which the areas that present the multicracking patterns are related to the red shaded regions on the DIC major strain field that represent the largest tensile strain. In general, most of the deformation of the beam under the 4-point bending test is occurring along the lower side of the catenary arch, and some additional in the stress concentration areas at the vertices of the triangular cavities that constitutes the optimized topology geometry of the 3D printed beam specimen.

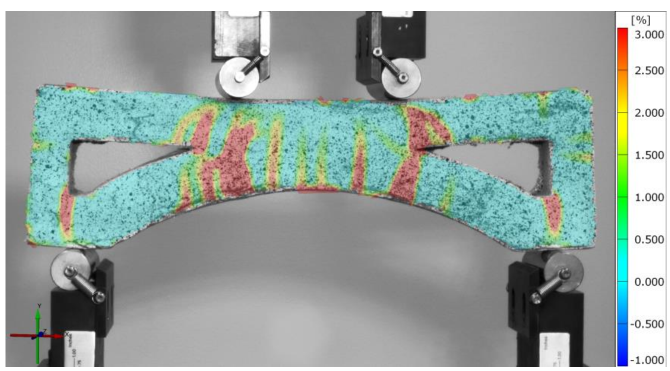

Figure 61: Major strain field in 3D printed topology-optimized beam (Specimen 3D-2) measured by DIC

In the other specimens of the 3D printed topology beams the cracking and strain pattern is very similar to the 3D-2 beam specimen, with some difference in having more stresses in the middle of the catenary arch and not as much under the rollers. This specimen tends to collapse when the critical crack propagates on the middle-lower side of the arch or on the middle-side area under the roller, whether it is the left or right side that collapses is decided by the flaws of the HS-DC material.

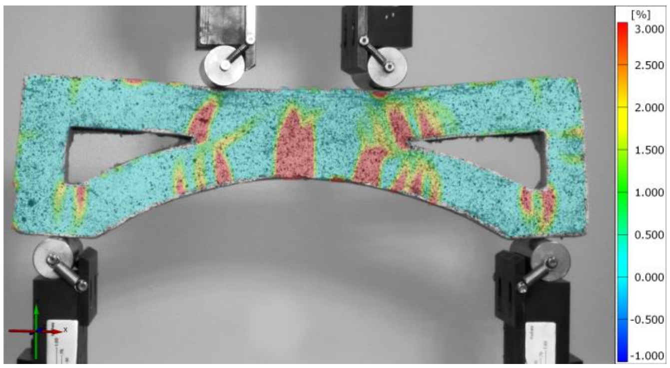

Figure 62: Major strain field of the Specimen 3D-1 at the peak flexural stress

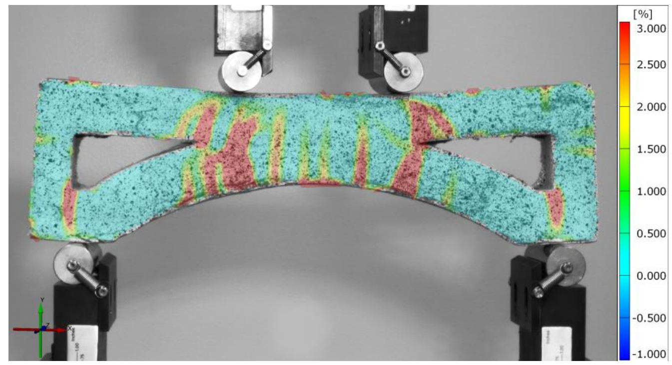

Figure 63: Major strain field of the Specimen 3D-2 at the peak flexural stress

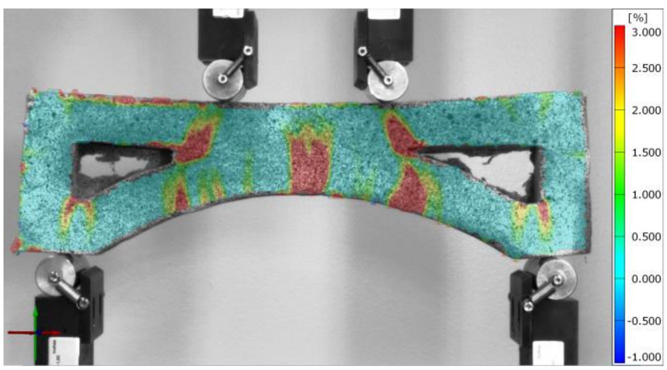

Figure 64: Major strain field of the Specimen 3D-3 at the peak flexural stress

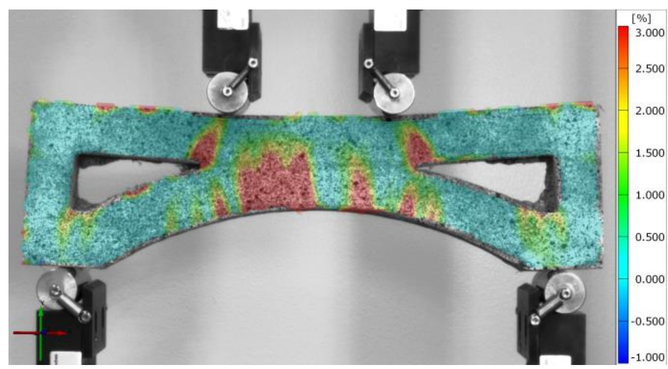

Figure 65: Major strain field of the Specimen 3D-4 at the peak flexural stress

3.3. Flexural behavior of casted high-strength ductile concrete beam with optimized topology

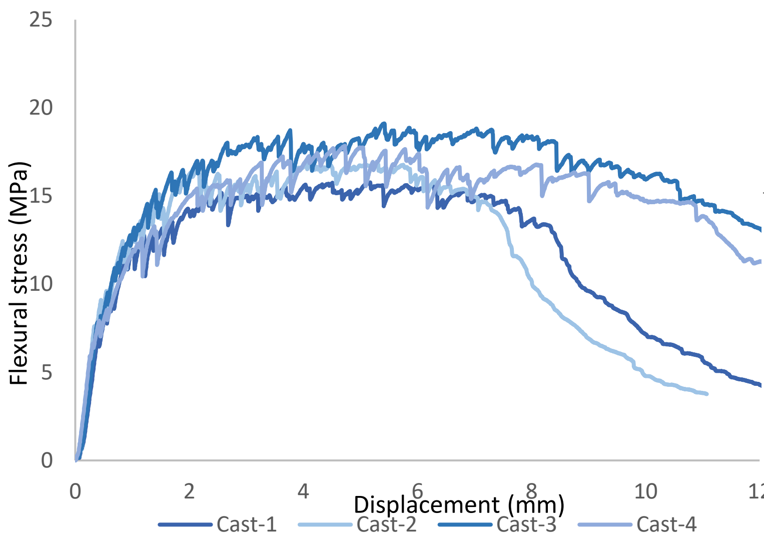

Figure 66: Flexural stress vs. displacement (at roller) curves of casted topology-optimized beams under four-point bending

Table 2: Flexural Strength and displacement capacity values for the casted topology-optimized beams

Repeat Specimen #	*Flexural Strength (MPa)*	*Displacement Capacity (mm)*
Cast-1	15.6	8.2
Cast-2	16.7	7.4
Cast-3	18.6	8.4
Cast-4	17.7	8.9
Average	17.2	8.2

Four specimens of the casted topology optimized beam were also tested under the standard 4-point bending setup. Numbered form Cast-1 to Cast-4 these specimens have the same shape as the 3D printed topology optimized beam but in this case are casted into a mold instead of being 3D printed in the same mold. Due to being casted, these specimens have a homogenously and randomly distributed fibers inside the High-Strength Ductile Concrete s material providing an isotropic properties in terms of strength and ductility. By contrast, in the 3D printed topology beams the process of extruding the HS-DC material through the narrow nozzle produces an alignment of the fibers in the same direction parallel to the printing path, and thus providing an anisotropic behavior, improving the performance of the material in that direction parallel to the printing path as [46], but decreasing in the perpendicular direction.

From the flexural stress – Displacement relation curve of Figure 66 it can be seen that all Casted topology specimens have an elasto-plastic behavior similar to the 3D printed topology specimens. Starting with an initial linear relation with an average slope of 20.6 MPa/mm until reaching a displacement of 0.31 mm and a flexural stress or equivalent yielding point of 6.4 MPa (Figure 68). After that displacement, the slope of the curve decreases and begins the strain-hardening stage initiating the propagation of the first microcracks (Figure 69), as discussed before this causes the saw-toothed curve and the small short drops in flexural stress that recovers after each microcrack reaches the steady state. This process makes the specimen to keep increasing the flexural stress until reaching an average peak flexural strength of 17.2 MPa (Figure 70) and an average displacement capacity at rollers of 8.2 mm before the critical crack starts propagating (Figure 71), severely weakening the beam and making it collapse at a larger displacement although it maintains a low residual flexural stress for very long displacements of over 12 mm.

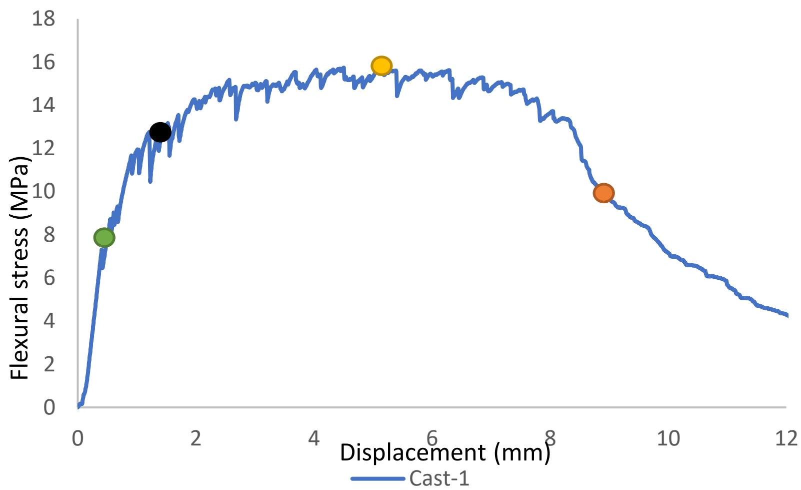

Figure 67: Flexural stress vs. displacement curve for casted topology-optimized beam (Specimen Cast-1). The colored dots mark different displacement levels.

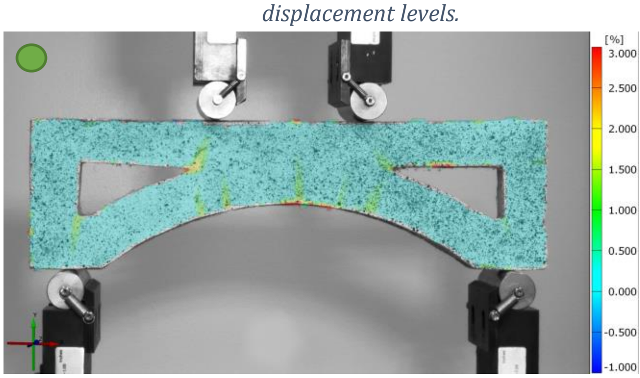

Figure 68: Strain field in Specimen Cast-1 corresponding to the displacement level (green dot) in Figure 67

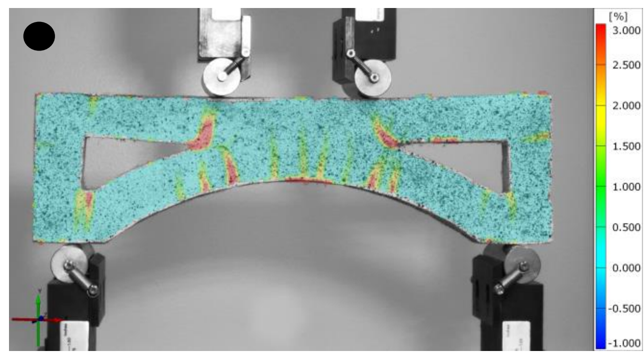

Figure 69: Strain field in Specimen Cast-1 corresponding to the displacement level (black dot) in Figure 67

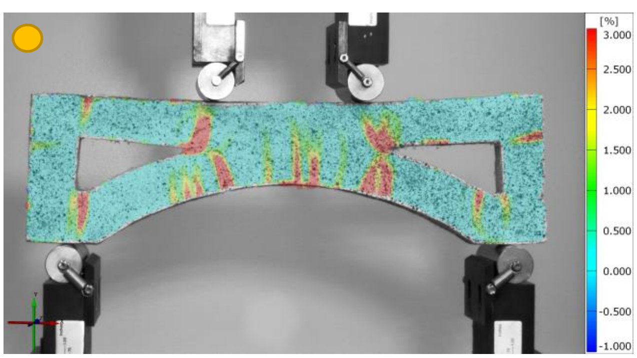

Figure 70: Strain field in Specimen Cast-1 corresponding to the displacement level (yellow dot) in Figure 67

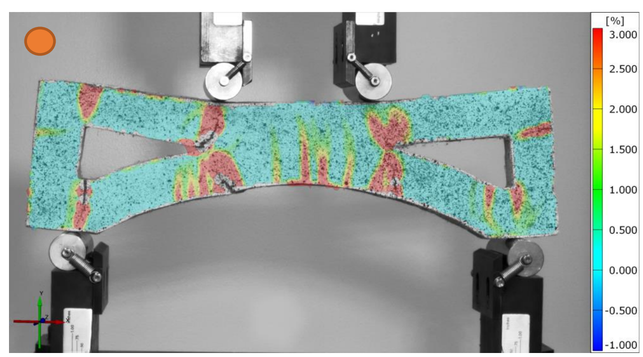

Figure 71: Strain field in Specimen Cast-1 corresponding to the displacement level (orange dot) in Figure

From (Figure 68) to (Figure 71) shows the process of the 4-point bending test at different displacements for the specimen Cast-1. In the beginning of the strain-hardening phase (Figure 68) the microcracks start to propagate at almost the same time in the majority of areas of stress concentration, such as the lower side of the arch and the vertices of the side triangular cavity (Figure 68). As the displacement keeps increasing more microcracks are produced in these same areas of stress concentration besides the ones already existing, and thus enlarging the high strain areas shaded in red in the DIC major strain field that correlates to an agglomeration of microcracks (Figure 69). Some of the microcracks in these agglomerations remain in a steady state with a constant aperture and length, while the newly formed microcracks are still propagating and opening until reaching a steady state later.

There are a few cracks that starts propagating on the exterior sides and upper side of the beam, which are not the main areas of stress concentration get strained and microcracked after large displacements. When the flexural stress reaches its peak all the microcracks are in a steady state (Figure 70) but after a further increase of displacement in the areas with the most stresses and with the biggest flaw or weaknesses there are some cracks that leaves the steady state, becoming a critical crack that starts expanding and leading to the collapse of the beam (Figure 71). Moreover, it appears that in some cases more than one critical crack can be developed in different areas at the same time or later on while the beam is collapsing.

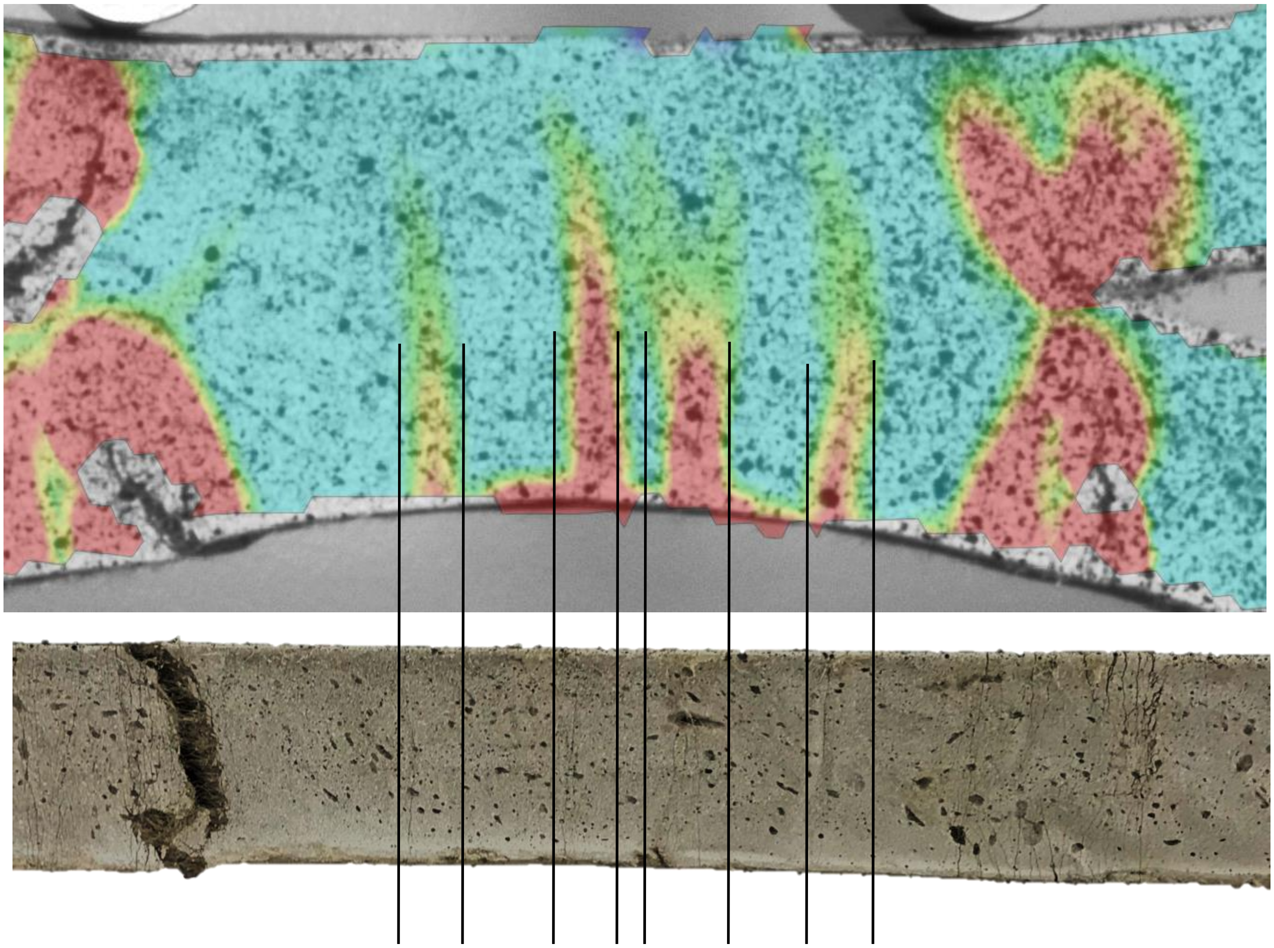

Figure 72: Front surface major strain field (top) and bottom surface damage pattern (bottom) in Specimen Cast-1

In Figure 72 there is represented the DIC major strain field of the front side of the specimen Cast-1 compared to an image of the same beam from the underside aligned, so it can be seen that in the red shaded areas of these DIC major strain concentration areas there are many microcracks grouped together, sometimes forming thin red stripes or thicker larger high strain areas shown in red in DIC. However, in both cases they are the result of the agglomeration of all the microcracks whose gap of each microcrack combined forms a larger strain.

3.4. Flexural behavior of prismatic casted high-strength ductile concrete beam with the same total volume (no topology optimization)

Four beam specimens were produced and tested having a conventional prismatic shape, to be later compared its behavior to the topology optimized geometry beam. For both beam geometries to be comparable, the prismatic casted beams were produced with the same total weight, volume, and maintaining the same length to fit the standard 4-point bending test, of 12 inch of span between rollers and 1 inch thickness. The width of the beam was adjusted to have the same weight and volume as the topology optimized beam.

These four specimens numbered PTV-1, PTV-2, PTV-3 and PTV-4 were tested with the same methodology as the other beams, a standard 4-point flexural bending test at a constant displacement speed of 0.05 mm/s and being recorded using a DIC in order to obtain its major strain field.

Table 3: Flexural Strength and displacement capacity values for the prismatic beams with the same total volume as the topology-optimized beams

Repeat Specimen #	*Flexural Strength (MPa)*	*Displacement Capacity (mm)*
PTV-1	15.9	4.4
PTV-2	18.6	3.9
PTV-3	19.3	4.5
PTV-4	17.3	4.8
Average	17.8	4.4

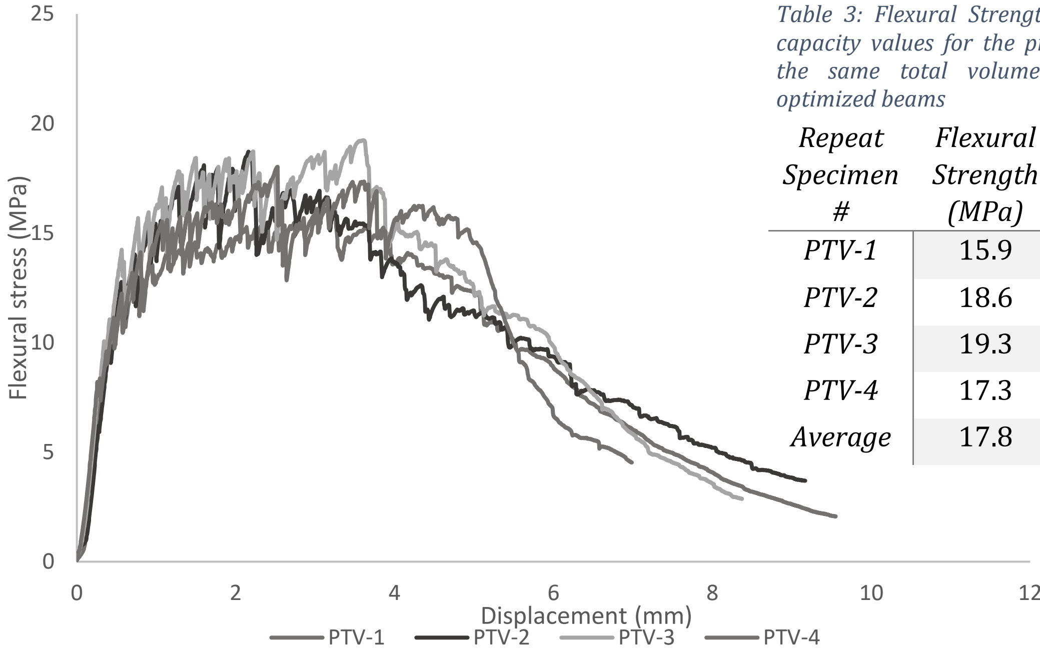

Figure 73: Flexural stress vs. displacement (at roller) curves of casted prismatic beams with the same total volume as topology optimized beams

The beam specimens with a prismatic geometry having the same total volume and weight as the topology optimized beams also show an elasto-plastic behavior in the flexural stress -displacement relation obtained from the standard 4-point bending test results. There is an initial elastic and linear relation stage with a slope of 25.6 MPa/mm until the yielding point at a flexural stress of 7.7 MPa and a displacement of 0.3 mm. Then begins the strain-hardening stage reaching an average peak flexural strength of 17.8 MPa at an earlier displacement of around 2 mm. After this peak, the flexural stress decreases at a small rate until reaching an average displacement capacity of 4.4 mm of displacement, which is the point after that the critical crack starts to propagate and causing the collapse of the beam, and thus the flexural stress decreases at a high rate.

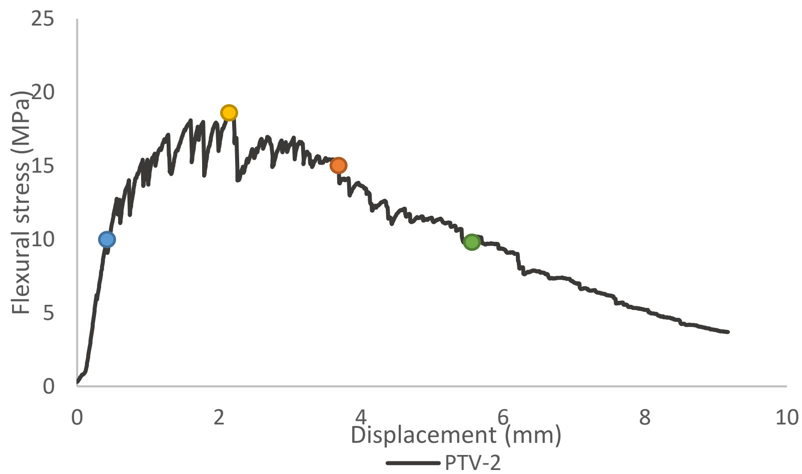

Figure 74: Flexural stress vs. displacement curve for casted prismatic beam (Specimen PTV-2). The colored dots mark different displacement levels.

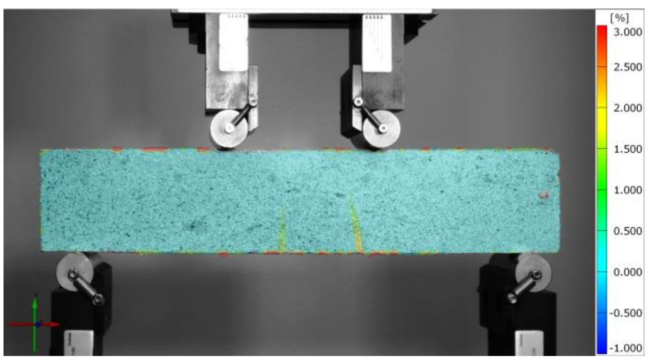

Figure 75: Major strain field in Specimen PTV-2 corresponding to the displacement level (blue dot) in Figure 75

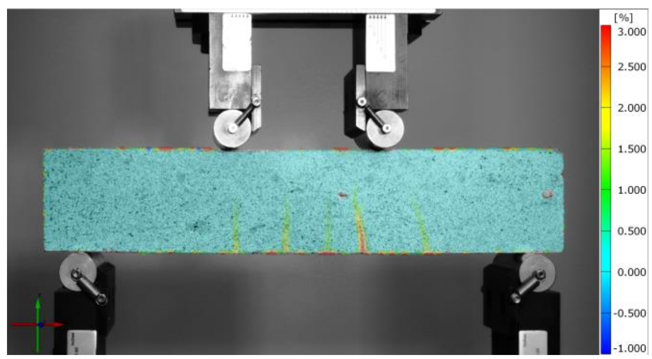

Figure 76: Major strain field in Specimen PTV-2 corresponding to the displacement level (yellow dot) in Figure 75

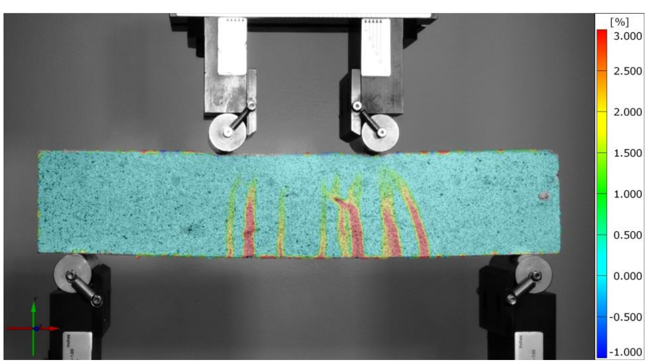

Figure 77: Major strain field in Specimen PTV-2 corresponding to the displacement level (orange dot) in Figure 75

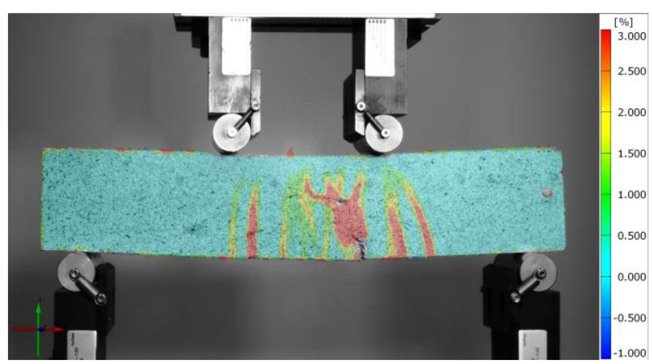

Figure 78: Major strain field in Specimen PTV-2 corresponding to the displacement level (green dot) in Figure 75

The Figure 74 shows the flexural stress -displacement relation for the 4-point bending test of the prismatic same total volume beam, with four color dots placed at different stages of the test in the flexural stress -displacement graph that corresponds to the major strain field of the images from Figure 75 to Figure 78 obtained from the DIC.

The first blue dot is placed on the yielding point that corresponds to the major strain field shown in Figure 75 where can be appreciate the first cracks are propagating on the central lower part where the tensile stresses are the highest due to the setup of this test that produces the highest bending moment between the two central rollers. As the displacement increases more microcracks are propagated but the propagation stops at around ¾ of the width of the beam and then remain as steady state cracks reaching the peak flexural strength at the yellow dot position (Figure 76), then the beam reaches its maximum displacement before collapsing at the orange dot in Figure 77. Each sudden drop in the flexural stress curve represents a microcrack that is propagating and it recovers the original flexural stress when it reaches the steady state of the opening and length ,until the critical crack abandons its steady state due to the critical flaw or weakest area of the beam that causes the collapse as shown in Figure 78, that corresponds to the green dot at the flexural stress -displacement graph (Figure 74).

Examining the critical crack in the principal strain field of Figure 78 and from the reverse side from a close up photography (Figure 79) it can be seen that it is not just a microcrack that is propagating beyond the steady state, but that it crosses other microcracks with a diagonal path following the weakest regions of the beam with the biggest flaws.

Figure 79: Close-up front view of final failure region in prismatic beam (Specimen PTV-2)

3.5. Flexural behavior of prismatic casted high-strength ductile concrete beam with the same effective volume (no topology optimization)

Four more specimens were produced and tested under the 4-point flexural bending setup having a prismatic shape. In this case the specimen was designed such the area between the two rollers of the 4-point bending test, as shown in the red shaded region in the Figure 80 with a span of 12 inch, had the same volume as in the topology optimized beam specimens while maintaining the total length of 14 inches and thickness of 1 inch. The section between the rollers is the effective volume as it takes most of the stresses. The parts outside this area do not stand as much stresses, due to the standard 4-point bending test setup does not apply forces on these areas. Therefore, the "effective volume" is defined as the volume between the outside rollers.

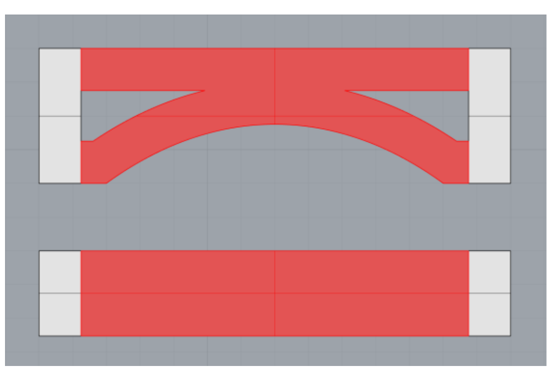

Figure 80: Representation of the topology-optimized beam and the prismatic beam with the same effective volume between two supports (red region)

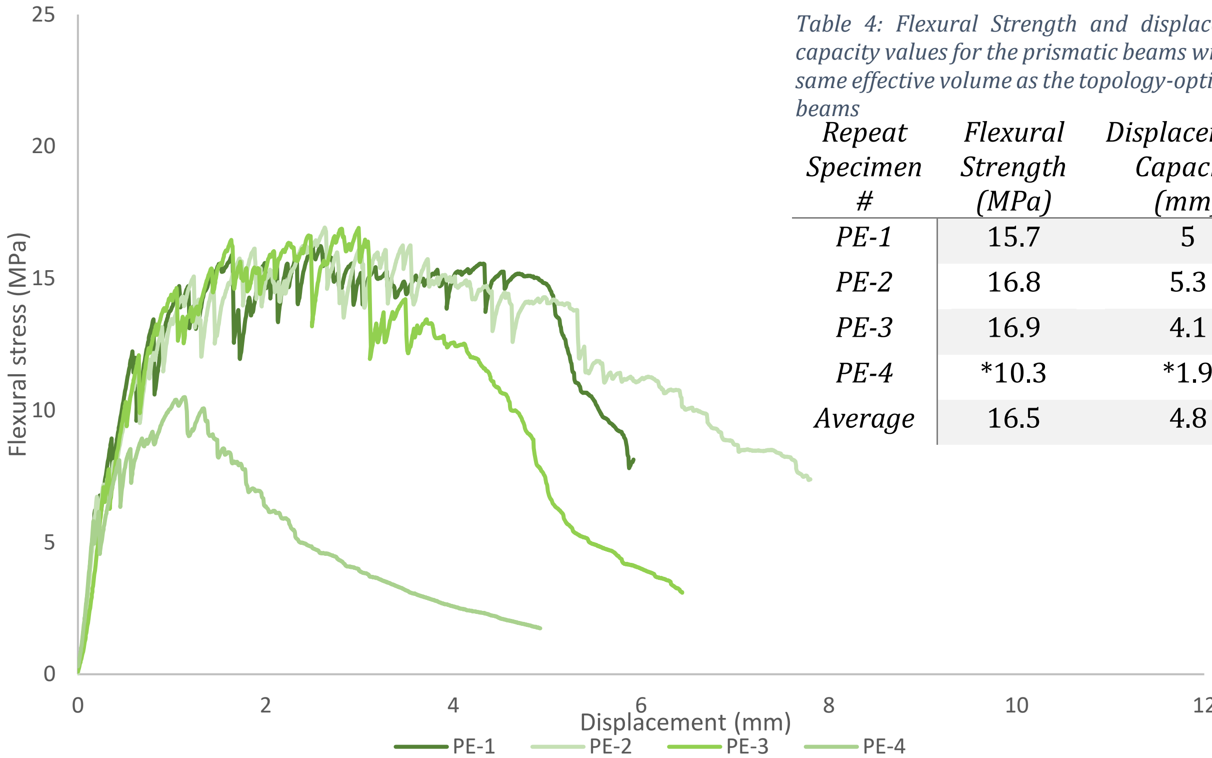

Table 4: Flexural Strength and displacement capacity values for the prismatic beams with the same effective volume as the topology-optimized beams

Repeat Specimen #	*Flexural Strength (MPa)*	*Displacement Capacity (mm)*
PE-1	15.7	5
PE-2	16.8	5.3
PE-3	16.9	4.1
PE-4	*10.3	*1.9
Average	16.5	4.8

Figure 81: Flexural stress vs. displacement (at roller) curves of casted prismatic beams with the same effective volume as topology optimized beams

The four prismatic effective volume beam specimens are numbered PE-1 to PE-4. The results from the standard 4-point bending test are shown in Figure 81 that represents the flexural stress -displacement curve. Like in the other types of specimens under the standard 4-point bending test these also have an elasto-plastic behavior, with an initial elastic and linear stage with a slope of 25.7 MPa/mm until reaching the yielding point at 5.41 MPa at a displacement of 0.21 mm. Then the strain-hardening behavior increases the flexural stress until an average peak strength of 16.5 MPa and reaching a displacement capacity at rollers before starting to collapse of 4.8 mm. The specimen PE-4 is not considered in the calculations of these performance values as it has a behavior too far from the average and it is considered a defective specimen, but it can also be studied to understand how these specimens can fail and have a lower performance than the expected.

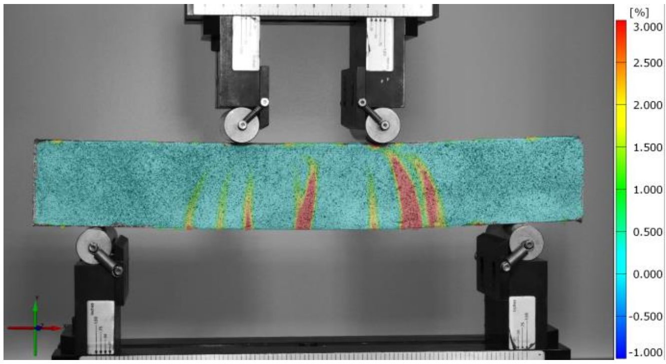

Figure 82: Major strain field of the Specimen PE-1 before critical cracking

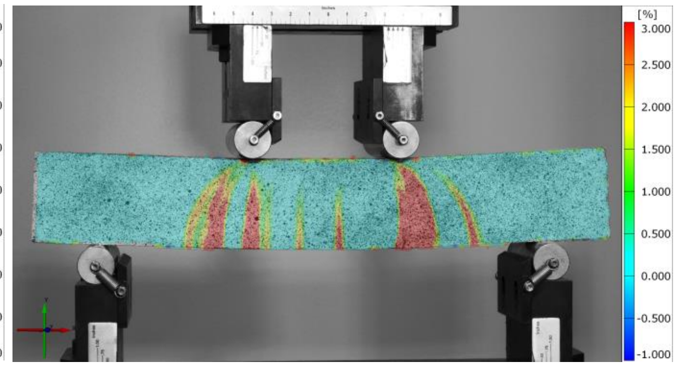

Figure 83: Major strain field in Specimen PE-2 at the peak flexural stress

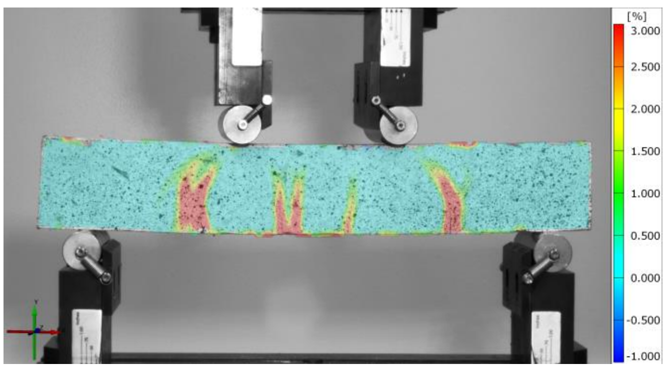

Figure 84: Major strain field in Specimen PE-3 at the peak flexural stress

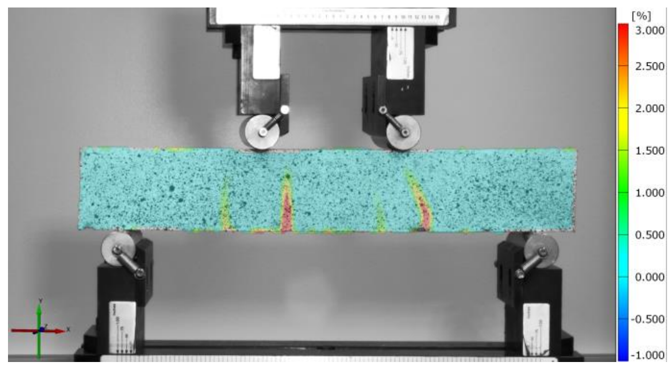

Figure 85: Major strain field in Specimen PE-4 at the peak flexural stress

The images above Figure 82 to Figure 85 show the major strain field form the DIC camera for every prismatic effective volume specimen just before the critical crack starts to propagate and causing the failure of each beam. As it is a prismatic beam and is being subjected to bending, the moment is highest between the upper rollers, causing high compression stresses on the top and tensile stresses on the underside where a multicracking pattern is formed. These cracks tend to group under the middle section rollers and the cracks that are situated outside the central area between the rollers have a certain inclination towards the center, indicating that besides tensile stresses there are also high shear stresses concentration, causing the microcracks and strain field to curve toward the center of the beam.

The specimen PE-4 shown in Figure 85 has an abnormal low performance in both flexural strength and displacement capacity, a clear indication of this poor performance is that it presents very few cracks and the critical crack starts propagating soon, causing an early collapse of the beam. Some possible reasons of this low performance could be due to a poor dispersion of the fibers inside the cementitious matrix, but because all the other specimens are made with the same material batch this possibility seem unlikely. The most reasonable explanation is that during the process of casting of the PE-4 specimen some major flaws were generated and the fibers in some region could get disconnected due to casting and not being able to bridge correctly the cementitious matrix in the flawed areas.

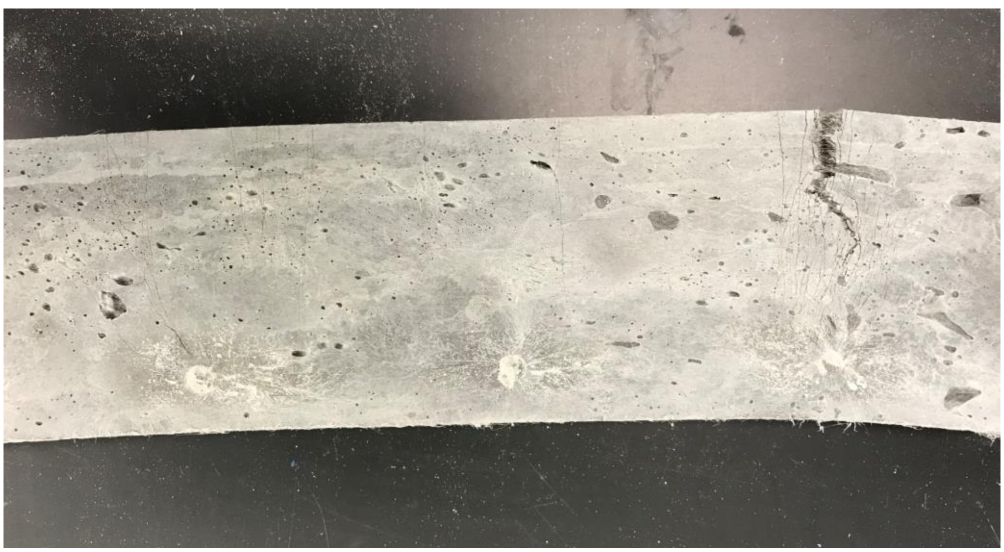

Figure 86: Close-up front view of final failure region in casted prismatic beam (Specimen PE-2)

3.6. Discussion of the effects of topology optimization and 3D printing on the beam flexural behavior

Four types of beam specimens were designed to be subjected to the standard 4-point bending test, with two different geometries: a conventional prismatic shaped beam and a topology optimized beam shape. By comparing the performance of these two geometries it can be deduced the effects of this specific topology optimization in terms of strength, ductility, stiffness, collapse mechanism and stress distribution. In a similar manner, the different types of beams are 3D printed or casted, so the study of the effects of 3D printing of High-strength Ductile Concrete can be deduced by comparing 3D printed beam specimens to casted specimens having both the same geometry.

The following Figure 87 shows all the results from the standard 4-point bending test for all types of beams, having 4 3D printed topology specimens (red curves), 4 Casted topology (blue curves), 4 prismatic same total volume beam (black curves) and 4 prismatic effective volume beams (green curves). In addition, an average curve for every type of beam was calculated by taking the average of the flexural stress of each type of beam for every displacement. The average curve is represented in the same color as the individual specimen type but in a thicker line that helps to visualize the average performance of all specimen types. In the Table 5 is calculated the average peak flexural strength for every kind of beam and its displacement capacity at rollers. Moreover, it shows the average slope of the initial elastic stage for every group of beams, which represent the stiffness in which the beam deflects.

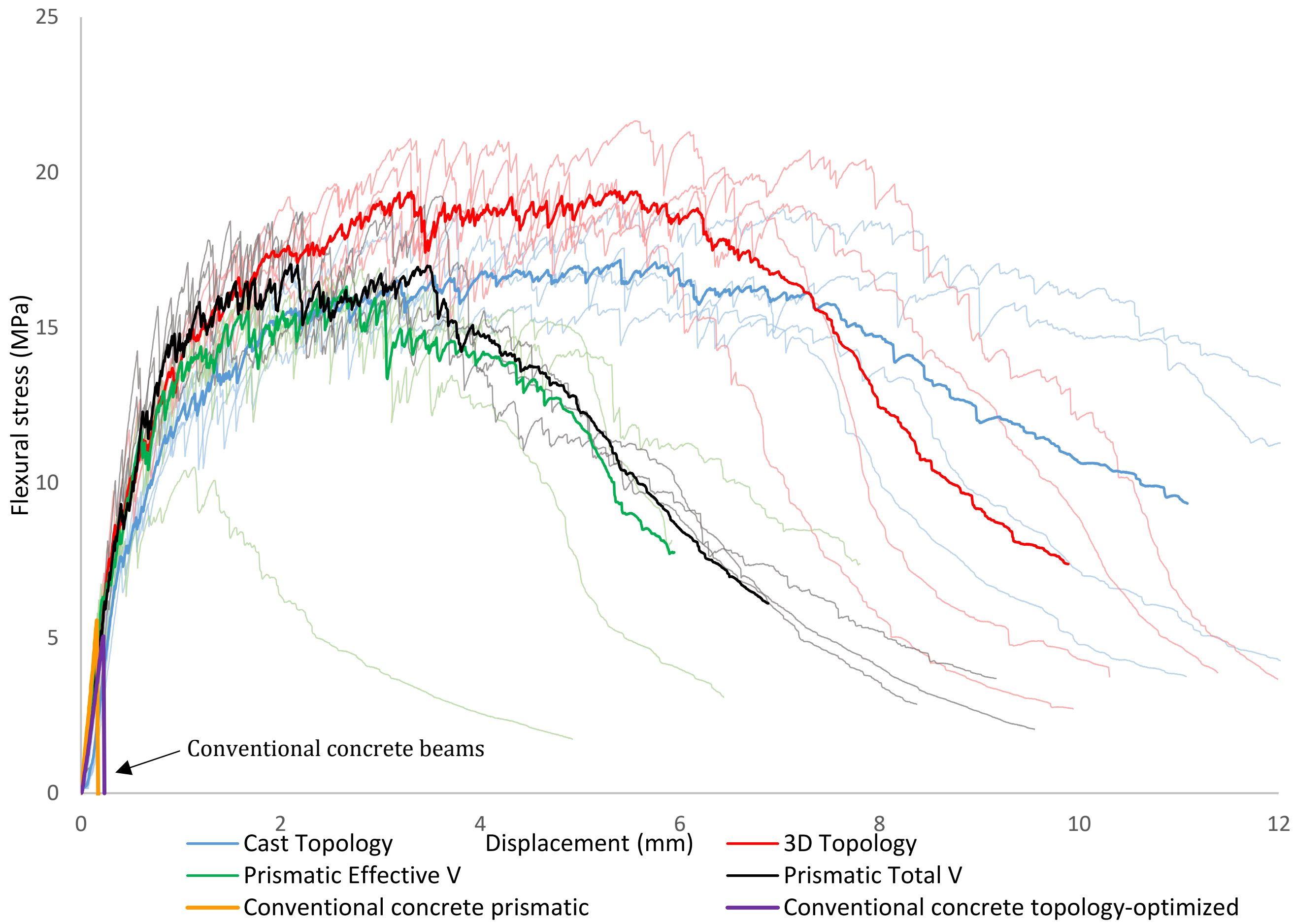

Figure 87: Comparison of all results from four-point bending test. "Cast Topology" stands for casted optimized-topology beams. "3D Topology" stands for 3D printed topology-optimized beams. "Prismatic Effective V" stands for casted prismatic beams with the same effective volume between supports as topology-optimized beams. "Prismatic Total V" stands for casted prismatic beams with the same total volume as topology optimized beams. "Conventional concrete" stands for beams produced without fibers .

Table 5: Comparison of the flexural behavior of four different types of beams made of high-strength ductile concrete

Average values	*Flexural Strength (MPa)*	*Displacement Capacity (mm)*	*Initial Stiffness (MPa/mm)*
3D Topology	20.1	7.5	23.2
Casted Topology	17.2	8.3	20.6
Prismatic Total V	17.8	4.4	25.6
Prismatic Effective V	16.5	4.8	25.7

Examining the flexural stress -displacement results from all the beam types from Figure 87 it can be seen that the overall behavior of the beams follow the same elasto-plastic pattern, with a linear elastic initial stage, then strain-hardening until reaching the peak flexural strength, after this point there is a slight decrease in flexural stress until the critical crack starts propagating, and then the flexural stress rapidly decreases as the beam collapses at a larger displacements. However, there are some clear differences between types of beams in terms of the ductility, flexural strength and stiffness.

Starting with the effects of the process of 3D printing, it appears from (Figure 87) and the previous Table 5 with the average values, that the 3D printed topology beams have a higher flexural strength compared to the casted topology beam with a 16.8% increase. As the only difference between these two types of beams is that one is 3D printed and the other casted , maintaining the same geometry and material, the improvement of strength in the 3D printed topology specimens is due that the PE fibers during the extrusion from the 3D printing process get aligned in parallel to the extruding direction causing an increase in fibers bridging and reinforcing the cementitious matrix in the same direction. Because the beam was printed and tested longitudinally with respect to the 4-point bending test, the 3D printed beam takes advantage of this increase in strength in that particular direction. However, if somehow the 3D printed beam was tested in a perpendicular direction, the strength would be reduced for the same reason that the fibers would be predominantly aligned in the unfavorable perpendicular direction.

The stiffness of the 3D printed beams is also increased 12.6% on average, effect caused by the same reason as the increased strength. On the other hand, the displacement capacity of the 3D printed specimens is lower than in the casted topology by an average amount of -10.6%, as the property of the ductility tends to be inversely proportional to the Stiffness of a material in this case the 3D printed beam has a stiffer behavior. As explained before the printing path in this geometry is favorable for the 4-point bending test, but using other geometries in which the 3D printing path is perpendicular to the stresses, then the 3D printed beams could have a lower stiffness or strength and a higher ductility as the 3D printed HS-DC is an anisotropic material.

To deduce the effects of the topology optimized geometry, the Casted topology beams are compared to the prismatic same total volume and the prismatic effective volume beams which are also made by casting, and the effect of the 3D printing is not interfering in this comparison. To have the most fair and exhaustive comparison, it has to be taken into account that the material situated on the ends of the beams does not take any stresses under the 4-point bending test. Due to the different amount of material in this region depending on the specimen type, it is expected that the prismatic total volume beam will be the upper limit in terms of performance of the beam as it has the highest amount of material between the rollers which is the region that has to support the stresses.

On the contrary, the prismatic effective volume beams are going to represent a lower boundary of the performance, as the amount of material between the rollers is the same as in the topology optimized beam and it has a lower volume overall. The ideal prismatic beam design for this comparison would be somewhere between the prismatic total volume and the prismatic effective volume but it is difficult to define a certain dimension that would best represent and be comparable between the topology optimized and prismatic shaped beams, so these two types of specimens represents and upper and lower boundary in terms of performance compared to the Casted topology beam. The average performance value between the two prismatic specimens will also be considered in the comparison as it is a median value between the upper and lower performance boundary.

In terms of peak flexural strength the casted topology beam has a slightly lower performance than the prismatic total volume beam by -3.5 %, which represent the upper strength limit. compared to the prismatic effective volume beam, the casted topology beams have a slightly higher peak flexural strength of +4.2% that represents the lower boundary. If the strength is calculated taking the average for both types of prismatic beams averaging the peak flexural strength, then the casted topology beam has a marginally higher strength of +0.2%. This result indicates that the strength increase due to the topology optimized geometry is minimal or it is equal to the prismatic shape due to the experimental error that could skew the results making its performance marginally better or worse.

In terms of displacement capacity the casted topology beams show a much higher performance of +88% compared to the prismatic total volume beam, and +73% compared to the prismatic effective volume beams. The average improvement of performance in displacement capacity with respect to both prismatic beams is +80%. This major increase in displacement capacity is explained as the topology optimized geometry is formed by two thinner segments of material that joins in the center of the beam, and for the same amount of displacement the thinner sections produce less strain and stresses, specially on the border. So the ductility in thinner HS-DC sections is greater compared to thicker sections in the prismatic effective volume beams. The thicker sections produces larger strains peaking at the boundary where the microcracks start propagating (Figure 88), and in the end the beam collapses at a lower displacement in the 4-point bending test. This effect is corroborated as the thicker prismatic total volume beam has a lower displacement capacity by 9% than the prismatic effective volume beam which is thinner. The total strength of the topology optimized beam is not compromised by the individual thinner sections as it is formed by two of them that work together, so in the end equalizes the prismatic geometry strength as shown in the results in the previous paragraph.

The stiffness of the linear elastic region is reduced for the casted topology optimized beam compared to the prismatic beams by -24% due to the thinner local sections of the Topology optimized geometry the global stiffness is reduced.

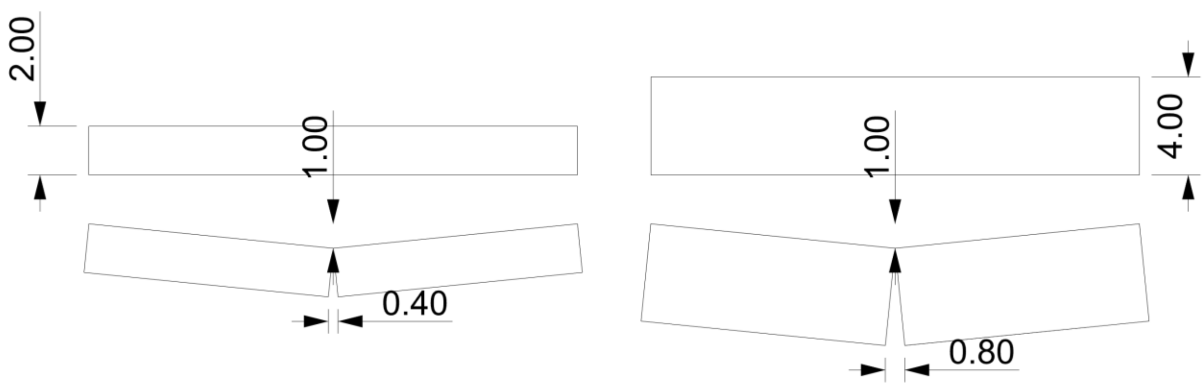

Figure 88: Geometric explanation that for two beams with a different thickness, the strain on the boundary of the beam for the same displacement is bigger in the thicker prismatic beam

In addition, the Figure 87 includes the flexural stress -displacement relation for two beams specimens produced using only the HS-DC cementitious matrix without any fibers, which is then similar to conventional high strength concrete. These two specimens are the "No fibers casted topology beam" (orange curve) and the "No fibers prismatic effective volume beam" (purple curve). In which the ductility is reduced by a factor of 20 and the strength is also reduced by a factor of 3, showing the great impact of the fibers and the increase in performance of the HS-DC over conventional high strength concrete which is brittle.

3.7. Modified four-point bending test with addition horizontal constraints at supports

A modification from the standard 4-point bending test was designed in order to restrain the lateral displacement of the beam using a metal clamp, so that the boundary conditions of the topology optimized beam would be equivalent to the conditions set in the Abaqus model during the topology optimization process. With this modification it is expected to greatly improve its performance as the catenary arch geometry would distribute the stresses in its optimum setting, as this geometry was specially designed with the topology optimization process from the FEM software with these same boundary conditions.

The clamp fixture consists of a steel piece that extends all the longitude of the beam and is supported over the lower 4-point bending test rollers. On the sides of the fixture the geometry extends to fit the 14 inch long beam specimens that in turn are supported over the fixture in a step like shape that is curved separated by 12 inch that acts as a lower roller. With these two elements the specimens have the longitudinal displacement restricted and are as well supported in an equivalent setup acting as the lower rollers from the standard 4-point bending test

Figure 89: Steel clamp fixture that restrains the horizontal displacement of the beam specimens at both supports

Figure 90: Modified 4-point bending test setup with additional horizontal constraints at both supports

3.8. Flexural behavior of 3D printed high-strength ductile concrete beam with optimized topology (with additional horizontal constrains at supports)

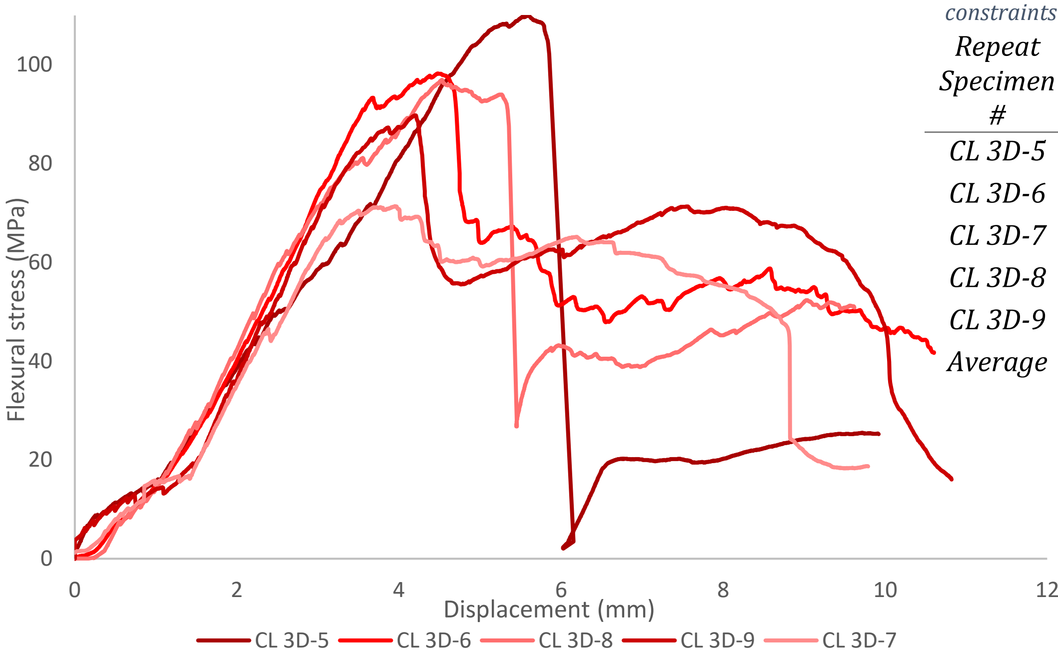

Figure 91: Flexural stress vs. displacement (at roller) curves of 3D printed topology-optimized beams with additional horizontal constraints

Table 6: Flexural strength and displacement capacity values of 3D printed topology-optimized beams with additional horizontal constraints

Repeat Specimen #	*Flexural Strength (MPa)*	*Displacement Capacity (mm)*
CL 3D-5	109	5.8
CL 3D-6	96	4.7
CL 3D-7	71	4.6
CL 3D-8	95	5.4
CL 3D-9	90	4.3
Average	92	5

Five specimens of the kind 3D printed topology were subjected to the clamped 4-point bending test using the steel fixture to restrain its lateral displacement, numbered CL (for clamped) from 3D-5 to 3D-9. The rest of the parameters such as the displacement rate of 0.05 mm/s is the same as in the standard 4-point bending test.

The Figure 91 shows the flexural stress -displacement relation for the clamped 4-point bending test of the five clamped 3D printed topology beams in different shades of red. For an initial small displacements it shows a linear elastic relation with an slope of 31.9 MPa/mm, better seen in Figure 92 that represents the same flexural stress -displacement relation but focused for very small displacement for the specimen CL 3D-5. At a displacement of 0.26 mm the elastic trend deceases at a yielding point of 6.7 MPa, after which the strain-hardening stage begins with a sawtooth pattern, indicating that microcracks are being formed but the stress are still being recovered at every dip in flexural stress, with an overall slope of 10 MPa/mm.

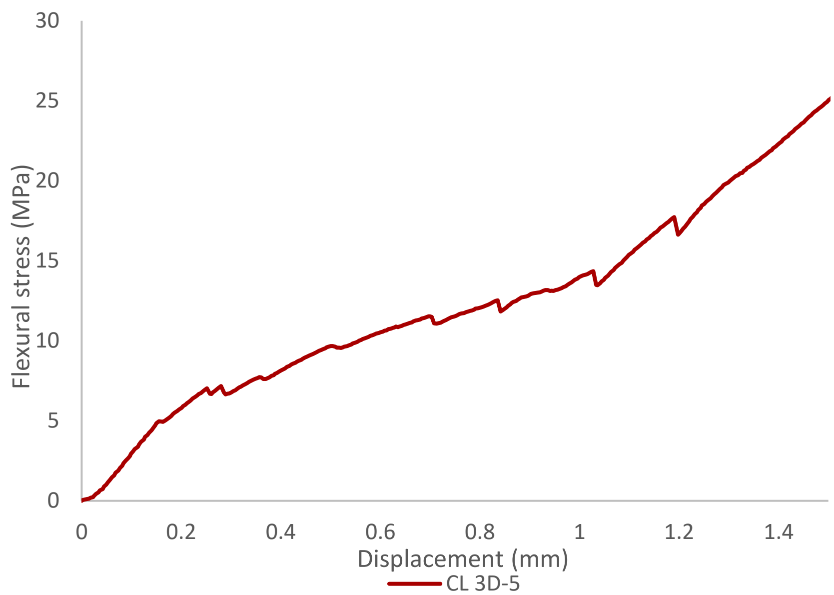

Figure 92: Initial part of the flexural stress vs. displacement curve for Specimen CL 3D-5 showing the initial elastic region, strain-hardening and compression stage

Until this point the behavior in the clamped 4-point bending test of the 3D printed topology beams is very similar to the standard 4-point bending test having an elastic initial stage and then an increasing flexural stress strain-hardening phase. But after a displacement of 1.05 mm and a flexural stress of 13.9 MPa the slope of the curve increases significantly to 24.5 MPa/mm, at this phase the steel clamp that fits the beam starts to react to the lateral forces produced by the beam which as a reaction it creates compressive stresses back in the beam reducing the tensile stresses on the lower side of the beam arch, and thus increasing the stiffness and strength of the beam. In this case the strength of the 3D printed topology beam is greatly increased achieving an average peak flexural strength of all the 3D printed topology beams of 92 MPa and a displacement capacity at rollers of 5 mm. At this point there are microcracks formed along the catenary arch and at the vertices of the stress concentration areas of the side cavities. On one side of the arch there is a high strain area shaded in red from the major strain field that runs along all the right side of the specimen CL 3D-5 (Figure 93), that is mainly formed by shear stresses and later becomes the critical crack that leads to the collapse of the beam.

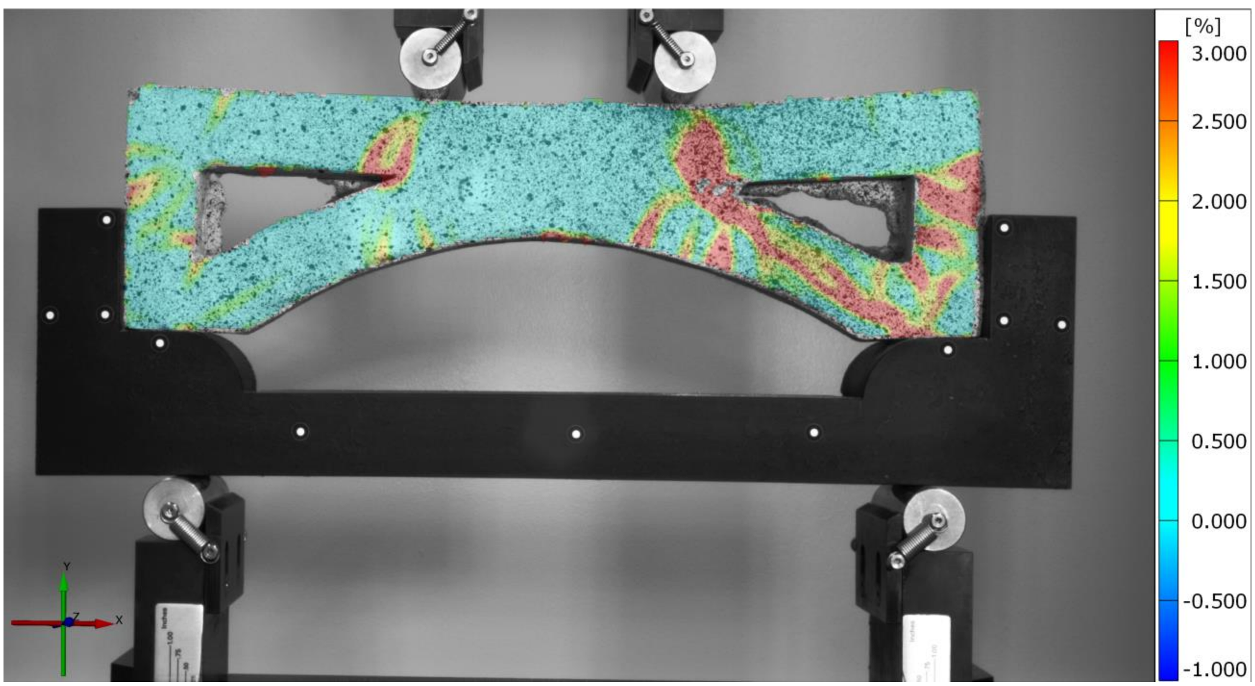

Figure 93: 3D printed topology-optimized beam (Specimen CL 3D-5) at the peak flexural stress under four-point bending

Due to the shear nature of the critical crack, for having an inclination, shown in Figure 94 and Figure 97: Image of damage pattern in Specimen CL 3D-8 after four-point bending test the propagation of the crack is fast and explosive causing a big release of energy, causing loud sound and big loss of strength of more than 90% in the case of the CL 3D-5 and around

50% of the other 3D printed topology beams. The critical shear crack can be propagated along the lower side of the arch of the beam like in the CL 3D-6 (Figure 94) or it can cut perpendicularly through the section of the arch like in the CL 3D-5 specimen (Figure 94). After this fracture the flexural stress drops by more than 50% but then it remains constant until reaching a displacement of 10mm as the clamped and the compression stresses keep all the sections of the beam together. enabling the beam to support some residual loads.

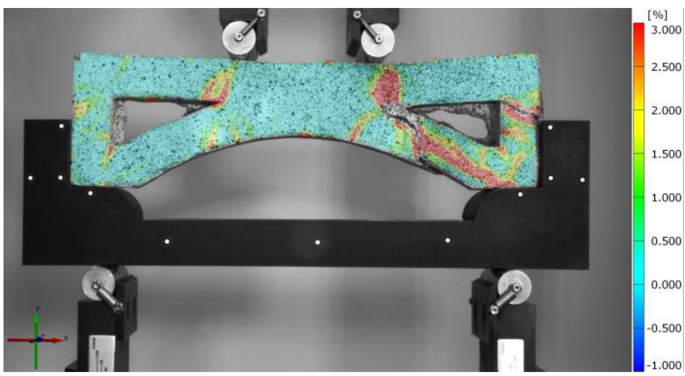

Figure 94: Major strain field of Specimen CL 3D-5 after the critical failure crack has formed in addition to microcracks

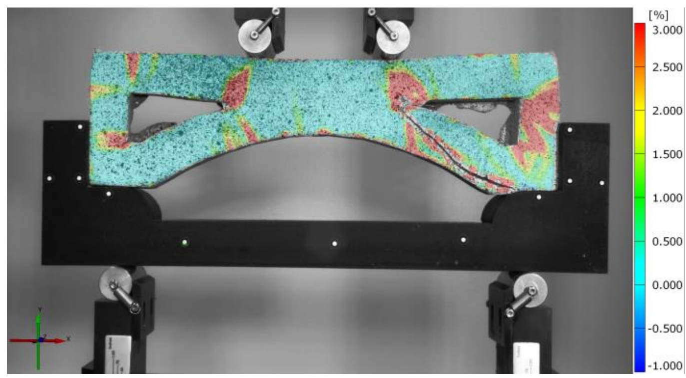

Figure 95: Major strain field of Specimen CL 3D-6 specimen after the critical failure crack has been formed in addition to microcracks

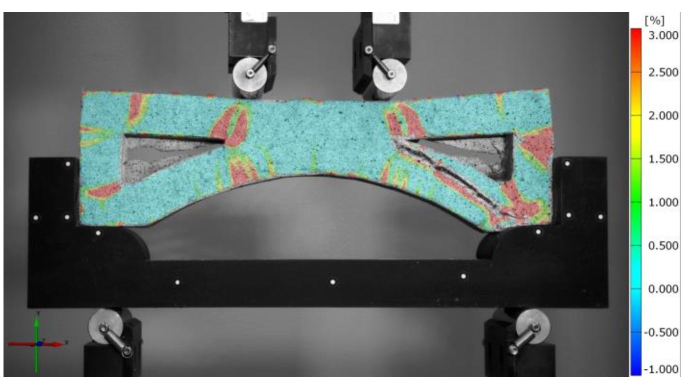

Figure 96: Major strain field of Specimen CL 3D-9 after the critical failure crack has been formed in addition to microcracks

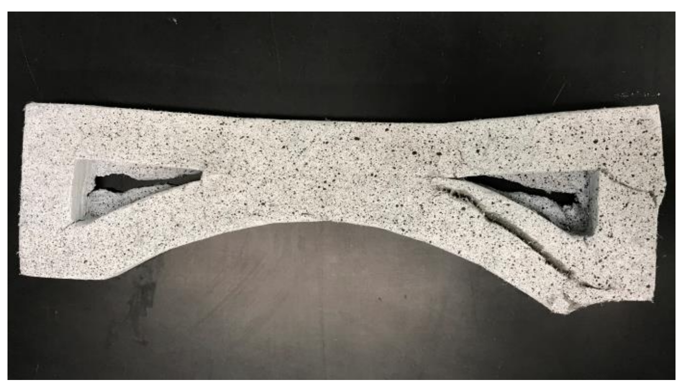
Figure 97: Image of damage pattern in Specimen CL 3D-8 after four-point bending test

3.9. Flexural behavior of casted high-strength ductile concrete beam with optimized topology (with additional horizontal constraints at supports)

Four Casted topology beam specimens, named CL Cast-5 to Cast-8, were tested with the clamped 4-point bending setup. These specimens were casted in a mold using the same High-Strength Ductile Concrete material as the 3D printed topology beams, but in this case the fibers are homogeneously distributed inside the cementitious matrix as they are not extruded through a nozzle that aligns them like during the 3D printing process. That makes the 3D printed topology beam to have an anisotropic behavior compared to the isotropic material behavior of the casted topology beam. The rest of the properties such as geometry, testing setup and displacement rate are the same as in the clamped 3D printed topology beams test.

Table 7: Flexural strength and displacement capacity values of casted topology-optimized beams with additional horizontal constraints

Repeat Specimen #	*Flexural Strength (MPa)*	*Displacement Capacity (mm)*
CL Cast-5	74	3.9
CL Cast-6	95	4.6
CL Cast-7	107	3.5
CL Cast-8	113	4.2
Average	96.5	4

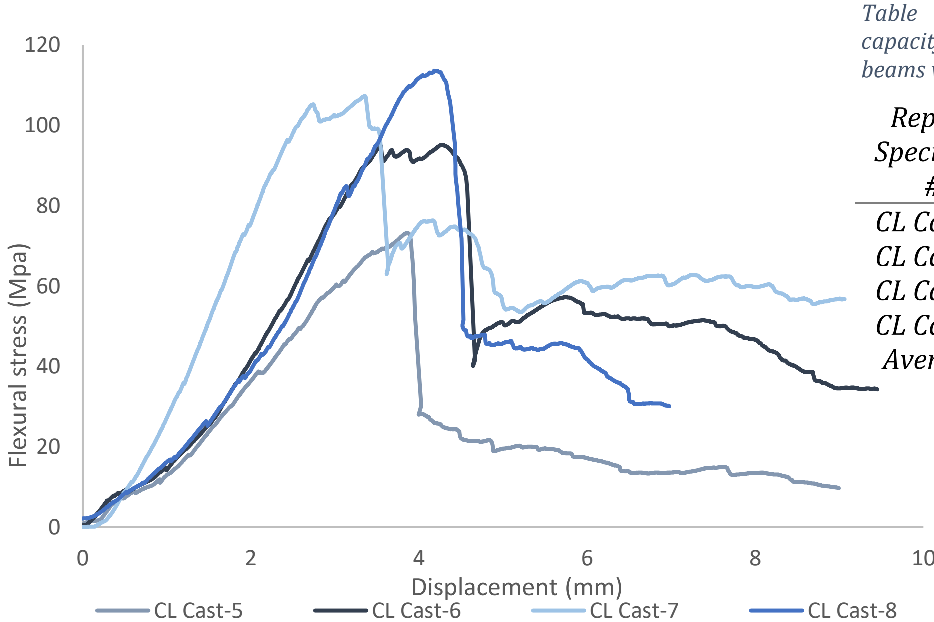

Figure 98: Flexural stress vs. displacement (at roller) curves of casted topology-optimized beams with additional horizontal constraints

The Figure 98 represents the flexural stress -displacement relation for the casted topology beams in the clamped 4-point bending setup, which uses a metal fixture to restrain the lateral movement of the beam and improves its performance as the reaction forces of the clamp compresses the beam and the tensile stresses decreases. Because the HS-DC material and cementitious materials in general have a much better performance in compression than in tension, this clamp fixture takes advantage of this property together with the topology optimized shape of the beam, with its arch shape and lateral confinement significantly improving its strength.

In this case the clamped casted topology beam have a similar response as the 3D printed topology beam, it begins with a small linear elastic stage until reaching a yielding point at a displacement of 0.5 mm and a Moment of rupture of 8.5 MPa (Figure 99). After this point there is a short strain-hardening phase that has the same behavior and properties as in the standard 4-point bending test, because at this phase the clamp is still not being loaded laterally as there are always small gaps between the beam and the clamp so it behaves as the standard 4-point bending test (Figure 98: Flexural stress vs. displacement (at roller) curves of casted topology-optimized beams with additional horizontal constraints) until reaching a displacement of 0.9 mm and an average flexural stress of 12.6.

Then the clamp starts to react to the lateral forces exerted by the casted topology beam. This reaction of the clamp to the lateral deformation of the specimen prevents the beam from deforming laterally, increasing the compressive stresses inside the beam and decreasing the tensile stresses (Figure 101). Because the strain in the compressive regions is relatively small to the tensile strain sections of the HS-DC material, this translates into a very high Young Modulus and strength in compression. Because the HS-DC has a high strength in uniaxial compression of around 100 MPa, which is 10 times higher than in uniaxial tension, taking advantage of this property by the topology optimized shaped beam, with its catenary arch and the whole geometry makes its flexural stress be able to increase to a very high average peak flexural strength of 96.5 MPa and a displacement capacity at rollers of 4 mm.

After the critical crack develops, like in the clamped 3D printed specimens, it causes a large energy release and a sudden decrease in strength, although some residual stresses are left and maintained at a constant level at around 50% of the peak strength, due to the clamp still confining the beam in compression.

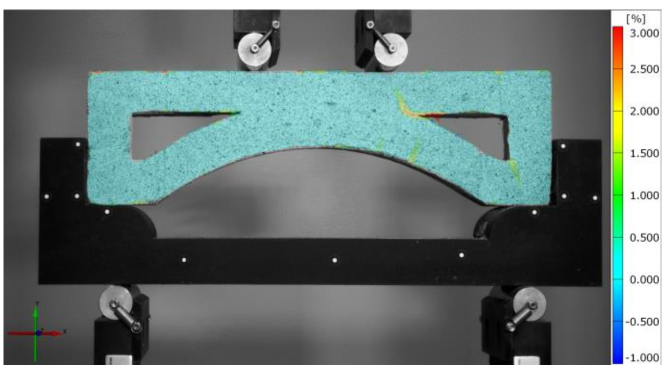

Figure 99: Major strain field of casted topology-optimized beam (Specimen CL Cast-7) when microcracks appeared

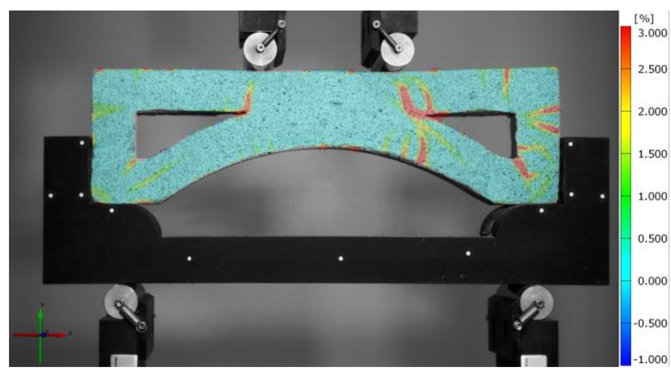

Figure 100: Major strain field of casted topology-optimized beam (Specimen CL Cast-7) during deflection-hardening stage

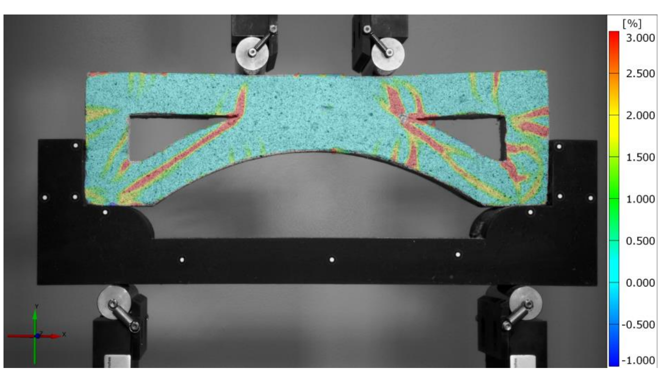

Figure 101:Major strain field of the clamped casted topology beam CL Cast-7 at the peak flexural stress

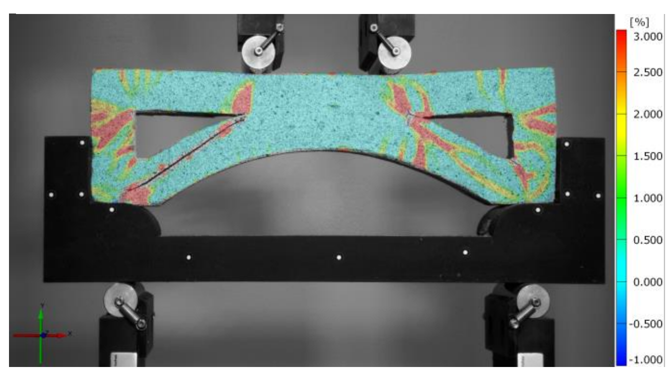

Figure 102: Major strain field of casted topology-optimized beam (Specimen CL Cast-7) after peak flexural stress

3.10. Flexural behavior of prismatic casted high-strength ductile concrete beam with the same total volume (with additional horizontal constraints supports)

The prismatic casted same total volume beams were also tested in the clamped 4-point bending setup. A total of four beam of this type were tested named CL PTV-5 to -8. These specimens are made with the same HS-DC material and were casted in a prismatic mold, having the same total weight and volume as the topology optimized beams.

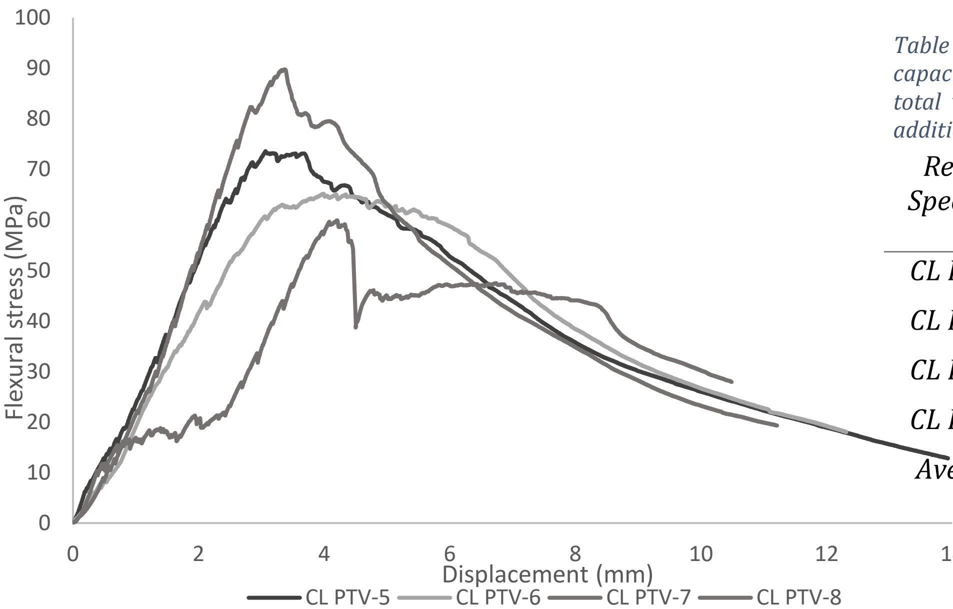

Figure 103: Flexural stress vs. displacement (at roller) curves of casted prismatic beams (with same total volume as topology-optimized beams) with additional horizontal constraints

Table 8: Flexural strength and displacement capacity values of casted prismatic beams (same total volume as topology-optimized beams) with additional horizontal constraints

Repeat Specimen #	*Flexural Strength (MPa)*	*Displacement Capacity (mm)*
CL PTV-5	73	5.2
CL PTV-6	65	6.3
CL PTV-7	90	4.8
CL PTV-8	59	4.4
Average	72	5.2

The Figure 103 represents the flexural stress -displacement relation for the clamped prismatic same total volume beams in curves with different shades of grey. The initial linear elastic region for these specimens is tiny, and for very small displacements (Figure 104) the clamped prismatic same total volume beams already starts to form microcracks and begins the strain-hardening phase with a sawtooth pattern due to the multicracking, and with a general positive and constant slope (Figure 105). The reason this type of specimen have very little elastic zone is due that it is a thicker specimen and for smaller displacements the outer sides of the beam experience bigger strain and stresses than in the topology optimized beam that is formed by thinner sections.

The strain-hardening phase peaks at an average flexural strength of 72 MPa with a displacement capacity at rollers of 5.2 mm (Figure 106). After this peak in strength and unlike in the topology optimized beams, the flexural stress starts gradually to decrease which by comparison in the topology optimized beams a sudden formation of a critical crack released a lot of energy breaking by shear and decreasing the stresses by more than 50%. On the contrary, in this case all the clamped prismatic casted same total volume beam began its collapse with the formation of a critical crack in the middle of the lower side of the specimen (Figure 107), where the biggest tensile stresses are present due to the bending forces. Because in this case the collapse mode of the critical crack is by tensile stresses the flexural stress decreases gradually and not in a brittle manner like in shear failure mode.

Examining the Major strain field for the specimen CL PTV-7 (Figure 106) it can be seen that there are two cracks on the sides of the beam at a 45 degree inclination, indicating that in this area there are shear stresses concentration, but in the end this region does not fail maintaining the steady state of these microcracks caused by shear. During the phase of decreasing flexural stress and leading to the collapse of the beam the region between the upper rollers also collapses and cracks due to compressive stresses indicating that in this area these stresses might be around 100 MPa as it is the failure threshold of HS-DC. These high stresses in compression are cause by the reaction of the steel clamp that confined the beam and does not enable it to expand laterally compressing all the beam but specially the middle section that ends up collapsing (Figure 108).

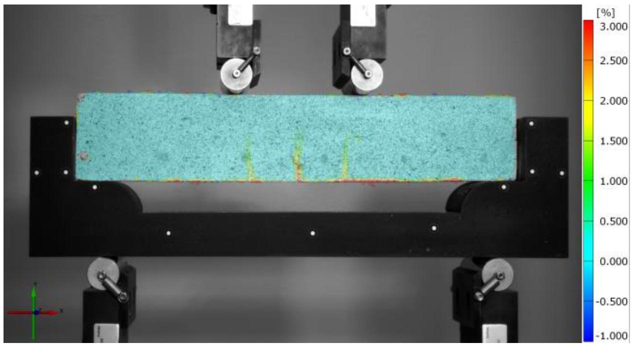

Figure 104: Major strain field of Specimen CL PTV-7 when microcracks formed

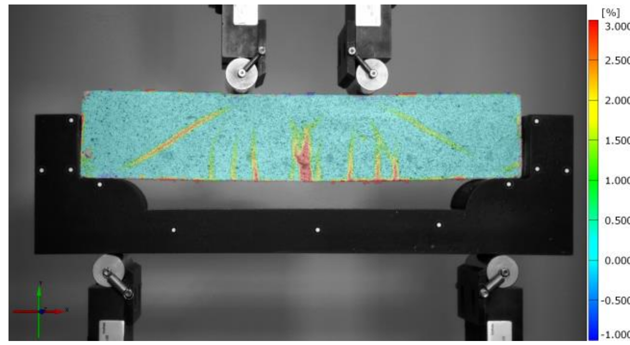

Figure 105: Major strain field of specimen CL PTV-7 during deflection-hardening stage

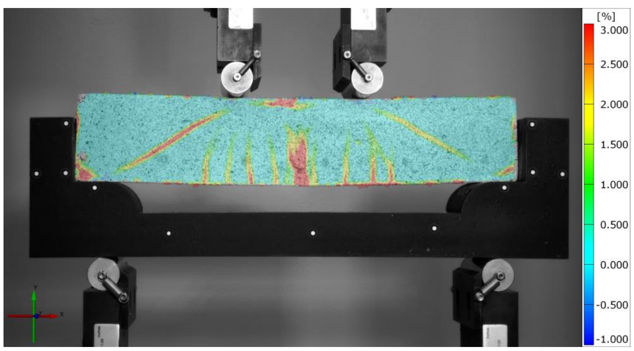

Figure 106: Major strain field of Specimen CL PTV-7 at the peak flexural stress.

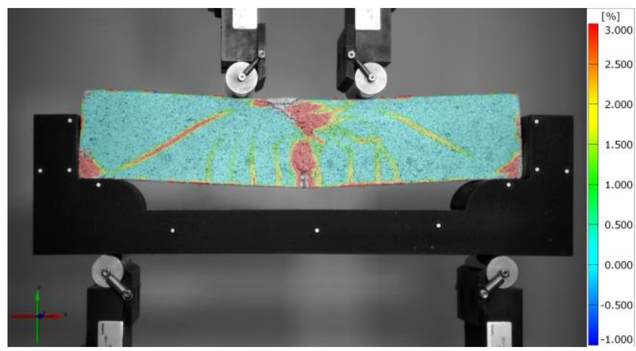

Figure 107: Major strain field of Specimen CL PTV-7 after peak flexural stress and at failure

Figure 108: Close-up front view of final failure region in casted prismatic beam (Specimen CL PTV-7) with same total volume as topology-optimized beams and with additional horizontal constraints at supports.

3.11. Flexural behavior of prismatic casted high-strength ductile concrete beam with the same effective volume (with additional horizontal constraints at supports)

The prismatic casted effective volume specimens are beams with a prismatic shape that have the same length 14” and thickness 1” of that of the other beam specimens but the width is adjusted so that the volume of material between the 4-point bending rollers is the same for this type of specimens and for the topology optimized beams. Four specimens of this type were made and tested in the Clamped 4-point bending setup, named CL PE-5 to CL PE-8.

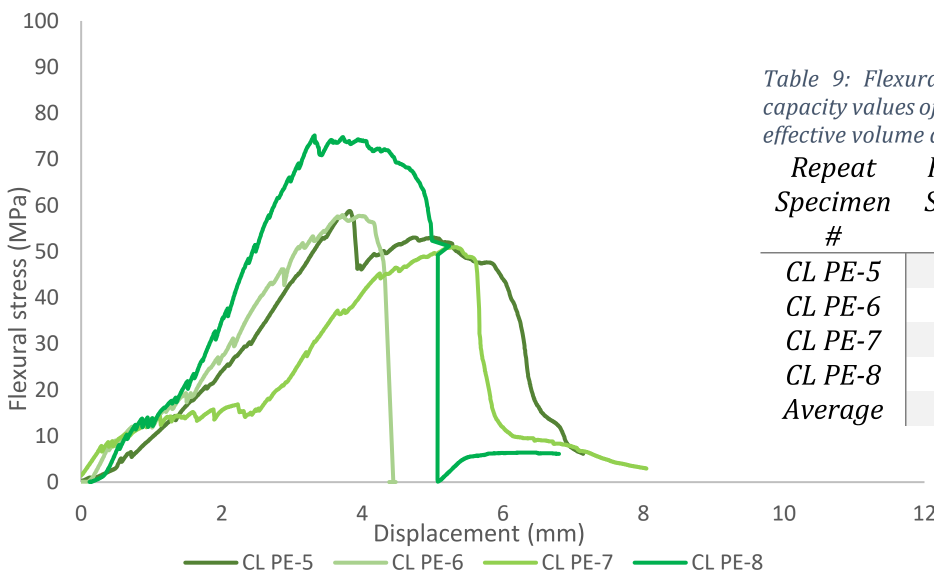

Table 9: Flexural strength and displacement capacity values of casted prismatic beams (same effective volume as topology-optimized beams)

Repeat Specimen #	*Flexural Strength (MPa)*	*Displacement Capacity (mm)*
CL PE-5	58	5.8
CL PE-6	58	4.3
CL PE-7	51	5.6
CL PE-8	75	4.6
Average	61	5.1

Figure 109: Flexural stress vs. displacement (at roller) curves of casted prismatic beams (with same effective volume as topology-optimized beams) with additional horizontal constraints

The flexural stress -displacement relation for the clamped prismatic effective volume beams is shown in Figure 109 and each specimen is represented in a curve colored in different shades of green.

The overall behavior from the flexural stress -displacement relation (Figure 109) is similar to the clamped topology optimized beams, with an initial linear elastic phase, then reaching a yielding point and starting the strain-hardening stage as if it was not clamped. After reaching a certain displacement the steel clamp starts to react to the lateral loads of the beam and the confinement it creates improves the stiffness of the beam increasing the slope of the flexural stress -displacement curve and also rising its flexural strength to an average peak of 61 MPa at a displacement capacity at rollers of 5.1 mm.

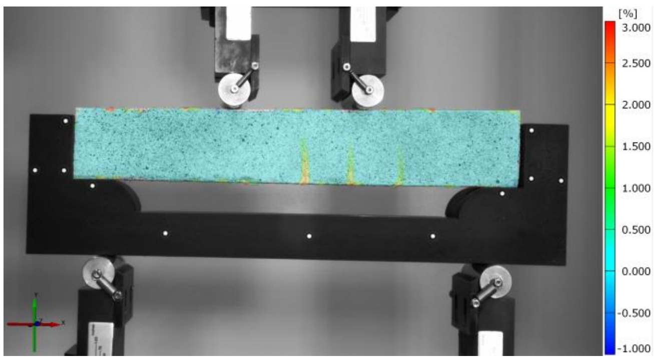

Figure 110: Major strain field in Specimen CL PE-5 when microcracks appeared

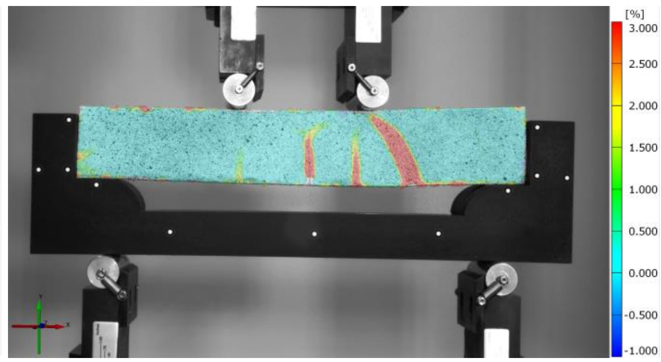

Figure 111: Major strain field in Specimen CL PE-5 during deflection-hardening stage

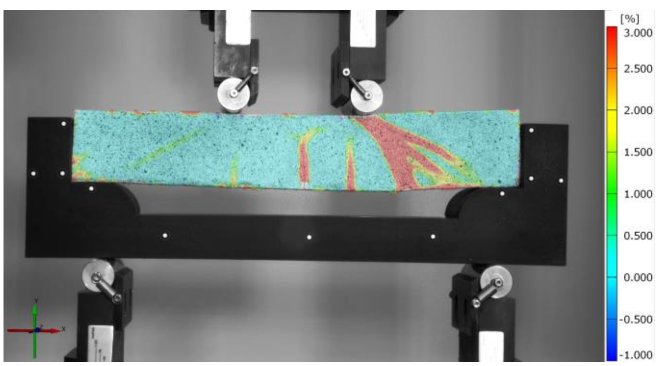

Figure 112: Major strain field in Specimen CL PE-5 at the peak flexural stress

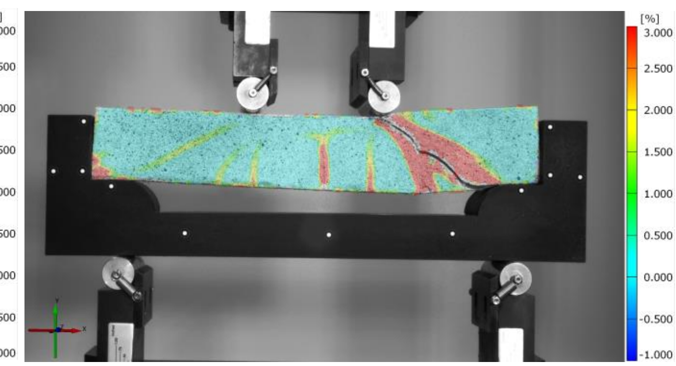

Figure 113: Major strain field in Specimen CL PE-5 at failure stage

After the peak flexural stress the critical crack propagates in a shear mode causing a sudden release of energy and causing a fall of the flexural stress to almost 0 MPa. The shear critical crack connects the two rollers and in both sides of the beam there is a strain concentration stripe inclined at around 45 degrees but only one side of the beam collapses in the end.

All four clamped prismatic effective volume specimens collapse in an abrupt release of energy of the critical crack caused by shear stresses. On the contrary, all the clamped prismatic total volume specimens collapsed due to tensile stresses on the middle of the beam although they also presented shear strain stripes on the same areas like in the prismatic effective volume beam. This completely different mode of failure for such a similar types of beam is due to the width of the beam.

In the case of the clamped prismatic total volume beams being wider it creates more tensile stresses on the lower sides of the beam for the same displacement and also the shear induced steady state cracks have more area to distribute the stresses, so the beam finally collapses due to the tensile stresses and tensile microcracks and not due to shear.

On the other hand, the clamped prismatic effective volume beam is thinner so the shear stresses have a larger impact in respect to the tensile stresses concentration areas which ends in a collapse due to shear in a more brittle way like in the clamped topology optimized beam (Figure 114).

Figure 114: Final failure crack in Specimen CL PE-5 indicating shear-governed failure

3.12. Experimental results discussion and summary

The clamped 4-point bending test was designed to provide the beam specimens with a boundary condition similar to that of the FEM topology optimized process, in which a prismatic beam was simulated in the Abaqus software to be loaded and supported by a clamped boundary condition on the lower side of the beam and the software calculated and generated the most efficient shape that minimized the strain energy inside the beam.

The custom fixture installed in this clamped 4-point bending test restrain the lateral movement of the beams in the longitudinal direction so the reacting forces that prevents this displacement creates compression inside the beam and improving its performance. The topology optimized beams takes this advantage to the optimum condition, making use of and arch like structure which is similar to an inverted catenary shape that distributes the stresses into compression forces acting along the arch in an uniform way.

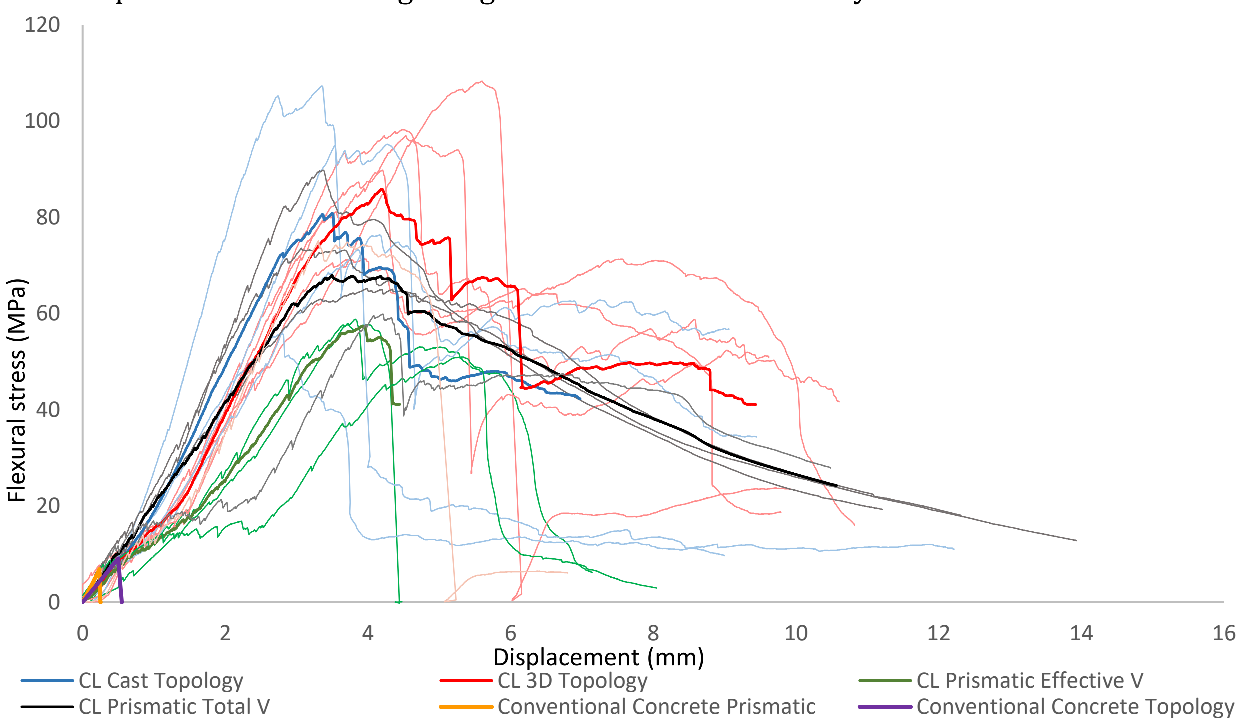

Figure 115: Comparison of all results from modified four-point bending test with additional horizontal constraints at supports. "CL Cast Topology" stands for casted optimized-topology beams. "CL 3D Topology" stands for 3D printed topology-optimized beams. "CL Prismatic Effective V" stands for casted prismatic beams with the same effective volume between supports as topology-optimized beams. "CL Prismatic Total V" stands for casted prismatic beams with the same total volume as topology optimized beams. "Conventional concrete" stands for beams produced without fibers.

Table 10: Comparison of the flexural behavior of four different types of beams made of high-strength ductile concrete, with additional horizontal constraints at supports

Average values	*Flexural Strength (MPa)*	*Displacement Capacity (mm)*
CL 3D Topology	92	5
CL Casted Topology	83	4.4
CL Prismatic Total V	72	4.5
CL Prismatic Effective V	61	4.3

From all the flexural stress -displacement results represented in Figure 115 it can be seen that the topology optimized specimens have a significantly higher flexural strength of 92 MPa for the 3D topology and 83 MPa for the casted topology, compared to 72 MPa for the prismatic total volume and 61 MPa of the prismatic effective volume beam.

The effect of the topology optimization on the strength can be deduced by comparing the Casted topology to the prismatic beams which are made with the same HS-DC material while conserving an homogeneously distributed fibers, because these were casted in a mold. This causes an increase in strength due to the topology optimization which is between 15 % and 36 % depending if it is compared to the prismatic effective volume beams or the prismatic total volume. Like in the previous standard 4-point bending test, there is a central region of the beam between the supports that are more important in supporting the stresses than the material on the sides. So the two types of prismatic beam represent an upper and lower bound for the performance comparison with the topology optimized beam.

The prismatic same total volume beam has a higher amount of material in the middle section between the supports of the beam compared to the topology optimized beam geometry. The prismatic same effective volume has the same amount of material in the middle effective section of the beam between the supports, but a lower overall material volume compared to the topology optimized beams. Taking the average flexural strength value of the prismatic beams, it can be calculated that the increased flexural strength due to the topology optimization is about 25%.

The effect of the 3D printing on the peak flexural strength is that the 3D printed topology beams have an 11% higher peak flexural stress than the casted topology optimized beam, this effect is due to the fiber alignment that takes places during the extrusion of the HS-DC material through a narrow nozzle that aligns the fibers along the printing path, increasing the material strength parallel to that direction as the fiber amount is theoretically increased in that direction. In the perpendicular direction, the fibers would be aligned in an unfavorable direction decreasing the overall bridging capacity of the fibers and decreasing the strength performance in the perpendicular directions. In this test, the longitudinally fiber alignment is favorable to the loading and supports setup as the fiber alignment direction is parallel to the span of the beam.

From the average displacement capacity results there is no significant difference between the performance of the casted topology optimized beam at 4.4 mm, the prismatic total volume 4.5 mm and the prismatic effective volume 4.3 mm. Moreover, the displacement capacity for the casted topology optimized beam falls in between the two prismatic beams which represent the upper and lower bound in terms of comparable beam geometry indicating that the topology optimization geometry, in this case for the clamped 4-point bending test, does not affect the ductility. This could contradict the results from the standard 4-point bending test which in that case showed a better performance in ductility for the topology optimized beam because these have a thinner cross section, but in this case the clamped 4-point bending test setup increases the compressive stresses which changes the failure mode to one in which the compressive strength have a bigger impact, so the topology optimized beam is being disfavored for having a thinner cross section that as a consequence provides a lower ductility in this clamped test setup that increases the compressive stresses compared to the tensile governed failure mode of the previous standard 4-point bending test.

On the contrary, the 3D printing process does have a significant increase in displacement capacity, at 5mm for the 3D printed topology to the 4.4 mm displacement of the Casted topology beam there is a 14% increase in performance due to the fiber alignment along the span of the beam.

The stiffness is not compared as in the clamped 4-point bending test the elastic regions have a large variation between the different types of specimens in which some did not even have a linear elastic region.

Two additional control specimen types are added in the Figure 115, the no fibers clamped topology beam (brown curve) and no fibers prismatic effective volume beam (purple curve). Which are beams produced using only the HS-DC cementitious matrix without the fibers, which is then a material similar to conventional high strength concrete. This shows the great impact of the fibers that without them the strength and ductility is severely reduced by a factor of 10.

The following chart (Figure 116) shows the average relative performance impact of the topology optimization and 3D printing process in the beam for the standard and clamped 4-point bending test. It is based on the performance results of the properties flexural strength, displacement capacity at rollers and stiffness summarized from the previous chapter about the experimental results.

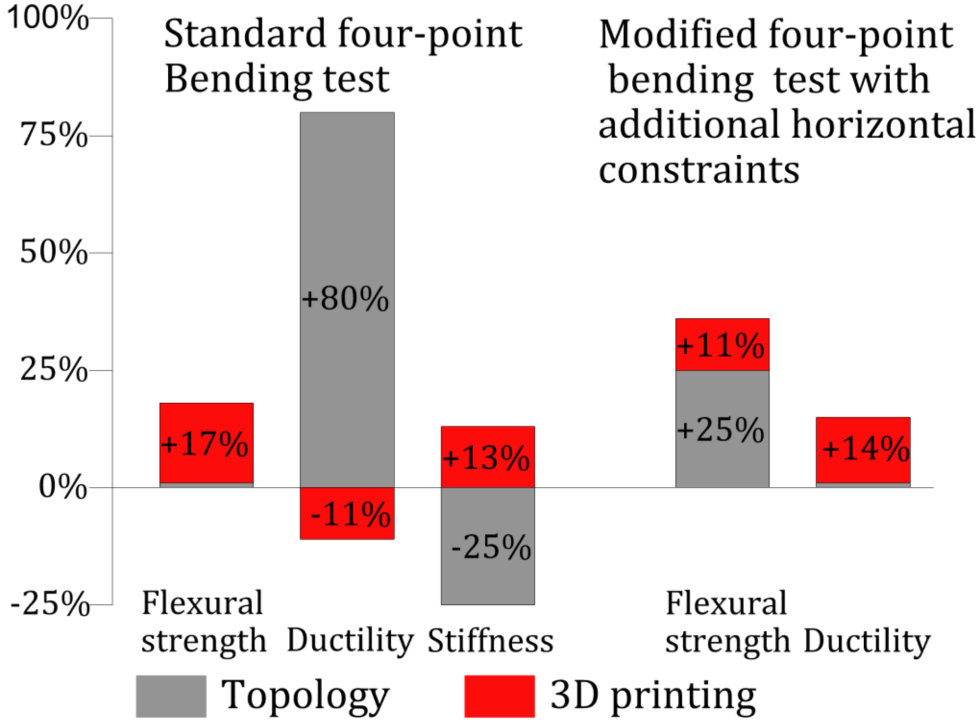

Figure 116: Effect of topology optimization and 3D printing on the percentage differences in flexural strength, ductility (displacement capacity) and initial stiffness of beams made of high-strength ductile concrete

Each bar represents the average relative performance of a beam, with the topology optimization represented in grey and the 3D printing process in red. For instance, for the standard 4-point bending test the displacement capacity is increased by 80% if the beam has the topology optimized design, and it is decreased by -11% if the beam is 3D printed. Looking at the clamped 4-point bending test side the flexural stress is increased by +25% if the beam is topology optimized and it is also increased on average by +11% if it is also 3D printed.

CHAPTER 4: Finite Element Based Modeling of High-Strength Ductile Concrete Beam Behavior

4.1. FEM Model

A Finite Element Method model was created with the software Abaqus to simulate the standard and clamped 4-point bending tests for every type of beam specimen. With the objective to model in the most accurate possible way the behavior of the High Strength Ductile Concrete beams, whether 3D printed or casted and with the topology optimized geometry.

Being able to precisely simulate 3D printed HS-DC objects is mandatory in order to design any structure using this new technology, and doing so with a good enough tolerance to ensure a safe and reliable design.

First, the test setup and beams were modeled in a CAD software and imported into the Abaqus program and assembled into its position like in the real test.

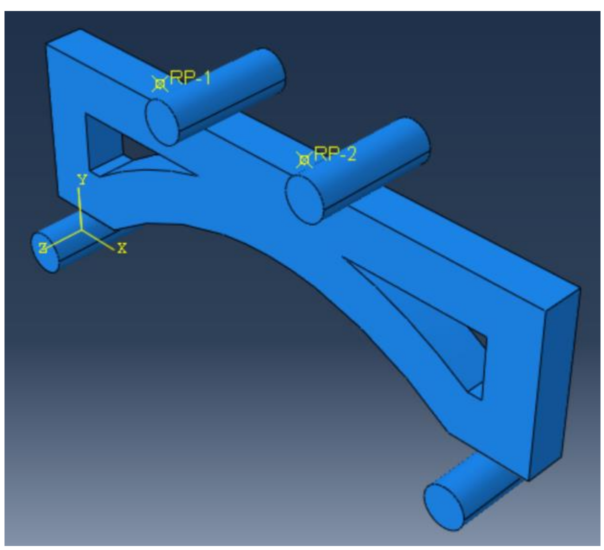

Figure 117: Finite element model of topology-optimized high-strength ductile concrete beam under four-point bending

The material properties were applied to each element. The steel in the rollers and clamp was modeled as a material with an elastic behavior given a Young's Modulus of 200 GPa, density 7800kg/m^3 and Poisson's ratio of 0.32.

The High strength Ductile Concrete material was simulated using a Concrete damaged plasticity model in which the material constitutivep relation and parameters were obtained from real testing of the HS-DC material. The compressive behavior was obtained from a uniaxial compression test of a cylindrical specimen and the Concrete tension damage behavior was also experimentally obtained from the Stress-Strain relation from a uniaxial tension test.

The model requires the Young's modulus of 45.1 GPa obtained from the initial linear stress-strain relation of the previous tests, density 2400 Kg/m^3, Poisson ratio 0.18, dilation angle 30, eccentricity 0.1, fb0/fc0 = 1.16, k = 0.667 and viscosity 0.00005.

The strain hardening stage can be input from the graph of the stress-strain relation removing the elastic region which is already considered with the Young's modulus. To model the concrete damage which represents the collapse of the beam and the decrease in strength after the peak, it is derived from an equation for the Simplified model of the Damage plasticity. It considers that the compressive and tensile damage in based on the inelastic hardening strain that controls the unloading curve slope [47]. So the slope of the unloading stage is considered the damage (d) and is calculated with the equation:

$$d = 1 - \frac{\sigma}{\sigma_u} \tag{3}$$

The boundary conditions were set on the rollers and the clamp, with a fixed boundary condition on the lower rollers and the upper rollers with a vertical displacement of 10 mm constrained to reference points RP-1, RP-2 and fixed on the horizontal directions.

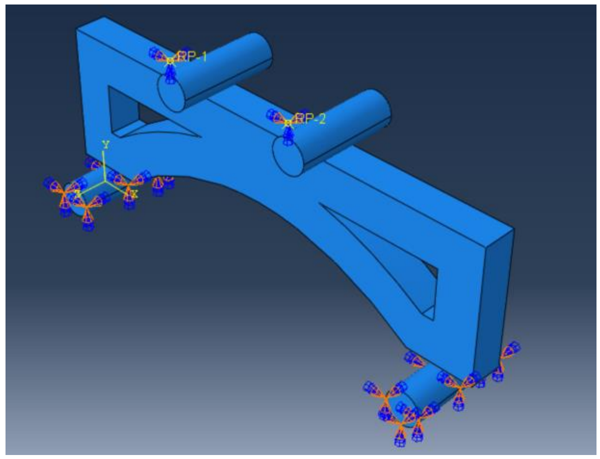

Figure 118: FEM model boundary conditions

A contact property was set between the steel rollers and the HS-DC beam with a tangential behavior with a Friction coefficient of 0.1, and a normal behavior with a hard contact pressure-overclosure.

The displacement of the upper rollers was subordinated to two points called RP-1 and RP-2 in which the boundary condition displacement is applied. The two points are constrained to the upper rollers and all move at the same rate and time. This constrain was set to easily obtain the output of the total force for every displacement. By comparison, obtaining the total reaction forces directly from the roller elements would require the integration of the local forces of each mesh polygonal element that forms the roller, which could decrease the precision of the analysis.

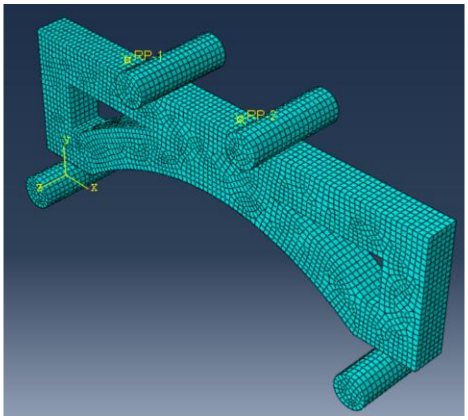

Figure 119: FEM model of the topology optimized beam under four-point bending with Hex mesh applied

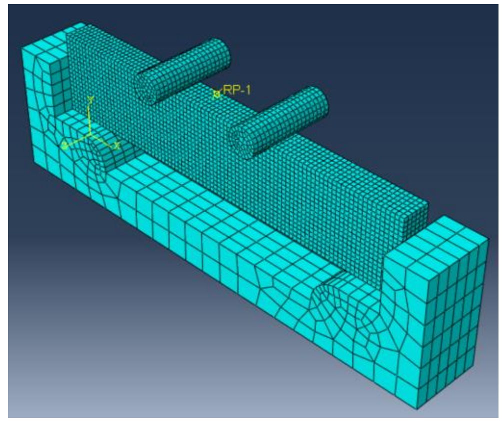

Figure 120: FEM model of the prismatic beam under modified four-point bending with Hex mesh applied

The parts were meshed in a finite element Hex mesh as shown in Figure 119, trying to minimize the amount of elements for computation economy, while maintaining a good geometric fidelity and enabling calculation convergency.

The output parameters were selected to be the vertical displacement U2 to know the vertical displacement on every point and time and the Reaction force RF to know the force applied on the reference points RP-1 and RP-2.

Finally, the complete model was run and after a calculation period all the results from of the standard and clamped 4-point bending test for all beam specimens types were obtained and presented in the next chapter 5.

4.2. Numerical simulation results – 3D printed high-strength ductile concrete beam with topology optimization

The 3D printed topology beam under the standard 4-point bending test was simulated using the FEM Abaqus model described in the previous chapter. From the simulation the flexural stress -displacement relation for the test was obtained (Figure 121) and the Major strain field of the front face of the beam (Figure 122). Also using the same scale and color representation as in the real Digital Image Correlation strain field (Figure 123) obtained at the experimental part.

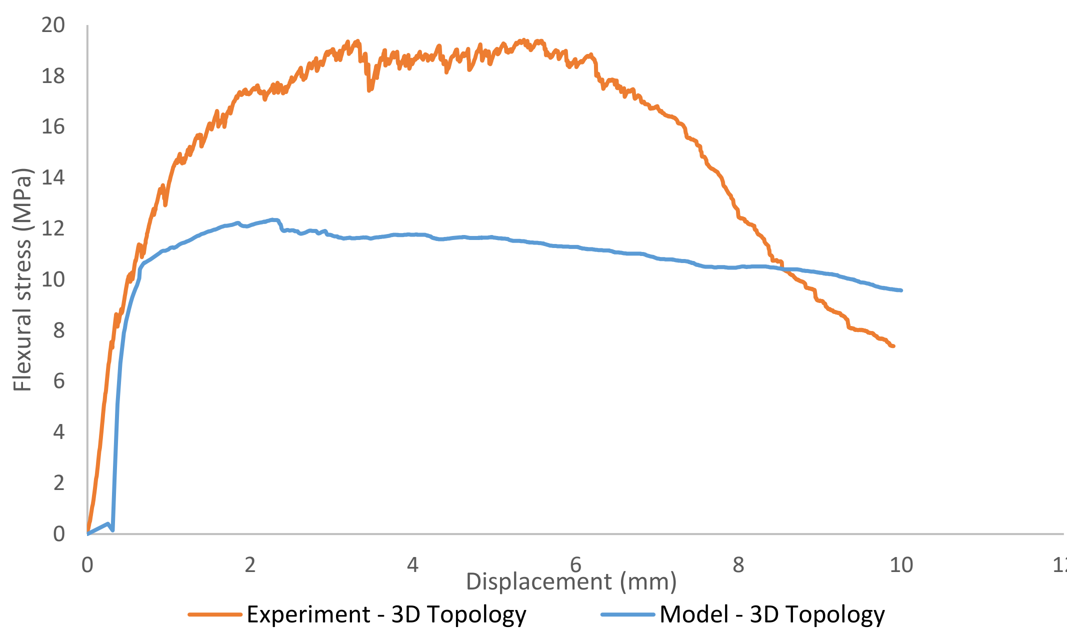

Figure 121: Comparison between modeling and experimental results for 3D printed topology-optimized beam

From the flexural stress -displacement relation (Figure 121) comparing the FEM model (blue curve) to the real 3D printed topology beam (orange curve) for the standard 4-point bending test, It can be seen that both have an elasto-plastic behavior. With an initial linear elastic behavior which in the case of the FEM model has a higher slope, also in the strain-hardening phase. In this plastic stage the FEM model shows a lower flexural strength. Moreover, the real 3D printed beam has a saw-toothed pattern indicating the formation of microcracks in each drop in flexural stress, which in the case of the FEM modeled beam has a smoother curve and doesn't reflect this behavior as much. However, for the general performance of the beam the small sudden drops in strength from the propagation of microcracks in the real 3D printed beam do not have a significant effect as these drops are small relative to the overall flexural stress.

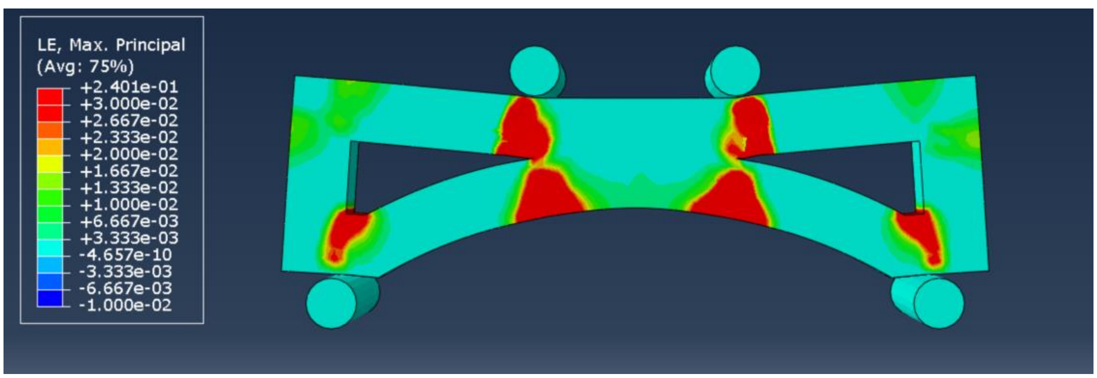

Figure 122: FEM model predicted major strain field in the 3D printed topology-optimized beam

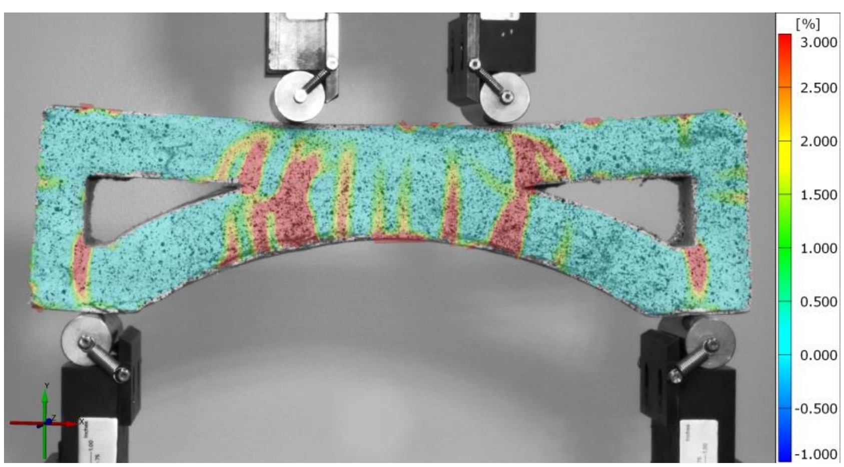

Figure 123: Experimentally measured major strain field in the 3D printed topology-optimized beam

The Figure 122 shows the Major strain field of the FEM modeled 3D printed topology beam at the same displacement as in the real major strain field from Figure 123. It is represented in the moment the critical crack starts propagating and causing the collapse of the beam. The areas shaded in red in both major strain field figures represent a tensile strain over 3%, in light blue 0% strain and in dark blue negative or compressive strain. It can be seen that the areas shown in red from the FEM Abaqus model correlates to the areas where there is an agglomeration of microcracks in the real beam as these microcracks causes most of the tensile strain and ductility. These high strain areas concentrate on the lower side of the arch right below the upper rollers and in the vertices of the triangular shaped holes of the topology optimized geometry.

Overall, there is a good correlation between the Abaqus model and the real beam strain field, and the deformed shape that bends toward the center also correlates to the real test.

From the flexural stress -displacement relation (Figure 121) the overall elasto-plastic behavior is also well simulated but the slope of the elastic stage is higher and the maximum flexural strength is lower in the case of the Abaqus model.

4.3. Numerical simulation results – Casted high-strength ductile concrete beam with topology optimization

The Figure 124 shows the flexural stress -displacement relation of both the FEM Abaqus model and real standard 4-point bending test of the Casted topology beam. Both curves show an initial linear relation and after a yielding point, a strain hardening stage similar to the previous 3D printed topology case but with a slightly lower peak flexural strength. Because in the case of the 3D printed topology beam the material properties in Abaqus was adjusted to 3D printed HS-DC behavior which in this case improves its performance due to fiber alignment. On the contrary, the casted topology beam is modeled after an isotropic HS-DC where the fibers are homogeneously distributed, decreasing the flexural strength compared to the 3D printed one.

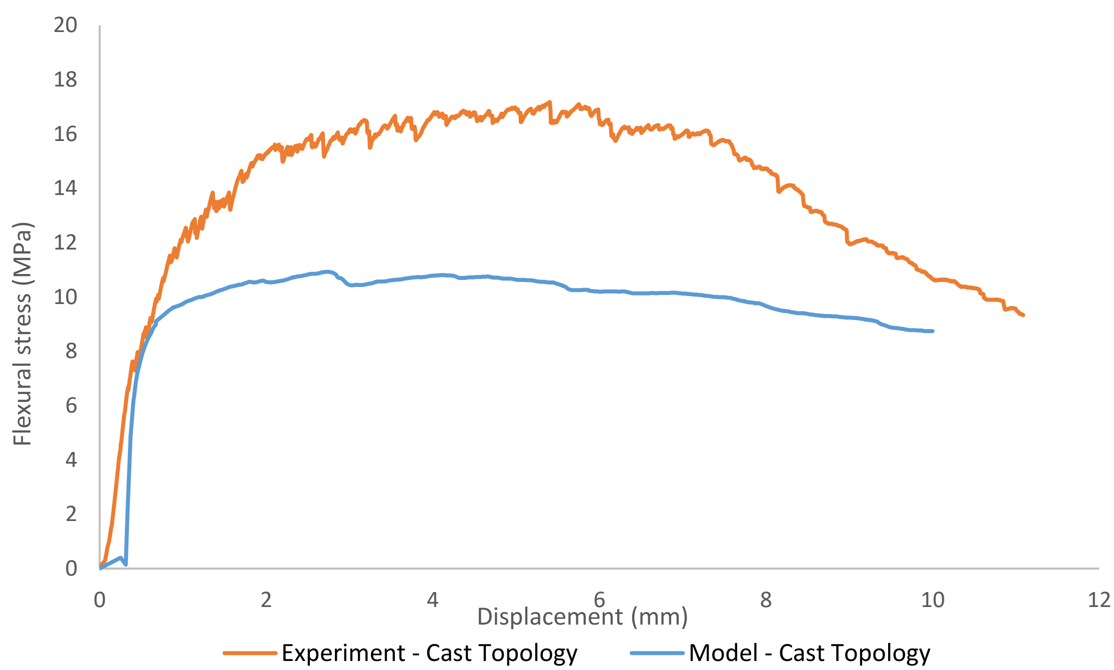

Figure 124: Comparison between modeling and experimental results for casted topology-optimized beam

The major strain field of the FEM model and real casted topology beam is represented in Figure 125 and Figure 126 for a given displacement after the critical cracks have been formed and the beam is collapsing. In the real specimen the critical cracks are located inside the red colored areas indicating the largest strain and damage. These high strain areas are accurately simulated in the FEM modeled beam. Although this model is not able to represent the microcracks, the overall collapse mode and deformed geometry is realistic.

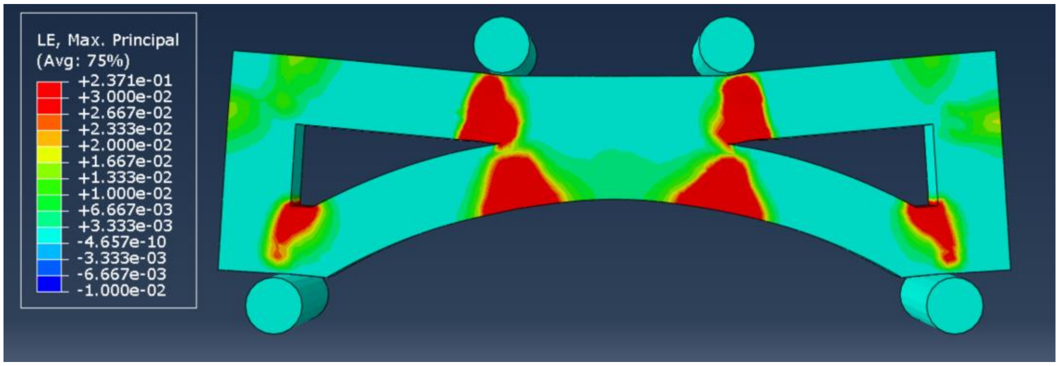

Figure 125: FEM model predicted major strain field in the casted topology-optimized beam

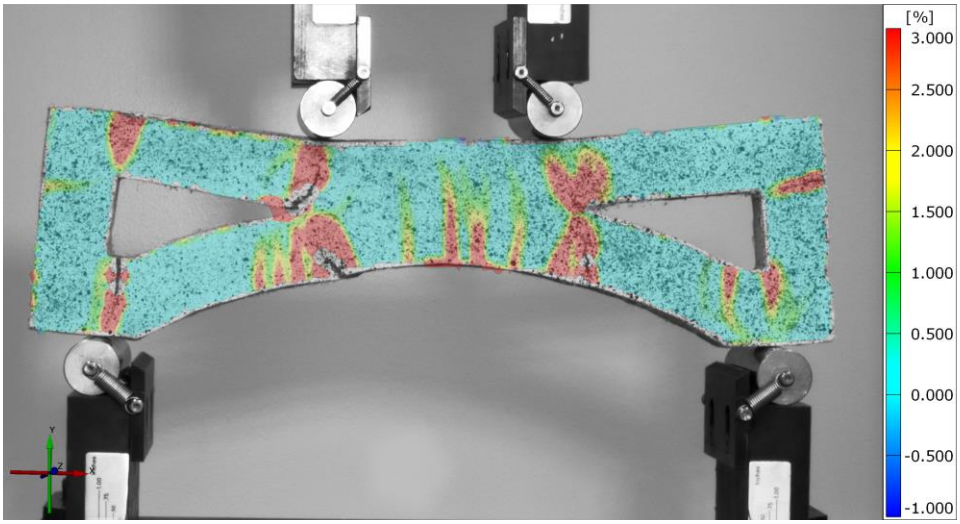

Figure 126: Experimentally measured major strain field in the casted topology-optimized beam

4.4. Numerical simulation results – Casted prismatic high-strength ductile concrete beam with the same total volume

The flexural stress -displacement relation for the prismatic same total volume beam in the FEM model and in real 4-point bending test is represented in the (Figure 127). In this case the behavior is also elasto-plastic but the initial linear elastic slope of the FEM model fits better the real test than the previous topology optimized beams.

The strain hardening phase for this kind of beam shows a lower ductility which is also reflected in the FEM result in which it reaches a flexural strength at around 2.5 mm and then it begins to collapse like in the real specimen, although a bit earlier and with a lower flexural stress as in previous beam types.

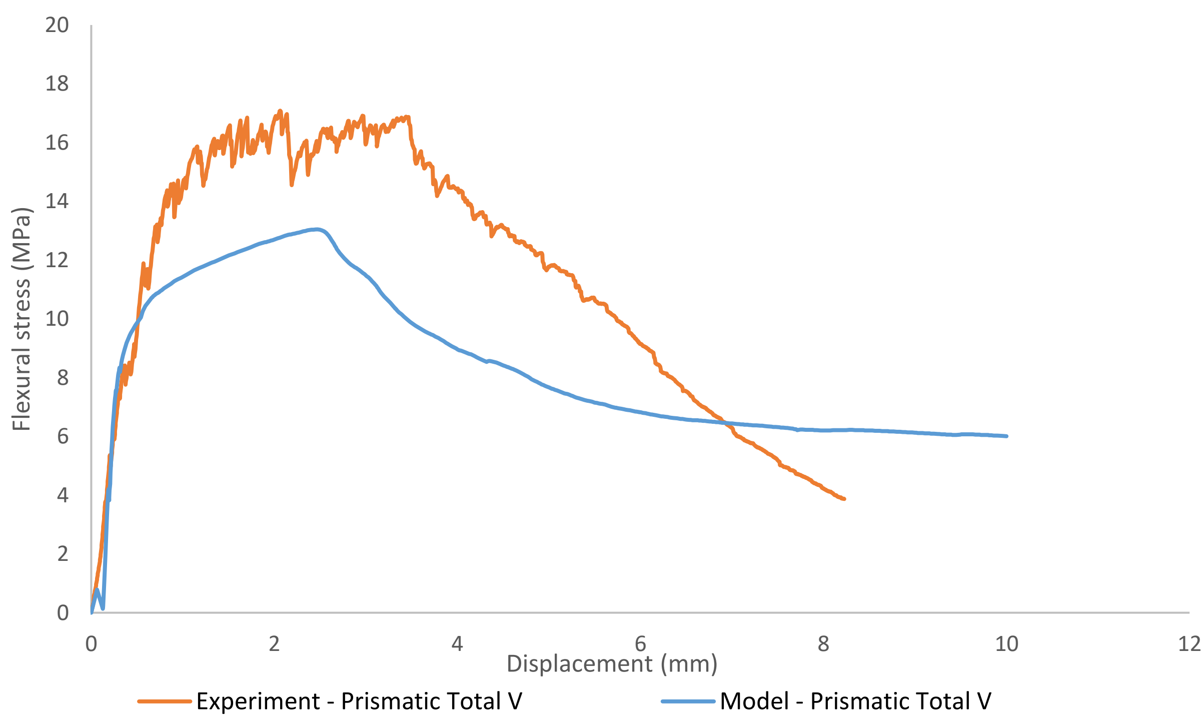

Figure 127: Comparison between modeling and experimental results for casted prismatic beam with the same total volume as topology-optimized beam

The major strain field of the FEM prismatic total volume beam (Figure 128) indicates the areas with most damage and strain are located on the lower middle section of the beam specially below the upper rollers. For the real beam (Figure 129) the location of the highest strain areas are also in the middle lower section, but in this case the strain is more dispersed in several small microcracks along the middle span, although there is an increase in microcracks concentration below the upper rollers, similar to the the FEM model. This indicates that although the FEM Abaqus model using the Concrete Damage plasticity model cannot represent microcracks, it does approximate well the location of the strain and the overall deformation of the beam.

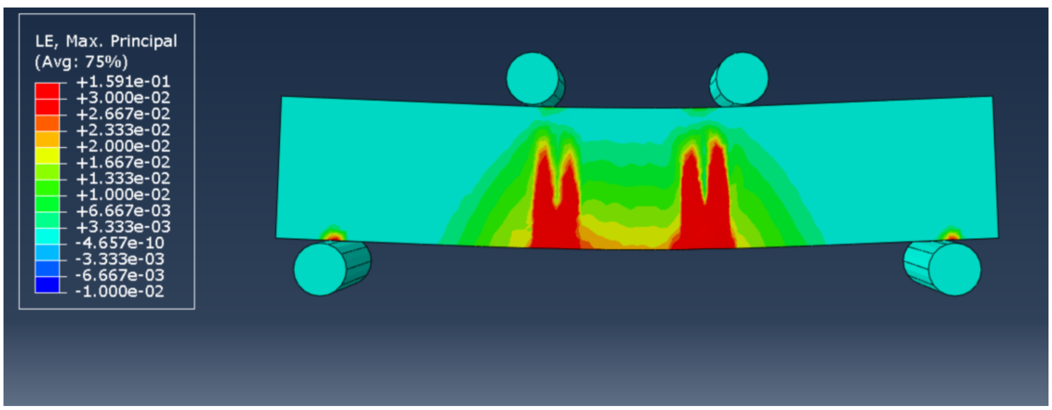

Figure 128: FEM model predicted major strain field in the casted prismatic beam (same total volume as the topology-optimized beam)

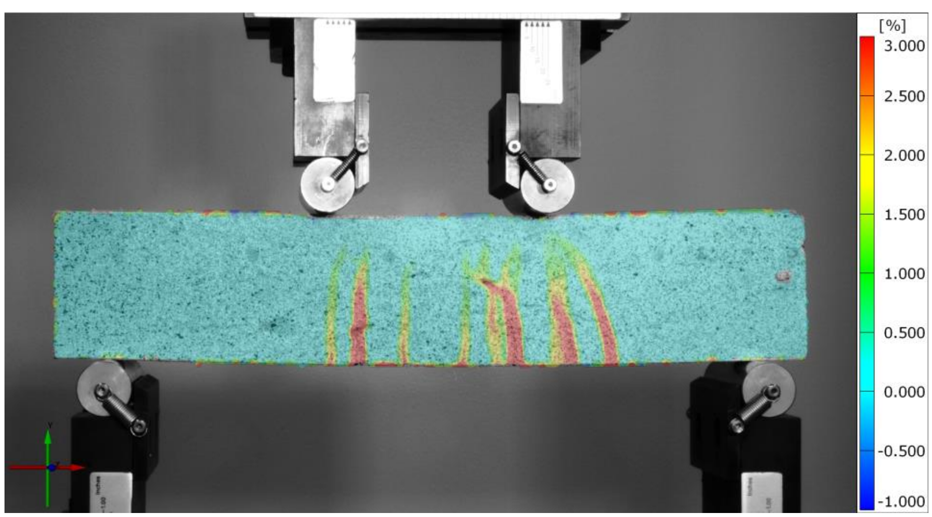

Figure 129: Experimentally measured major strain field in the casted topology-optimized beam (same total volume as the topology-optimized beam)

4.5. Numerical simulation results – Casted prismatic high-strength ductile concrete beam with the same effective volume

The prismatic effective volume beam modeled with FEM also follows the behavior of the real specimen as shown in the flexural stress -displacement relation from the standard 4-point bending test represented in Figure 130. The most significant difference is that the FEM model beam curve (blue curve) has a higher yielding flexural stress but in the strain-hardening stage the slope of the FEM beam is lower and the trend of the strain hardening phase of the real specimen is steeper resulting in a higher flexural strength for the real specimen.

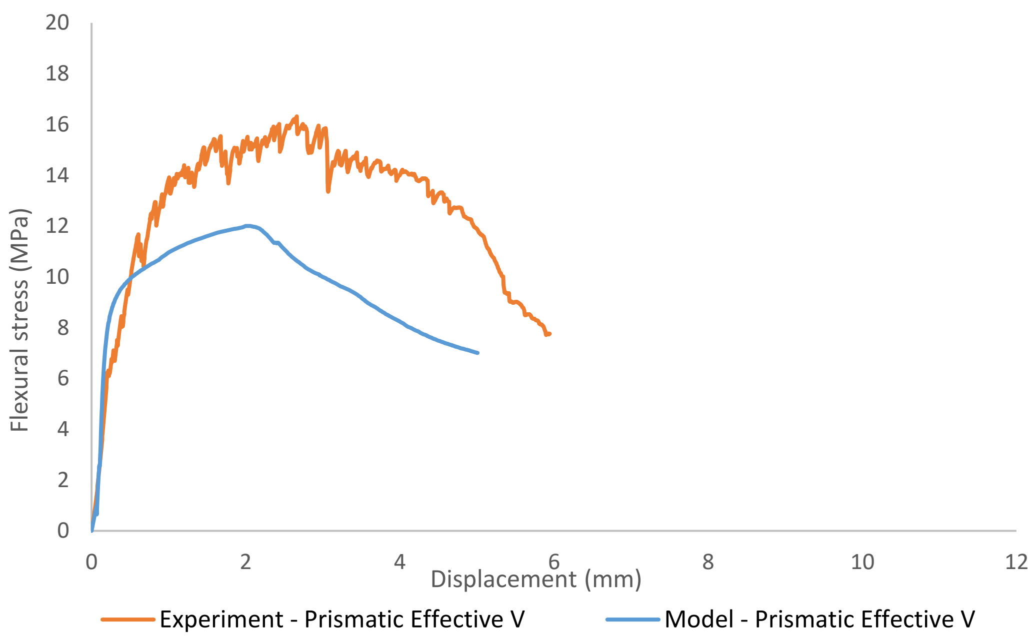

Figure 130: Comparison between modeling and experimental results for casted prismatic beam with the same effective volume as topology-optimized beam

The major strain field of both the real (Figure 132) and FEM beam (Figure 131) have the shaded areas in red and green in similar locations. With the FEM model strain field indicating a broader area of high strain around the middle span of the beam and in the real specimen located inside the same areas but in thinner stripes, which are formed by microcracks. The microcracks located more on the sides of the real beam are bent towards the upper rollers, and for the FEM model the border of the green shaded area is also curved in a similar way. Indicating the FEM model simulates the same phenomenon but with a shaded high strain area instead of more concentrated real microcracks, with this curvature being caused by shear stresses.

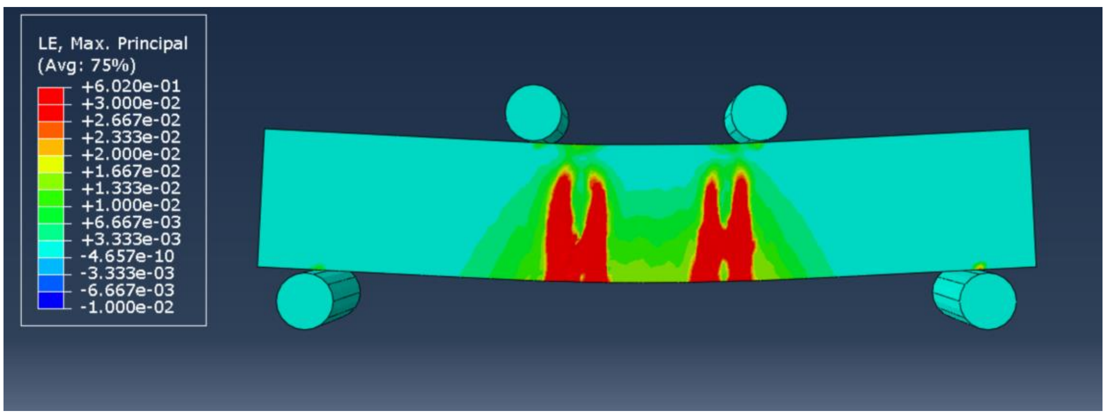

Figure 131: FEM model predicted major strain field in the casted prismatic beam (same effective volume as the topology-optimized beam)

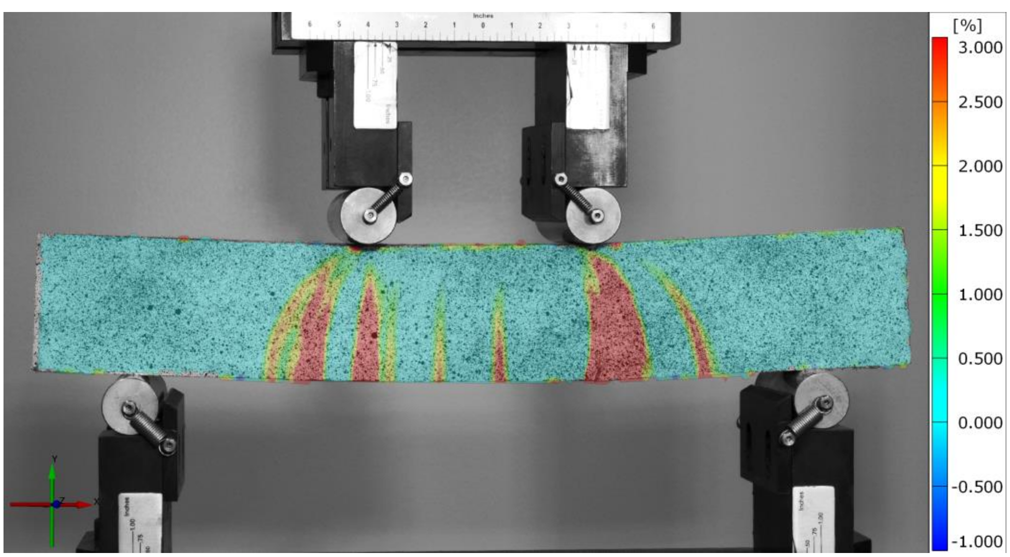

Figure 132: Experimentally measured major strain field in the casted prismatic beam (same total volume as the topology-optimized beam)

4.6. Numerical simulation results – 3D printed high-strength ductile concrete beam with optimized topology (with additional horizontal constraints at supports)

The FEM Abaqus model of the 3D printed topology beam was also implemented with the Clamped 4-point bending setup, modelling the steel clamp with the same geometry as the real one with steel material properties. From the flexural stress -displacement relation of the Clamped 4-point bending test in Figure 133 it can be seen that the FEM modelled 3D printed topology beam has an initial linear increase of the flexural stress with a very steep slope compared to the real test which has a smaller derivative on this initial phase. However, both reaches a similar flexural strength but at a very different displacement. In this case the displacement capacity of the FEM model is much smaller. After the flexural stress reaches its peak strength both curves have a steep reduction of the flexural stress with an almost vertical slope, indicating that the collapse of the beam in a similar way for both the FEM model and real specimen and with a rapid energy release for a brittle collapse mode.

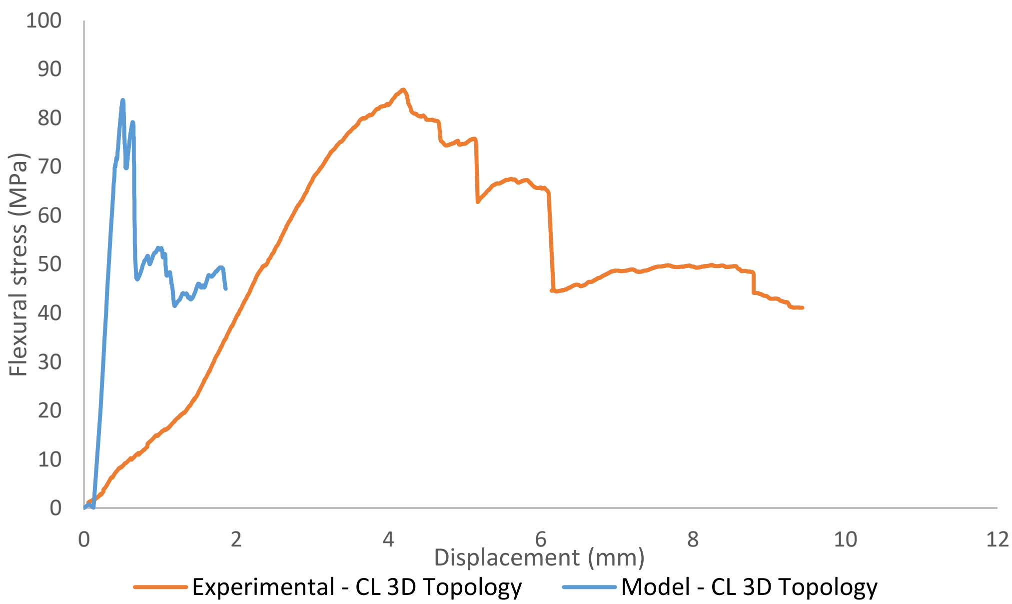

Figure 133: Comparison between modeling and experimental results for 3D printed topology-modified beam with additional horizontal constraints at supports

The major strain field for both FEM model and real clamped 3D printed topology beam is represented in Figure 134 and Figure 135 respectively. The areas with a high strain are shaded in red which in the case of the FEM model it occupies all the regions between the upper rollers to the lower support of the beam running along the arch, and two more red areas on the side of the beam where the clamp ends vertically.

The regions shaded in red in the real beam correlates to the amount of microcracks and are all contained inside the red shaded areas of the FEM beam. The overall deformation of the beam is very similar for both real and FEM model indicating it is also modelling this clamped 4-point bending setup reasonably well, although for the real beam on side of it is more damaged than the other and for the FEM beam it has a symmetric result, which could be important to take into consideration.

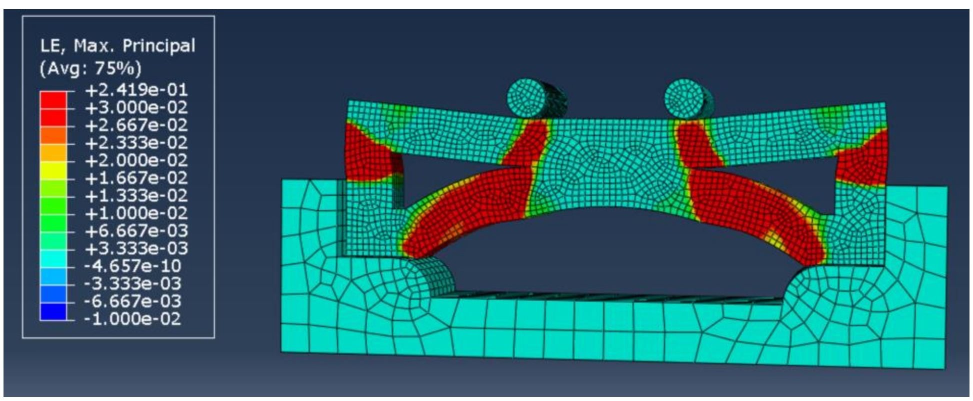

Figure 134: FEM model predicted major strain field in the 3D printed topology-optimized beam with additional horizontal constraints at supports

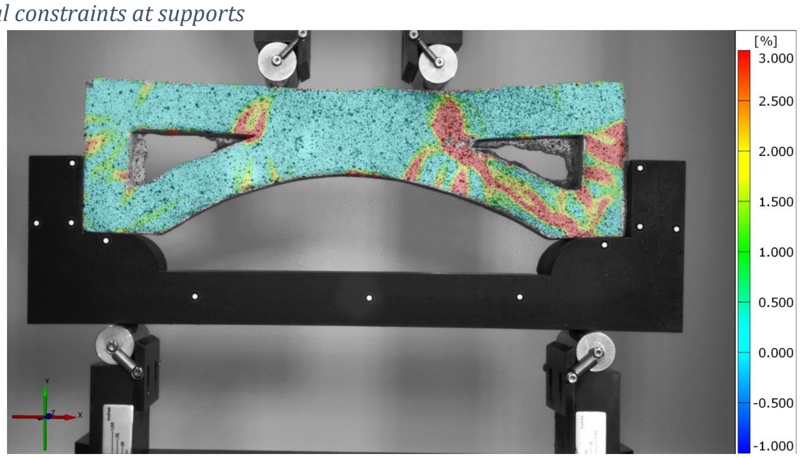

Figure 135: Experimentally measured major strain field in the 3D printed topology-optimized beam with additional horizontal constraints at supports

4.7. Numerical simulation results – casted high-strength ductile concrete beam with optimized topology (with additional horizontal constraints at supports)

The flexural stress -displacement relation of the FEM casted topology beam with the clamped 4-point bending test setup compared to the real specimen have the same differences as in the previously studied 3D printed topology beam. It shows a very high initial slope compared to the real test, but the flexural strength value is well approximated. However, the peak is produced at a much smaller displacement and having a much lower displacement capacity than the real beam.

The collapse mode of the beam is well simulated with both FEM model and real beam curves having a vertical fall of the flexural stress to a similar value plateau, which then continues constant for very large displacements, as the steel clamp is still compressing the cracked beam and providing a residual strength.

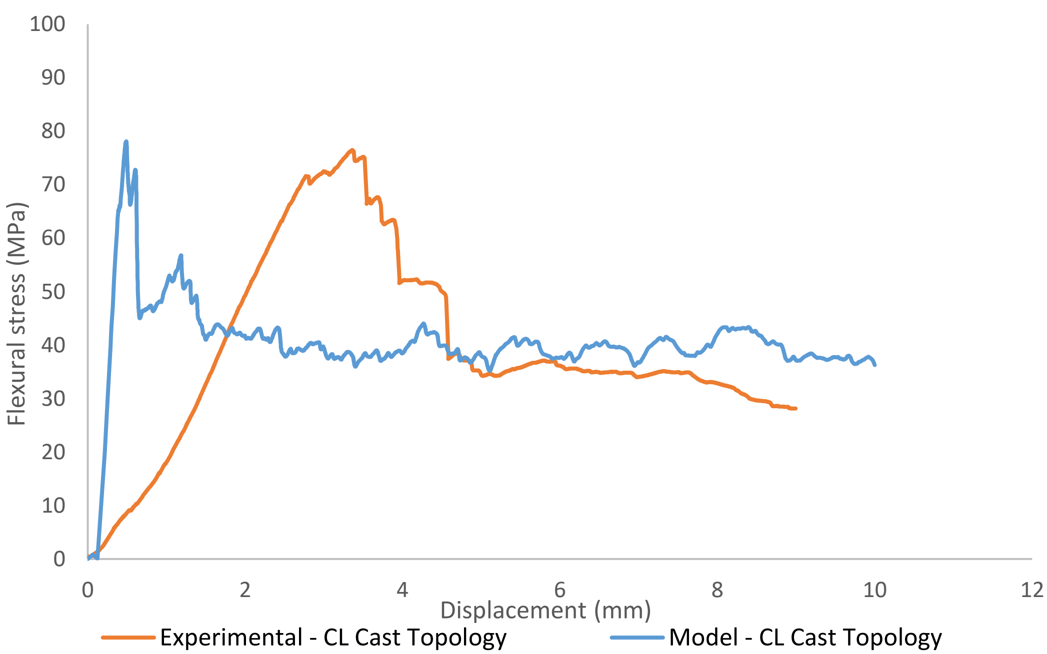

Figure 136: Comparison between modeling and experimental results for casted topology-optimized beam with additional horizontal constraints at supports

The same conclusions can be observed from the major strain field of the FEM model casted topology beam (Figure 137) like with the 3D printed topology model, there is a broad red shaded area with a strain over 3%, which in the real specimen test these red shaded areas represent microcracks which are more concentrated in narrow red stripes along each microcrack. Nevertheless, all microcracks fit inside the red shaded area from the FEM model (Figure 138), indicating that the high strain areas are well modeled in the FEM beam.

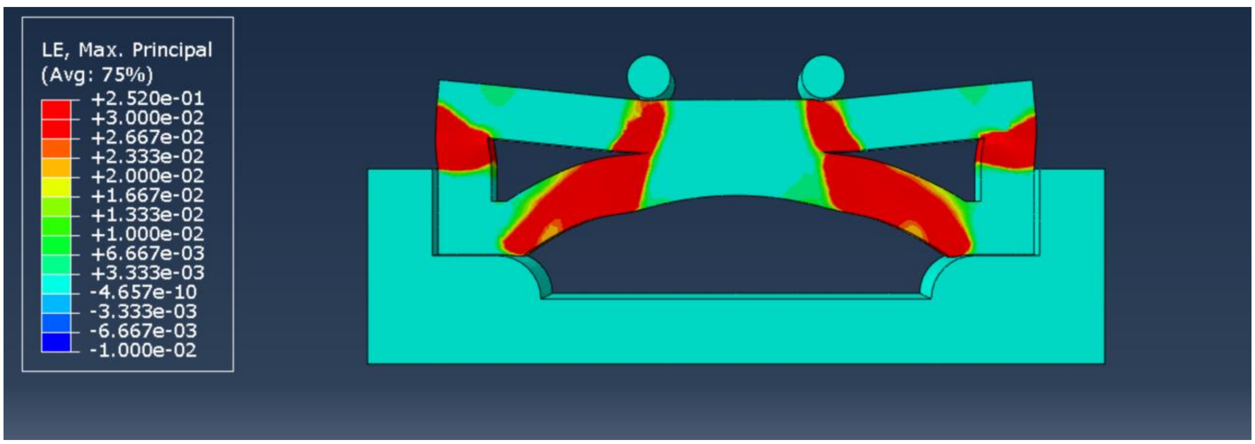

Figure 137: FEM model predicted major strain field in the casted topology-optimized beam with additional horizontal constraints at supports

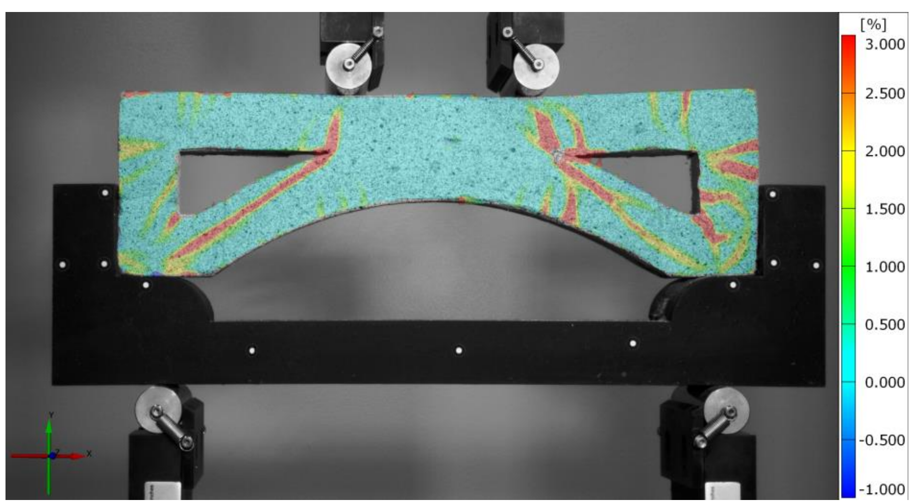

Figure 138: Experimentally measured major strain field in the casted topology-optimized beam with additional horizontal constraints at supports

4.8. Numerical simulation results – casted prismatic high-strength ductile concrete beam with the same total volume (with additional horizontal constraints at supports)

The flexural stress -displacement relation for the clamped 4-point bending test of the FEM model and real prismatic total volume beam is represented in the Figure 139. The orange curve represents the real specimen and the blue the FEM model. In this case there are important discrepancies in the behavior of these two curves. To begin with, the initial slope of the FEM model is steeper, and the peak flexural strength is much lower than the real beam. Moreover, the displacement capacity is also much smaller in the FEM simulated beam, which collapses with a brittle vertical decrease in flexural stress. On the contrary, the real prismatic same total volume beam has a continuous decrease in flexural stress with a constant smaller slope instead of a sudden brittle collapse.

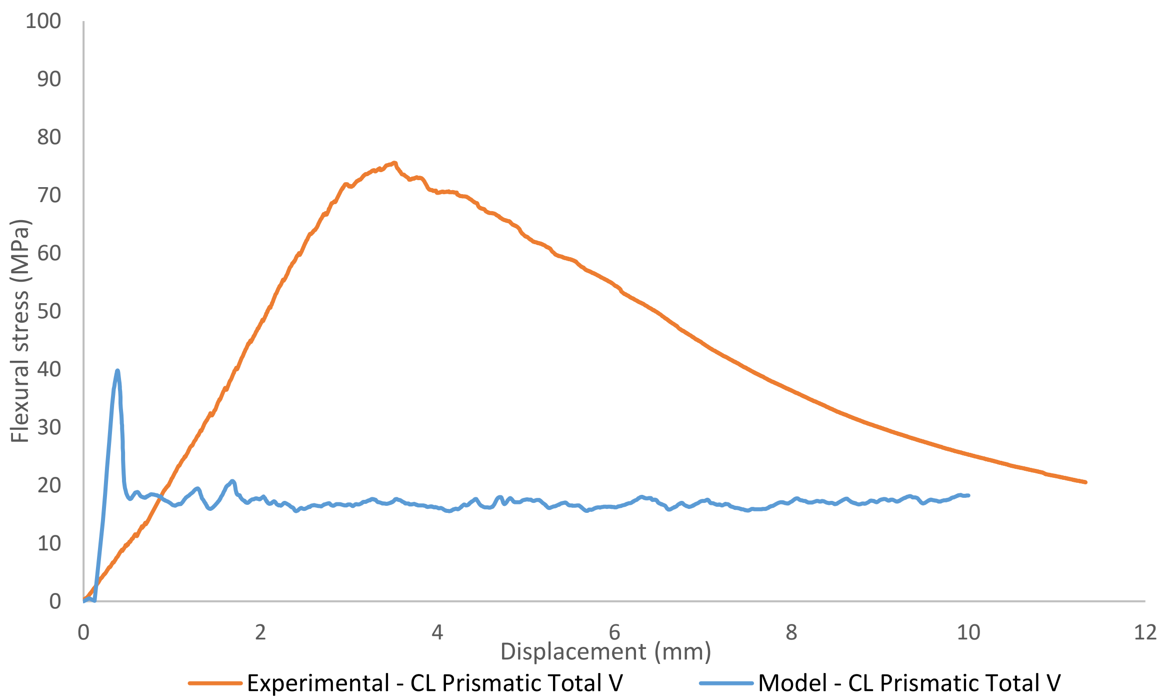

Figure 139: Comparison between modeling and experimental results for casted prismatic beam (same total volume) with additional horizontal constraints at supports

Examining the major strain field of the FEM model (Figure 140) the areas shaded with red, indicating a strain over 3%, are located in an inclined band running from the upper rollers to the lower clamp support of the beam. The inclination and location of the high strain area indicates that this mechanism is caused by shear stresses. Compared to the major strain field of the real specimen (Figure 141) it also shows two red stripes inclined towards the center of the upper rollers, that correlates to the region of high strain from the FEM model. However, in the real specimen there are also vertical microcracks shaded in red in the middle section of the beam which are caused by tensile stresses. These damaged regions caused by tensile stresses are not well simulated in the FEM model as these areas are not shaded in any color other than light blue which represents 0% strain and damage.

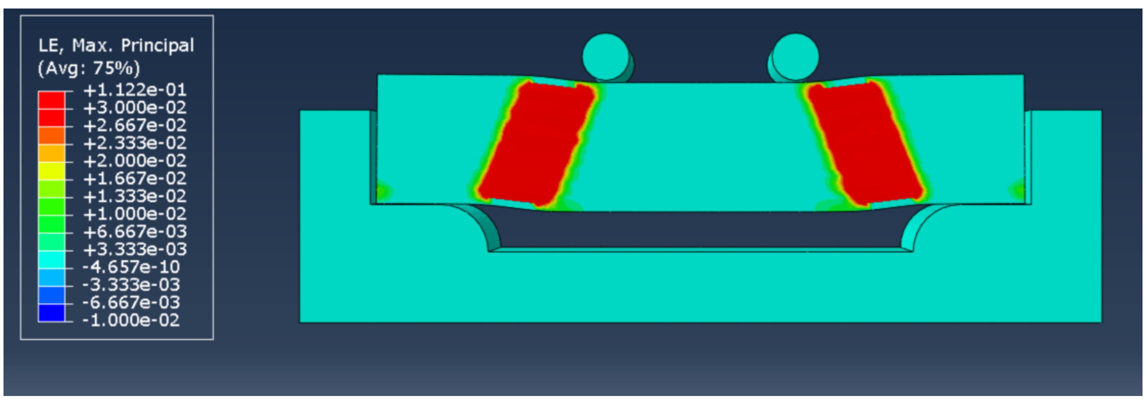

Figure 140: FEM model predicted major strain field in the casted prismatic beam (same total volume) with additional horizontal constraints at supports

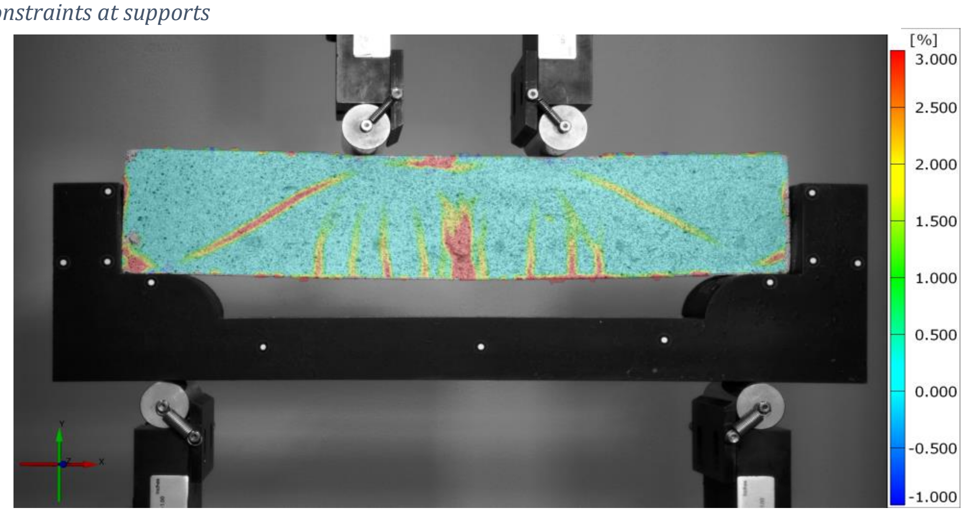

Figure 141: Experimentally measured major strain field in the casted prismatic beam (same total volume) with additional horizontal constraints at supports

4.9. Numerical simulation results – casted prismatic high-strength ductile concrete beam with the same effective volume (with additional horizontal constraints at supports)

The Figure 142 represents the flexural stress -displacement relation of the FEM model and real clamped prismatic effective volume beam. Similar to the previous clamped prismatic total volume FEM model, there are significant differences in the behavior of the both real and FEM beam. The initial linear slope is steeper and have a much lower displacement capacity at rollers for the later. However, in this case the flexural strength of the FEM model is in a similar order of magnitude as the real beam, and the collapse mode is also brittle for both with a vertical decrease in MOR.

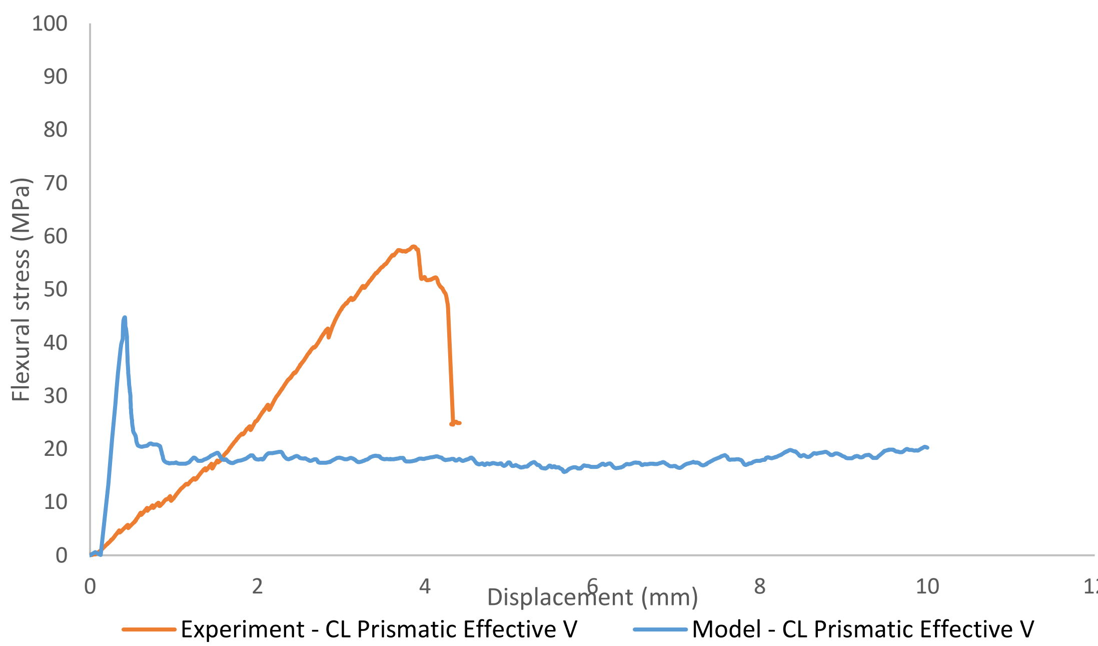

Figure 142: Comparison between modeling and experimental results for casted prismatic beam (same effective volume) with additional horizontal constraints at supports

The major strain field distribution of the FEM model clamped prismatic effective volume beam also has an inclined red shaded band that runs from the upper rollers to the clamp support like in the previously described prismatic total volume beam. Compared to the real specimen it also shows the inclined high strain areas that crosses the beam from the upper rollers to the clamp support, with these areas formed by thinner red shaded stripes that represent the microcracks and are mostly caused by shear stresses.

Nevertheless, there is a noticeable difference in which the real specimens have tensile microcracks in the middle section of the beam which are not shown in the FEM model. This indicates that the FEM model response in shear is weaker than in the real specimen and causes the FEM model beam to fail mostly in shear compared to the more diversified damage distribution of the real specimen, that contains shear damage and tensile strain areas in the middle section which are not present in the simulation.

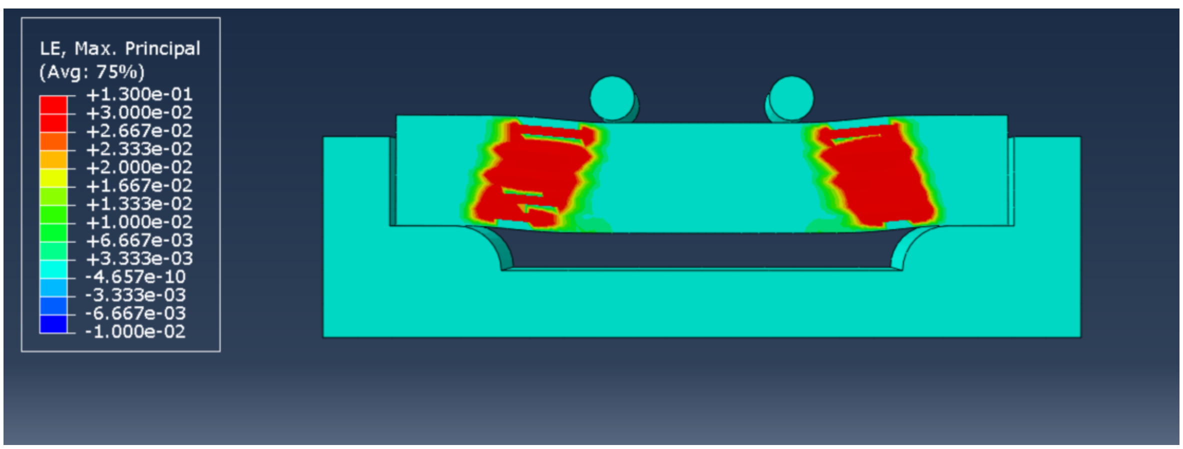

Figure 143: FEM model predicted major strain field in the casted prismatic beam (same effective volume) with additional horizontal constraints at supports

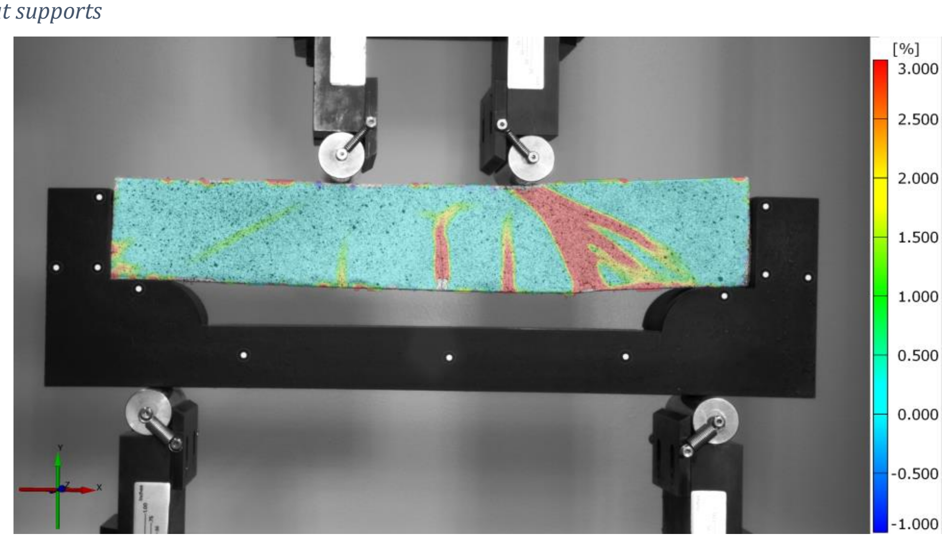

Figure 144: Experimentally measured major strain field in the casted prismatic beam (same effective volume) with additional horizontal constraints at supports

CHAPTER 6: Conclusions and Future Studies

3D concrete printing is an emerging technology that interfaces different disciplines in science and engineering, such as materials science and engineering, advanced manufacturing, robotics, topology, and mechanics. Understanding and harnessing the interconnections in these fields can lead to more rational and accelerated adoption of this technology to build structures and infrastructure with greatly improved mechanical performance but much reduced material uses and environmental impacts. The study presented in this thesis represents an initial step forward in such efforts, by integrating novel high-strength ductile concrete materials, 3D printing process and topology optimization to understand and to improve the mechanics of beam behavior.

This thesis work elucidated how concrete material ductility, 3D printing method, topology optimization, and beam boundary conditions affect the flexural behavior of concrete beams. The following conclusions can be drawn from this study:

- The novel high-strength ductile concrete transforms the concrete beam behavior from brittle and localized fracture to a displacement-hardening behavior with spatial formation of microcracking damage and a highly ductile failure mode. Without any steel reinforcements, the beams made of high-strength ductile concrete, whether casted or 3D printed, with or without topology optimization, were able to accommodate excessive bending force and extraordinarily large bending deformation and curvature before final failure happened.
- This study shows that high-strength ductile concrete with tailored rheology can be successfully 3D printed, into the optimized topology of the beam element. The 3D

printing process tends to align the polymeric fibers into the direction along the printing filament, leading to an increased resistance to stress and strain long the beam direction under bending, but less resistance in the direction perpendicular to the printing filaments. Therefore, the 3D printed beams with optimized topology exhibited higher flexural strength with similar large flexural ductility (which is the displacement capacity before failure) than the casted beams with optimized topology.

- The study shows topology optimization can significantly improve beam flexural behavior with the same usage amount of high-strength ductile concrete materials. The extent of improvement depends on the beam boundary conditions at the supports. When the supports are pin-roller without additional horizontal constraints along the beam direction, the beams with optimized topology exhibited higher load-carrying capacity (increased by 46%) as well as larger (more than twice) displacement capacity before failure, than the prismatic beams without topology optimization. The strain field evolution with increasing loading and displacement, captured by the digital image correlation system, revealed a sequential formation of a number microcracks within the tensile region of the beams, and the stress concentration areas cause by local geometry change (e.g., notches in the topology-optimized beams), leading to a spatially distributed damage process that significantly increased the overall flexural ductility and strength of the beams. The failure modes were flexure governed under this boundary condition.
- However, with additional horizontal constraints along the beam length, the beam failure modes under bending became shear- and compression-dominant, and the final failure was shear-governed, as seen in the measured damage pattern and strain field.

As a result, much less deflection-hardening behavior was observed in these shear-governed beams compared with their flexure-governed counterparts without horizontal constraints. Nonetheless, the high-strength ductile concrete provided much higher resistance to shear failure than conventional concrete, through developing distributed microcracking damage in the shear region. Furthermore, the additional horizontal constraints were favorable for taking advantage of the "arch-shape" geometry as part of the topology-optimized beam, subjecting the high-strength ductile concrete material mainly in compression along the "arch-shape" portion, rather than tension, thereby utilizing the ultra-high compressive strength of the concrete material. This unique mechanism enabled by the optimized topology, combined with the high shear resistance of the novel concrete material, led to extremely high flexural strength of the beam, in addition to maintaining a decent flexural deformation capacity before failure despite that the failure stage was less gradual or ductile as it was shear governed. Notably, the 3D printed beams with optimized topology achieved flexural strength up to almost 100 MPa when there were horizontal constraints at both supports, much increased from 20 MPa with a pin-roller support condition.

- In both scenarios of boundary conditions, the optimized topology in this study enabled by 3D printing significantly improved the beam flexural behavior, in terms of load carry capacity and flexural ductility, with the same amount of material usage.
- The finite element model well captured the stress and strain fields and the damage pattern in the beam specimens with different boundary conditions, with and without optimized topology, in agreement with the experimental results. Particularly, the

model well predicted the high strain-concentration areas within the beams where spatial microcracking damage was observed in the experiments.

- However, there is still significant discrepancy between the numerically predicted beam load vs. displacement relations and the experimental data. This calls for future studies to develop more accurate constitutive models of 3D printed high-strength ductile concrete materials, to reduce variation in the printed material properties, and to refine the finite element model parameters.

The research carried out from this thesis can be further pursued in multiple directions of future work. These include: (1) understanding how the 3D printing process, ranging from smaller- to larger-scales, would affect the rheological parameters and the resulting mechanics and properties of 3D printed structural elements made of high-strength ductile concrete; (2) developing more accurate constitutive models of 3D printed concrete or 3D printed high-strength ductile concrete, including monotonic and cyclic models, to integrate into the finite element modeling framework to better predict their structural behavior and to guide structural designs; (3) performing more refined topology optimization and complex geometries enabled by 3D printing for structural elements subjected to various loading conditions to achieve greatly improved structural capacity, damage resistance, ductility and energy-dissipation capacity; (4) scaling up the beam designed with optimized topology and validating the 3D printing process and the resulting structural behavior at larger scale; (5) exploring bio-inspired designs and manufacturing of structural members, enabled by the novel concrete materials and 3D printing process, to achieve unprecedented structural behavior and capacities resisting normal and extreme loading conditions.

REFERENCES

[1] J. Xiao *et al.*, "Large-scale 3D printing concrete technology: Current status and future opportunities," *Cem. Concr. Compos.*, vol. 122, p. 104115, Sep. 2021.

[2] G. W. Ma, L. Wang, and Y. Ju, "State-of-the-art of 3D printing technology of cementitious material—An emerging technique for construction," *Science China Technological Sciences*, vol. 61, no. 4. Springer Verlag, pp. 475–495, 01-Apr-2018.

[3] C. Beyer, "Strategic Implications of Current Trends in Additive Manufacturing," *J. Manuf. Sci. Eng. Trans. ASME*, vol. 136, no. 6, Dec. 2014.

[4] I. Perkins and M. Skitmore, "Three-dimensional printing in the construction industry: A review," *Int. J. Constr. Manag.*, vol. 15, no. 1, pp. 1–9, Jan. 2015.

[5] H. Al Jassmi, F. Al Najjar, and A.-H. I. Mourad, "Large-Scale 3D Printing: The Way Forward."

[6] B. Nematollahi, M. Xia, J. G. Sanjayan, and J. Sanjayan, "Current Progress of 3D Concrete Printing Technologies Fiber-Reinforced Strain-Hardening Geopolymer Composites (SHGC) View project CRC-LCL Project View project Current Progress of 3D Concrete Printing Technologies," p. 260, 2017.

[7] F. Bos, R. Wolfs, Z. Ahmed, and T. Salet, "Additive manufacturing of concrete in construction: potentials and challenges of 3D concrete printing," *Virtual Phys. Prototyp.*, vol. 11, no. 3, pp. 209–225, Jul. 2016.

[8] W. Oropallo and L. A. Piegl, "Ten challenges in 3D printing," *Eng. Comput.*, vol. 32, no. 1, pp. 135–148, Jan. 2016.

[9] R. Duballet, O. Baverel, and J. Dirrenberger, "Classification of building systems for concrete 3D printing," *Autom. Constr.*, vol. 83, pp. 247–258, Nov. 2017.

[10] R. A. Buswell, W. R. Leal de Silva, S. Z. Jones, and J. Dirrenberger, "3D printing using concrete extrusion: A roadmap for research," *Cem. Concr. Res.*, vol. 112, pp. 37–49, Oct. 2018.

[11] Y. Ma and S. Winsun, "A brief introduction to 3D printing technology."

[12] N. Gaudillière *et al.*, "Large-Scale Additive Manufacturing of Ultra-High-Performance Concrete of Integrated Formwork for Truss-Shaped Pillars," *Robot. Fabr. Archit. Art Des. 2018*, pp. 459–472, Sep. 2018.

[13] G. De Schutter, K. Lesage, V. Mechtcherine, V. N. Nerella, G. Habert, and I. Agusti-Juan, "Vision of 3D printing with concrete — Technical, economic and environmental potentials," *Cem. Concr. Res.*, vol. 112, pp. 25–36, Oct. 2018.

[14] N. Gaudillière *et al.*, "Building Applications Using Lost Formworks Obtained Through Large-Scale Additive Manufacturing of Ultra-High-Performance Concrete," *3D Concr. Print. Technol.*, pp. 37–58, Jan. 2019.

[15] P. E. Gennadievna, M. P. Vladislavovich, M. E. Sergeevna, Y. V. Alexandrovich, I. I. Aleksandrovich, and D. B. Azaoui, "House-building analysis when using additive technologies: Classification, advantages and disadvantages," *J. Appl. Eng. Sci.*, vol. 17, no. 4, pp. 449–456, 2019.

[16] F. P. Bos, Z. Y. Ahmed, E. R. Jutinov, and T. A. M. Salet, "Experimental Exploration of Metal Cable as Reinforcement in 3D Printed Concrete," *Mater. 2017, Vol. 10, Page 1314*,

vol. 10, no. 11, p. 1314, Nov. 2017.

[17] D. Asprone, F. Auricchio, C. Menna, and V. Mercuri, “3D printing of reinforced concrete elements: Technology and design approach,” *Constr. Build. Mater.*, vol. 165, pp. 218–231, Mar. 2018.

[18] H. Kloft *et al.*, “TRR 277: Additive manufacturing in construction,” *Civ. Eng. Des.*, Jul. 2021.

[19] B. T. Wang and M. Rimmer, “3D Printing and Housing: Intellectual Property and Construction Law,” *Adv. 21st Century Hum. Settlements*, pp. 113–140, 2021.

[20] S. H. Saheb and J. V. Kumar, “A comprehensive review on additive manufacturing applications,” *AIP Conf. Proc.*, vol. 2281, no. 1, p. 020024, Oct. 2020.

[21] T. Wangler *et al.*, “Digital Concrete: Opportunities and Challenges,” *RILEM Tech. Lett.*, vol. 1, pp. 67–75, Oct. 2016.

[22] G. Vantyghem, W. De Corte, T. Ooms, E. Shakour, and O. Amir, “3D-Printed Concrete Bridge Designed by Topology Optimization PRINTING OF A POST-TENSIONED CONCRETE GIRDER DESIGNED BY TOPOLOGY OPTIMIZATION, AUTOMATION IN CONSTRUCTION (2020) SHAPE OPTIMIZATION.”

[23] “3D printing of a post-tensioned concrete girder designed by topology optimization | Elsevier Enhanced Reader.” [Online]. Available: https://reader.elsevier.com/reader/sd/pii/S0926580519305096?token=50356D1486D051F9BF9C58B1F2AA6A003F28E58773A8E6F33E0ECA4878F9AD65449C4097F8D31B207511AAEE2A0A63C8&originRegion=us-east-

1&originCreation=20210412221455. [Accessed: 12-Apr-2021].

[24] D. J. White, A. Abdulraheem Alhasan, P. Kumar Re Vennapusa, A. Abdulraheem, and P. Kumar Re, "Proceedings of the 2015 Conference on Autonomous and Robotic Construction of Infrastructure," 2015.

[25] D. D. Camacho *et al.*, "Applications of Additive Manufacturing in the Construction Industry A Prospective Review Applications of Additive Manufacturing in the Construction Industry-A Prospective Review," 2017.

[26] A. Siddika, M. A. Al Mamun, W. Ferdous, A. K. Saha, and R. Alyousef, "3D-printed concrete: applications, performance, and challenges," *https://doi.org/10.1080/21650373.2019.1705199*, vol. 9, no. 3, pp. 127–164, May 2019.

[27] J. Jianjing, L. Xinzheng, and G. Jingjun, "Study for Real-time Monitoring of Large-Span Bridge Using GPS," 2002.

[28] M. Ziaee and N. B. Crane, "Binder jetting: A review of process, materials, and methods," *Addit. Manuf.*, vol. 28, pp. 781–801, Aug. 2019.

[29] D. Lowke, E. Dini, A. Perrot, D. Weger, C. Gehlen, and B. Dillenburger, "Particle-bed 3D printing in concrete construction – Possibilities and challenges," *Cem. Concr. Res.*, vol. 112, pp. 50–65, Oct. 2018.

[30] "3D printed bridge - IAAC." [Online]. Available: https://iaac.net/project/3d-printed-bridge/. [Accessed: 04-Aug-2021].

[31] I. Hager, A. Golonka, and R. Putanowicz, "3D Printing of Buildings and Building

Components as the Future of Sustainable Construction?," *Procedia Eng.*, vol. 151, pp. 292–299, Jan. 2016.

[32] S. E. Buskin and L. J. Paulozzi, "Fatal injuries in the construction industry in washington state," *Am. J. Ind. Med.*, vol. 11, no. 4, pp. 453–460, Jan. 1987.

[33] H. Alhumayani, M. Gomaa, V. Soebarto, and W. Jabi, "Environmental assessment of large-scale 3D printing in construction: A comparative study between cob and concrete," *J. Clean. Prod.*, vol. 270, p. 122463, Oct. 2020.

[34] V. C. Li, "On Engineered Cementitious Composites (ECC) A Review of the Material and Its Applications," 2003.

[35] V. Li, "Tensile strain-hardening behavior or polyvinyl alcohol engineered cementitious composite (PVA-ECC)," 2001.

[36] A. N. Christiansen, J. A. Bærentzen, M. Nobel-Jørgensen, N. Aage, and O. Sigmund, "Combined shape and topology optimization of 3D structures," *Comput. Graph.*, vol. 46, pp. 25–35, Feb. 2015.

[37] G. Vantyghem, V. Boel, W. De Corte, and M. Steeman, "Compliance, Stress-Based and Multi-physics Topology Optimization for 3D-Printed Concrete Structures," *RILEM Bookseries*, vol. 19, pp. 323–332, Sep. 2018.

[38] G. Vantyghem, W. De Corte, M. Steeman, and V. Boel, "Density-based topology optimization for 3D-printable building structures," *Struct. Multidiscip. Optim. 2019 606*, vol. 60, no. 6, pp. 2391–2403, Jul. 2019.

[39] V. C. Li, "Advances in ECC Research."

[40] X. Li and M. Li, “Multifunctional self-sensing and ductile cementitious materials,” *Cem. Concr. Res.*, vol. 123, p. 105714, Sep. 2019.

[41] V. Li, “Interface Tailoring for Strain-hardening PVA-ECC.”

[42] B. Panda, S. Ruan, C. Unluer, and M. J. Tan, “Improving the 3D printability of high volume fly ash mixtures via the use of nano attapulgite clay,” *Compos. Part B Eng.*, vol. 165, pp. 75–83, May 2019.

[43] H. Jeong, S.-J. Han, S.-H. Choi, Y. J. Lee, S. T. Yi, and K. S. Kim, “Rheological Property Criteria for Buildable 3D Printing Concrete,” *Mater. 2019, Vol. 12, Page 657*, vol. 12, no. 4, p. 657, Feb. 2019.

[44] M. Li and V. C. Li, “Rheology, fiber dispersion, and robust properties of Engineered Cementitious Composites,” *Mater. Struct.*, vol. 46, no. 3, pp. 405–420, Mar. 2013.

[45] N. Roussel, “Rheological requirements for printable concretes,” *Cem. Concr. Res.*, vol. 112, pp. 76–85, Oct. 2018.

[46] A. R. Arunothayan, B. Nematollahi, R. Ranade, S. H. Bong, J. G. Sanjayan, and K. H. Khayat, “Fiber orientation effects on ultra-high performance concrete formed by 3D printing,” *Cem. Concr. Res.*, vol. 143, p. 106384, May 2021.

[47] M. Hafezolghorani, F. Hejazi, R. Vaghei, M. S. Bin Jaafar, and K. Karimzade, “Simplified damage plasticity model for concrete,” in *Structural Engineering International*, 2017, vol. 27, no. 1, pp. 68–78.